Modeling and mechanical characterization of a bio-sourced composite by non-contact kinematic field measurements

Shengnan Sun

N° d'ordre : D. U : 2450
E D S P I C : 650

UNIVERSITÉ BLAISE PASCAL - CLERMONT II

ÉCOLE DOCTORALE
SCIENCES POUR L'INGÉNIEUR DE CLERMONT-FERRAND

Thèse

présentée par :

Shengnan SUN

pour obtenir le grade de

DOCTEUR D'UNIVERSITÉ

Spécialité : Génie mécanique

Modélisation et caractérisation mécanique d'un composite bio-sourcé par mesures de champs cinématiques sans contact

Soutenue publiquement le 14 avril 2014 devant le jury :

M. C. Baley	Professeur Univ., UBS	Président
M. L. Guillaumat	Professeur Univ., ENSAM	Rapporteur
M. C. Poilâne	Maître de Conf. HDR, UNICAEN	Rapporteur
M. A. Alzina	Maître de Conf., CEC, ENSCI-GEMH	Examinateur
M. J-D. Mathias	Chargé de rech., IRSTEA	Co-directeur
Mme. E. Toussaint	Professeur Univ., Inst. Pascal, UBP	Co-directrice
M. M. Grédiac	Professeur Univ., Inst. Pascal, UBP	Co-directeur

REMERCIEMENTS

Je voudrais d'abord exprimer ma reconnaissance à M. Michel Grédiac, Mme. Evelyne Toussaint et M. Jean-Denis Mathias, mes directeurs de thèse, pour m'avoir confié ce travail. Merci pour le temps que vous m'avez consacré et pour vos nombreux conseils.

Je remercie l'Agence Nationale de la Recherche (ANR-10-ECOT-004 grant) pour le support financier qu'elle m'a apporté tout au long de ces trois années.

Je tiens à remercier plusieurs personnes de l'IFMA : M. Hugues Perrin et M. Michel Dréan pour m'avoir formée et aidée pour la manipulation des équipements de laboratoire.

J'adresse ma reconnaissance à tous les membres du jury : M. Laurent Guillaumat, M. Chistophe Poilâne, M. Christophe Baley et M. Arnaud Alzina pour m'avoir fait l'honneur d'accepter d'évaluer ce travail.

Je remercie également les différents collaborateurs du projet DEMETHER en particulier Mme. Narimane Mati-Baouche pour l'échange d'informations et la fabrication des différents composites ; Mme Fabienne Pennec pour m'avoir bien accueillie et formée en modélisation à l'Université de Limoges et également pour l'échange d'informations durant le travail.

J'adresse mes grands remerciements à ma famille pour leur soutien et leurs encouragements afin de poursuivre en thèse.

Enfin, je remercie tous ceux qui m'ont permis de traverser cette longue période à l'Université Blaise Pascal.

TABLE DES MATIÈRES

RÉSUMÉ

Ce travail de thèse a été réalisé dans le cadre du projet de l'ANR DEMETHER lancé en 2011. L'objectif du projet était d'élaborer un matériau composite d'origine bio-sourcée pour l'isolation thermique des bâtiments existants. Ces biocomposites sont constitués de broyats de tiges de tournesol liés par une biomatrice à base de chitosane. Mon travail s'est concentré essentiellement sur la caractérisation et la modélisation des propriétés mécaniques des broyats et du biocomposite.

La première phase du travail a permis de mettre en évidence l'influence de la zone de prélèvement des échantillons dans la tige ainsi que celle de l'humidité relative sur le module d'Young. Une approche statistique a également permis de prendre en considération le caractère diffus des tiges sur leurs propriétés mécaniques. Par la suite, un travail d'homogénéisation basé sur la morphologie et les caractéristiques des constituants de l'écorce a conduit à une estimation des propriétés élastiques globales de celle-ci. La deuxième phase du travail a permis de caractériser mécaniquement le biocomposite en compression par une méthode de mesures de champs sans contact développée au laboratoire. Le caractère hétérogène des champs de déformation a ainsi été directement relié aux constituants et au taux de chitosane.

Mots clés : biocomposites, tige de tournesol, propriétés hygromécaniques, analyse statistique, vieillissement, mesures de champs sans contact

ABSTRACT

This thesis was carried out within the framework of the project Demether started in 2011. The objective of this project is to develop a bio-based composite material for thermal insulation of existing buildings. These biocomposites consist of shredded sunflower stems linked by a chitosan-based biomatrix. My work is mainly focused on the characterization and the modeling of the mechanical properties of both the sunflower stem and the biocomposite.

The first part of this work highlighted the influence of both the specimen sampling location and the conditioning relative humidity on the Young's modulus of sunflower stem. A statistical approach enabled us to take into account the diffuse nature of the stems on their mechanical properties. Thereafter, a homogenization work was carried out. It led to an estimate of the elastic property of the bark based on the morphology and the characteristics of the constituents. In the second phase of the work, the mechanical behavior of the biocomposite under compression was characterized by applying a full-field measurement technique. The heterogeneous nature of the deformation fields was directly linked to the constituents and the chitosan mass percentage of the biocomposite.

Keywords: biocomposites, sunflower stem, hygromechanical properties, statistical analysis, full-field measurement

INTRODUCTION GÉNÉRALE

La raréfaction des ressources naturelles liée à leur surexploitation et les changements environnementaux liés à la croissance économique et démographique constituent l'un des grands défis que l'humanité ait à relever. Certains experts l'ont constaté : le rythme de croissance de la population est supérieur à celui des ressources agricoles et à la découverte de nouveaux gisements de ressources énergétiques non renouvelables (charbon, pétrole, gaz naturel,...). Ces évolutions négatives obligent à considérer de nouvelles voies de croissance s'inscrivant dans le concept de développement durable qui seul peut garantir à long terme un progrès économique, social et environnemental [1–4].

Dans le domaine des sciences des matériaux, le principal défi réside dans la mise au point de matériaux bio-sourcés destinés à se substituer progressivement aux matériaux dont l'origine est l'un des combustibles fossiles. Les fibres naturelles telles que les fibres de lin et de chanvre possèdent des avantages manifestes comme leur biodégradabilité, leur faible coût, leur faible densité, leur recyclabilité et leur haut module spécifique. Ces avantages ont déjà permis à ces matériaux de faire leur place dans les domaines d'applications structurelles comme l'automobile et la construction de bâtiment [5–17]. Ces matériaux sont largement cultivés, de 2001 à 2008, la surface des champs de chanvre et lin en Europe représentait déjà 114 000 hectares par an en moyenne [18].

En octobre 2009, le Commissariat Général au développement durable (CGDD) a publié un rapport sur "Les filières industrielles stratégiques de la croissance vertes". Ce rapport analyse les atouts et faiblesses de 17 filières environnementales. Il a proposé pour chacune d'entre elles des objectifs de développement à moyen et long termes [19]. Dans ce rapport, le potentiel industriel de la filière "biomasse, valorisation matériaux" a été jugé très important. L'une des pistes actuellement utilisée pour la valorisation de la biomasse consiste à développer des matériaux d'origine bio-sourcée. Ce développement a notamment donné naissance à la création de nouvelles filières agricoles non alimentaires pour faire face à ce nouveau marché. Une alternative à ces filières agricoles non alimentaires consiste à utiliser des sous-produits issus de l'agriculture comme des fibres broyées issues de céréales ou d'oléagineux, ceci afin d'élaborer des matériaux bio-sourcés à forte valeur ajoutée.

Dans le même temps, plusieurs réglementations nationales et européennes comme le Grenelle 2 de l'environnement [20] ou la directive 2002/91/CE du parlement européen [21] ont été élaborées afin de favoriser la qualité environnementale du parc des bâtiments des collectivités locales. Ces réglementations comportent notamment des recommandations

concernant l'isolation thermique des bâtiments pour réduire *in fine* la production de CO2 (Loi Grenelle 1 article 4 et article 5-I - Projet de loi Grenelle 2 article 1er et article 2). Le marché potentiel est d'environ 400 000 logements à rénover par an jusqu'à 2020, ce qui correspond à une réduction des consommations d'énergie du parc des bâtiments existants d'au moins 38 % d'ici à 2020.

Ces réglementations constituent l'une des raisons pour lesquelles le projet DEMETHER (DÉveloppement de MatÉriaux biosourcés issus de sous-produits de l'agriculture pour l'isolation THERmique des bâtiments existants [22]) a été accepté en 2010 par l'Agence Nationale de Recherche. Le projet consiste en effet à utiliser des sous-produits oléagineux et céréaliers pour développer des matériaux bio-sourcés issus de sous-produits de l'agriculture, ceci à des fins de l'isolation thermique de bâtiments existants. Ce projet se justifiait pour des raisons économiques, sociales et environnementales telles que :

- les objectifs de réduction du bilan énergétique des bâtiments existants. En effet, selon l'ADEME [1], le secteur du bâtiment est le plus gros consommateur d'énergie parmi tous les secteurs économiques, avec environ 70 millions de tonnes d'équivalent pétrole par an ;
- un stockage du carbone important pendant la durée de vie de l'immeuble, étant donné le nombre potentiel significatif de bâtiments à rénover ;
- la valorisation de sous-produits agricoles. Cela permet ainsi de diminuer l'exploitation des terres agricoles consacrées à la production industrielle. Ceci est nécessaire étant donnée la superficie des terres occupées par les cultures industrielles [23] ;
- la création d'une nouvelle application industrielle pour la filière verte, avec un fort potentiel de développement étant donné les aspects réglementaires liés à la réglementation Grenelle 2 ;
- la fourniture de matériau isolant thermique respectueux de la santé humaine et de l'environnement. Ce point est très important pour développer et évaluer la performance de matériaux isolants thermiques [24].

Le but du projet ANR DEMETHER au sein duquel ma thèse s'inscrit est de concevoir un matériau composite d'origine bio-sourcée qui doit avoir pour vocation d'isoler des bâtiments existants. L'originalité de la démarche est double :

- d'une part, des sous-produits issus de l'agriculture sont utilisés pour élaborer le matériau isolant. Dans notre cas, il s'agit de tiges de tournesol. Elles se composent de deux constituants dont les propriétés sont très différentes : l'écorce d'abord, qui possède des propriétés mécaniques suffisantes vu l'application visée, et la moelle d'autre part qui possède d'excellente propriétés d'isolation thermique. Cette deuxième

caractéristique est de fait très intéressante vu l'objectif du projet. Par ailleurs, cette plante est abondante car elle est largement cultivée pour les graines présentes dans ses fleurs dont on extrait de l'huile. Cette plante était cultivée sur 22 millions d'hectares en 2009 dans le monde entier [25]. A ce jour, il n'y a pas d'utilisation industrielle notable des tiges de ces plantes, qui restent éparses sous forme de broyats dans les champs pour nourrir le sol après la récolte, ce qui en fait un matériau abondant et très bon marché. Les avantages que possède ce sous-produit ont déjà attiré l'attention des chercheurs. Dans les travaux de Kaymaki, le poudre de tige de tournesol a été utilisé en tant que remplisseur du composite, les résultats obtenus ont montré que le poudre de tige de tournesol pourrait être potentiellement utilisé comme matière première convenant à la fabrication de composites à base de polypropylène [26, 27]. Dans les travaux de Magnions, la moelle de tige a été utilisée en tant que matériau isolant pour l'élaboration du matériau de construction à base de pouzzolane, les résultats obtenus sur les propriétés physiques, thermiques et mécaniques de ces mélanges étaient intéressantes. [28, 29]. Ces études menées sur la tige de tournesol montrent que ce sous-produit possède des propriétés prometteuses pour des applications isolation thermique et structurale ;

– d'autre part, une matrice à base de biopolymère naturel est utilisée pour lier les broyats de tiges de tournesol. Le biopolymère choisi est élaboré à partir de chitosane qui est présent notamment dans les carapaces de crabes et de crevettes. Il est largement disponible dans le commerce et potentiellement peu coûteux en fonction de la qualité et de la quantité exigées pour cette application donnée. Il a été récemment montré que le chitosane pouvait être utilisé en association avec d'autres constituants chimiques afin d'obtenir divers types de résines comportant des propriétés mécaniques intéressantes, en fait comparables à celles employées pour des applications de collage semi-structural. Les caractéristiques de la biomatrice utilisée ici ont été ajustées pour atteindre une viscosité et une mouillabilité adaptées à l'imprégnation de morceaux d'écorce et de moelle de tiges.

Au bilan, on minimise ainsi les impacts environnementaux tout en s'assurant de la possibilité d'utiliser le biocomposite pour l'isolation de bâtiments existants.

Sur le plan de sa structuration, le projet se décompose en une tâche de management et 4 tâches scientifiques : le développement d'une biomatrice (tâche 1), la caractérisation des propriétés physiques (tâche 2), la modélisation des impacts environnementaux (tâche 3) et l'application à l'isolation de bâtiments existants (tâche 4). L'organigramme de la Figure 1 décrit les objectifs de chaque tâche, les principales productions qui sont associées ainsi que les relations entre les tâches.

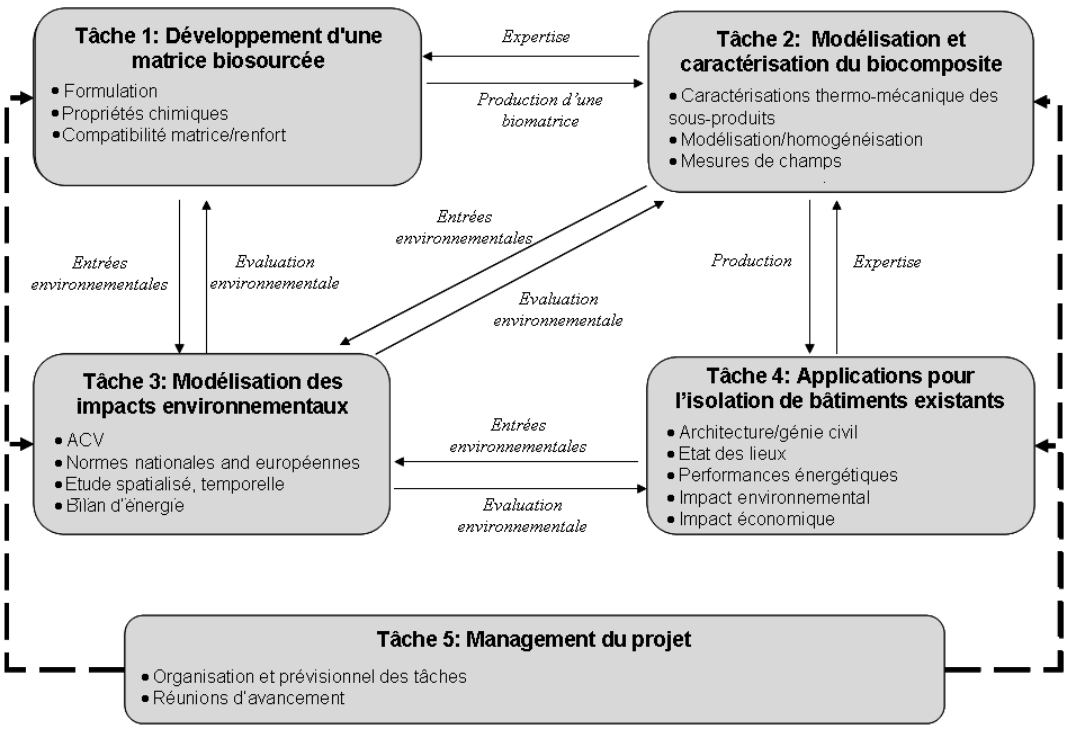

Figure 1 Organigramme technique du projet

Le sujet de ma thèse constitue une part importante de la tâche 2. Il se concentre essentiellement sur les propriétés mécaniques du biocomposite. En effet, si les propriétés thermiques sont centrales dans ce projet, il faut également assurer des propriétés mécaniques minimales aux biocomposites réalisés. Ces panneaux doivent en effet ne pas rompre sous l'effet de leur poids propre pendant les opérations de manipulation et supporter des localisation de contrainte dues au montage des panneaux sur les murs.

Le présent mémoire reprend sous forme de chapitres séparés les quatre tâches que j'ai accomplies pendant ce travail de thèse. Chacune fait l'objet d'une publication dans un journal international en langue anglaise. Ces publications sont reportées chacune dans l'un des chapitres, ce qui fait de ce document un manuscrit de thèse sur articles. Deux de ces articles sont déjà publiés. Le troisième est soumis et le quatrième est en cours de finalisation.

La première partie de ce travail de thèse a consisté à caractériser les propriétés mécaniques des constituants pris isolément. Les résultats de cette caractérisation devaient effectivement servir à la conception du biocomposite en termes de compromis entre propriétés mécaniques et thermiques. Les résultats devaient également augmenter le champs des connaissances et faciliter l'emploi de ce sous-produit agricole pour d'autres applications : en effet, il est apparu que très peu d'études concernant les propriétés

mécaniques de tige de tournesol étaient disponibles dans la littérature. Cette première étude se devait donc de combler ce vide. Elle a été conduite en observant notamment le lien entre propriétés mécaniques et localisation de l'éprouvette dans la tige. L'influence de l'humidité sur les propriétés mécaniques a aussi été examinée. Ce travail est présenté au sein du chapitre un de ce manuscrit.

Vu que les constituants sont d'origine organique, leurs propriétés présentent une dispersion qui doit être caractérisée soigneusement afin de pouvoir l'intégrer dans le comportement macroscopique du biocomposite. L'étude statistique de la dispersion des propriétés mécaniques a donc fait l'objet de la deuxième partie du travail. Plusieurs centaines d'éprouvettes ont été testées afin de caractériser cette dispersion et de déterminer les facteurs l'influençant, ceci afin de pouvoir ensuite mieux les contrôler lors de la phase d'utilisation des broyats à des fins de fabrication des composites. L'étude a été conduite principalement sur l'écorce car c'est elle qui contribue à l'essentiel des propriétés mécaniques du composite. Les résultats obtenus sont rassemblés dans le chapitre deux du manuscrit.

Les biocomposites étudiés ici rassemblent donc des constituants comme des morceaux d'écorce et de moelle liés par une biomatrice. S'ajoutent encore à cela des porosités bien visibles à l'œil nu. L'ensemble forme donc un matériau extrêmement hétérogène. Il a donc semblé judicieux d'en étudier finement le comportement mécanique réel en observant les champs mécaniques hétérogènes qui voient le jour à l'échelle de ces constituants lorsque l'ensemble était sollicité mécaniquement. Cependant, l'instrumentation associée classiquement aux essais mécaniques ne permet pas de distinguer des comportements *a priori* différents de ces constituants : l'étude des courbes classiques contraintes moyenne/déformation moyenne n'apporte effectivement pas l'information recherchée. La mise en place de capteurs locaux comme des jauges de déformation semble inadaptée vu les niveaux de déformation *a priori* faibles dans ces constituants, leur dimension et leur rigidité faible pour certains d'entre eux comme la moelle. L'idée a donc été d'utiliser une technique de mesure de champs cinématiques sans contact susceptible d'apporter une information sur le comportement réel *in situ* des constituants. Vu la nature inhabituellement hétérogène de ce matériau en comparaison aux matériaux utilisés en construction, la capacité à obtenir de tels champs a déjà constitué un premier challenge. La technique dite de corrélation d'images, qui est la plus utilisée en pratique en mécaniques expérimentale, n'a pas été retenue au vu de sa trop faible résolution spatiale. Nous nous sommes donc tournés vers la méthode dite "de grille" développée au laboratoire. Cette technique nécessite cependant un marquage régulier de la surface étudiée qui est peu compatible avec les hétérogénéités qu'on y observe. Il a donc été nécessaire de mettre au point une technique de marquage originale

qui a permis *in fine* de bien mettre en évidence des champs de déformations hétérogènes, de les interpréter et de les mettre en relation avec le comportement macroscopique du biocomposites. L'ensemble de ces résultats est rassemblé au chapitre trois.

D'un point de vue macroscopique, le tige de tournesol est composée de l'écorce et de la moelle. A une échelle plus petite, la moelle est composée seulement de parenchyme. La composition de l'écorce est quant à elle plus complexe car elle rassemble à la fois des fibres de sclérenchyme et du xylème. La porosité et le contenu de ces tissus biologiques varient en fonction de la hauteur de prélèvement des échantillons sur la tige. Il en sera donc de même des propriétés mécaniques. Pour mieux comprendre ce lien entre propriétés mécaniques de ces composants à l'échelle des cellules, caractéristiques morphologiques et propriétés mécaniques à l'échelle macroscopique, un travail portant sur l'homogénéisation et le passage micro-macro a été accompli. Les résultats obtenus sont basés principalement sur l'emploi de la loi des mélanges, d'un modèle sphéroïdal et d'un modèle cylindrique pour prendre en compte la forme des pores, les caractéristiques des constituants étant prises dans la littérature vu la difficulté pour les mesurer. Il en ressort un bon accord entre valeurs ainsi prédites et valeurs constatées en pratique, ce qui valide l'approche. Ces résultats sont présentés au chapitre quatre.

Enfin, trois annexes sont placées à la fin du document. On y trouve des résultats qui complètent ceux donnés dans ces quatre chapitres.

Bibliographie

[1] ADEME, Grands enjeux de développement durable, Agence de l'Environnement et de la Maîtrise de l'Energie. URL `http://www2.ademe.fr/servlet/KBaseShow?sort=-1&cid=96&m=3&catid=13329`.

[2] L. Guay, Les enjeux et les défis du développement durable : connaître, décider, agir, Presses Université Laval, (2004).

[3] M. Munasinghe, Environmental economics and sustainable development, World Bank Publications, 3 (1993).

[4] W-M. Adams, Green development : Environment and sustainability in the Third World, Routledge, (2003).

[5] A. Mohanty, M. Misra, L. Drzal, Natural fibers, biopolymers, and biocomposites, CRC, (2005).

[6] A. Bledzki, J. Gassan, Composites reinforced with cellulose based fibres, Progress in polymer science 24 (2) (1999) 221–274.

[7] P. Wambua, J. Ivens, I. Verpoest, Natural fibres : can they replace glass in fibre reinforced plastics ?, Composites Science and Technology 63 (9) (2003) 1259 – 1264.

[8] M. Aziz, P. Paramasivam, S. Lee, Prospects for natural fibre reinforced concretes in construction, International Journal of Cement Composites and Lightweight Concrete 3 (2) (1981) 123–132.

[9] M. J. John, S. Thomas, Biofibres and biocomposites, Carbohydrate polymers 71 (3) (2008) 343–364.

[10] H.-R. Kymäläinen, A.-M. Sjöberg, Flax and hemp fibres as raw materials for thermal insulations, Building and environment 43 (7) (2008) 1261–1269.

[11] A. C. Schmidt, A. A. Jensen, A. U. Clausen, O. Kamstrup, D. Postlethwaite, A comparative life cycle assessment of building insulation products made of stone wool, paper wool and flax, The International Journal of Life Cycle Assessment 9 (1) (2004) 53–66.

[12] Z. Pavlík, R. Černỳ, Hygrothermal performance study of an innovative interior thermal insulation system, Applied Thermal Engineering 29 (10) (2009) 1941–1946.

[13] A. Korjenic, V. Petránek, J. Zach, J. Hroudová, Development and performance evaluation of natural thermal-insulation materials composed of renewable resources, Energy and Buildings 43 (9) (2011) 2518–2523.

[14] S. Elfordy, F. Lucas, F. Tancret, Y. Scudeller, L. Goudet, Mechanical and thermal properties of lime and hemp concrete ("hempcrete") manufactured by a projection process, Construction and Building Materials 22 (10) (2008) 2116–2123.

[15] Z. Li, X. Wang, L. Wang, Properties of hemp fibre reinforced concrete composites, Composites part A : applied science and manufacturing 37 (3) (2006) 497–505.

[16] D. Sedan, C. Pagnoux, A. Smith, T. Chotard, Mechanical properties of hemp fibre reinforced cement : Influence of the fibre/matrix interaction, Journal of the European Ceramic Society 28 (1) (2008) 183–192.

[17] P. Coatanlem, R. Jauberthie, F. Rendell, Lightweight wood chipping concrete durability, Construction and building Materials 20 (9) (2006) 776–781.

[18] C. Meirhaeghie, Evaluation de la disponibilité et de l'accessibilité de fibres végétales à usages matériaux en France, Etude réalisée pour le compte de l'ADEME par Fibres Recherche Développement, (2011).

[19] CGDD, Etude « filières vertes » : Les filières industrielles stratégiques de la croissance verte, Rapport du Commissariat Général au Développement Durable (CGDD).

[20] Loi Grenelle 2, URL `http://www.developpement-durable.gouv.fr/IMG/pdf/Grenelle_Loi-2.pdf`, last accessed mar, 2014.

[21] Directive 2002/91/CE, Directive 2002/91/CE du Parlement européen et du Conseil du 16 décembre 2002, URL `http://www.legifrance.gouv.fr/affichTexte.do?cidTexte=JORFTEXT000000702199`, last accessed mar, 2014.

[22] DEMETHER, Demether (anr-10-ecot-004 grant) : Développement de matériaux biosourcés issus de sous-produits de l'agriculture pour l'isolation thermique des bâtiments existants, `http://demether.cemagref.fr/`, last accessed mar, 2014.

[23] Superficies agricoles consacrées aux productions non alimentaires, `http://ec.europa.eu/agriculture/envir/report/fr/n-food_fr/report.htm`, last accessed mar, 2014.

[24] A. Papadopoulos, State of the art in thermal insulation materials and aims for future developments, Energy and Buildings 37 (1) (2005) 77–86.

[25] A. Semerci, Y. Kaya, The components of production cost in sunflower and its relationships with input prices, in : International Conference on Applied Economic - ICOAE 2009 (2009) 593–599.

[26] K. Alperen and A. Nadir and O. Ferhat and G. Turker, Surface Properties and Hardness of Polypropylene Composites Filled With Sunflower Stalk Flour, BioResources, 8 (1) (2013).

[27] K. Alperen and A. Nadir and O. Ferhat and G. Turker, Utilization of sunflower stalk in manufacture of thermoplastic composite, Journal of Polymers and the Environment 37 (3) (2013) 1135–1142.

[28] C. Magniont, and G ; Escadeillas and M .Coutand, and C .Oms-Multon. Use of plant aggregates in building ecomaterials. European Journal of Environmental and Civil Engineering, 16 (sup1) (2012) s17–s33.

[29] C. Magniont, Contribution à la formulation et à la caractérisation d'un écomatériau de construction à base d'agroressources, Thèse de doctorat. Toulouse 3, (2010).

Chapitre 1

Hygromechanical characterization of sunflower stems

Article publié dans le journal : Industrial Crops and Products
Année : 2013
Numéro de volume : 46
Pages : 50-59

Introduction au chapitre 1

Ce premier chapitre a pour objectif de déterminer les propriétés hygroscopiques et mécaniques des deux constituants des tiges de tournesol : la moelle et l'écorce. En effet, avant de fabriquer des biocomposites à partir de ces deux constituants, il est nécessaire de les caractériser finement. Étant donné que le comportement mécanique des matériaux d'origine bio-sourcée est souvent sensible à l'humidité relative ambiante, leur comportement hygroscopique a d'abord été caractérisé. Pour cela, des tests d'absorption et de désorption ont été effectués, permettant l'identification du coefficient de diffusion d'humidité de la moelle et de l'écorce. Des tests mécaniques ont été ensuite réalisés en variant le taux d'humidité relative et la position des éprouvettes le long de la tige afin de quantifier leur influence sur les propriétés mécaniques de la moelle et de l'écorce.
Des résultats complémentaires sont disponibles dans l'Annexe A. On y voit également des photos montrant les éprouvettes en place dans les machines d'essai (traction et compression).

Hygromechanical characterization of sunflower stems

Shengnan SUN[1], Evelyne TOUSSAINT[1†], Jean-Denis MATHIAS[2] and Michel GREDIAC[1]

[1] *Clermont Université, Université Blaise Pascal, Institut Pascal, UMR CNRS 6602*
BP 10448, 63000 Clermont-Ferrand, France
[2] *IRSTEA, Laboratoire d'Ingénierie pour les Systèmes Complexes*
9 Avenue Blaise Pascal, CS20085, 63178 Aubière, France

[†] *corresponding author. Tel.: +33 473288073; fax:+33 473288027,*
evelyne.toussaint@univ-bpclermont.fr

Abstract

This study concerns the determination of hygromechanical properties of sunflower stems. Mechanical tests were carried out on specimens of sunflower bark and pith. Particular attention was paid to the influence on the mechanical properties of (i) specimen location along the stem and (ii) moisture content of specimens. For this purpose, specimens were taken from the bottom, middle, and top of the stems. The influence of humidity on the mechanical properties was studied by testing specimens conditioned at three different relative humidities: 0% RH, 33% RH and 75% RH. Moisture diffusion coefficients of bark and pith were deduced assuming Fick's law to predict the variation in moisture content of the specimens during the mechanical test. The Young's modulus of the bark was found to be higher than that of the pith, whereas the moisture diffusion coefficient of the bark was lower than that of the pith. Mechanical and hygroscopic properties of specimens depended on their location along the stem. In order to explain these results, morphological observations have been carried out on the specimen at each location. It was found that porosity of both the bark and the pith are lower at the top of the stem. The presence of sclerenchyma in the bark is also higher at the top of the stem.

Keywords: Sunflower stems, Mechanical properties, Moisture diffusion coefficients, Morphologies, Specimen location, Moisture content

1 Introduction

Green industry is important both economically and environmentally. Research on the development of new bio-sourced materials has thus been attracting more and more attention. During the last decades, bio-composites reinforced by plant fibers such as wood, flax, hemp, jute and sisal have been rapidly developed for various industrial applications such as structural components for the automotive and building industries [1]. Compared with conventional synthetic fibers, natural fibers offer some advantages including cheapness, low density and biodegradability, but their mechanical properties are generally inferior.

Besides industrial crop activity mainly devoted to fiber production, another potential source of natural fiber supply is agricultural by-products, especially for industrial applications in which required mechanical performance is not too high. Against a rapid expansion of natural fiber-based composites, new composites reinforced with agriculture by-product fibers offer a potentially effective way to ease disparities in natural fiber supply and demand. The cellulose content of most agricultural by-product fibers is generally lower than that of traditional natural fibers such as wood, flax, hemp, jute or sisal. Cellulose content directly influences mechanical properties. This drawback can, however, be offset by cheapness in many industrial applications. Some studies on the use of agricultural by-products as composite reinforcement are reported in the literature. They concern corn stalk, and wheat, rice or corn straw [2–8]. These studies clearly show that such by-products offer a relevant, promising solution for some composite applications. The even trade-off between cheapness, mechanical properties, abundance and availability of these agricultural by-products makes it possible to use them in industrial applications. Aside from these advantages, using agricultural by-products can also improve the agriculture-based economy and create new market opportunities.

This study concerns the characterization of hygromechanical properties of sunflower stems, an abundant agricultural by-product.These stems are generally shredded during flower harvesting and used as natural fertilizer. In Europe, sunflower is cultivated for the edible oil extracted from its grains: it is one of the three main sources of edible oil along with rapeseed and olive. This plant is thus widely cultivated. In 2010, the harvested area in Europe was 14.31E+06 ha, 61.82% of the total harvested area in the world [9]. The flower itself is clearly the most useful part of the plant; there is no significant industrial use of the stems shredded after flower harvesting. These stems may, however, exhibit favorable mechanical properties (of the bark) and good heat insulation properties (of the pith). Hence this by-product could find use in bio-sourced composite materials.

The aim of this study was to investigate the mechanical properties of the bark and pith of

sunflower stems. Our purpose was to collect information that would be useful for designing bio-composite panels suitable for building insulation (see project ANR [10]). Such panels must feature both useful heat insulation properties and mechanical properties sufficient to ensure safe handling, transport and assembly. The properties of the bark and the pith directly influence the properties of the panels. It is clear that the pith of the stem shows good insulation properties while the bark shows good mechanical properties. The mechanical responses of both the pith and bark have therefore to be assessed for predicting and modeling the global response of the panels and find a trade-off between heat insulation and mechanical properties.

In what follows, the specimens, tests and testing procedures are first described. Results obtained with hygroscopic and mechanical tests performed on bark and pith of sunflower stems are then presented and discussed, with special emphasis on the influence of the moisture and sampling zones on the results obtained.

2 Material and methods

2.1 Specimens, locations and preparation

2.1.1 Introduction

The sunflower species used for this study was LG5474, grown in Perrier, France, in 2010. A separate mechanical characterization was justified by the fact that the appearance of the bark and pith, and their hygromechanical properties, were very different. Specimens used in this study were extracted from portions of stems of length 765 mm. For all the stems from which specimens were cut, the bottom section was chosen at the level of the first node above the roots. The location of this first node did not significantly change from one stem to another. Three sampling zones were chosen to investigate the effect of specimen location on hygromechanical properties. The first sampling zone was located at the bottom of each stem, the second at the middle and the third at the top (see Figure 1). These short portions of stem were then used to cut either bark or pith specimens, but not both at the same time, because cutting bark specimens damages pith and *vice versa*.

2.1.2 Bark specimens

For bark specimens, the short portions of stems were divided lengthwise into six parts (see cross section A-A in Figure 1). Bark specimens extracted from the same angular location were noted with the same number (from 1 to 6). The geometry of the specimens was the same for the mechanical and for the hygroscopic tests (see Figure 2-a) as regards dimensions and inner

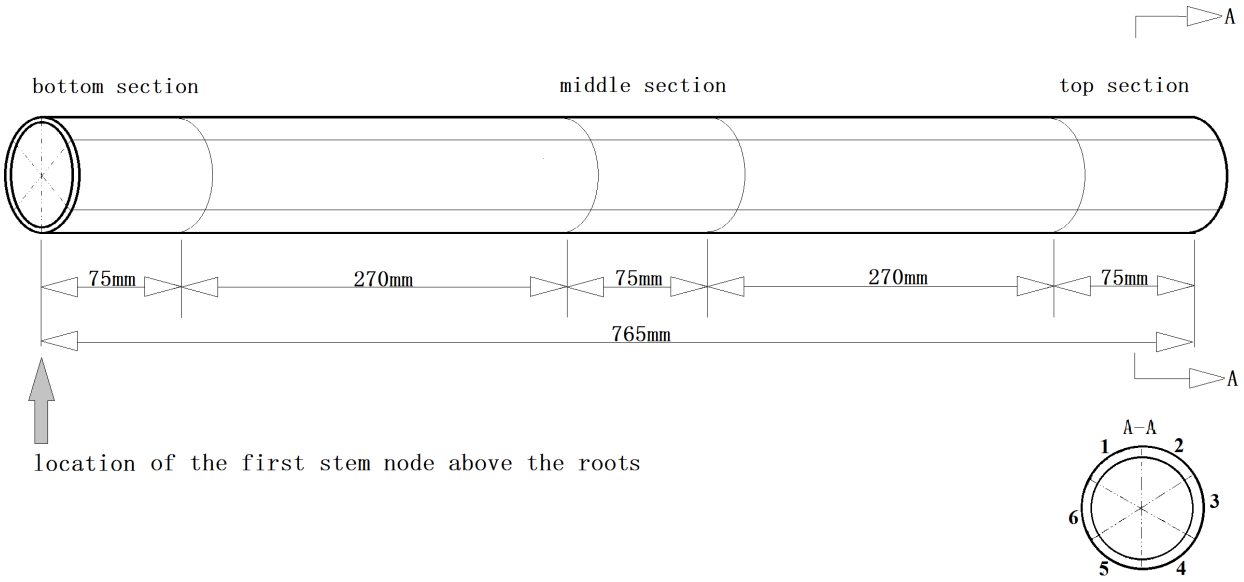

Figure 1 Sampling zones

and outer surfaces of the bark specimens. To obtain nearly plane specimens and to remove some pith residues, the inner face of the bark was lightly polished with sandpaper. The outer face was not polished, because some stiff fibers (sclerenchyma) are located around the stems; polishing the outer surface would have damaged them, thereby influencing the mechanical properties. These fibers and other stem components are clearly visible in Figure 3 [11], where a typical cross section of sunflower stem is depicted.

For the hygroscopic tests, six specimens cut from two stems were tested for each of the three sections (bottom, middle and top). Three non-adjacent specimens were chosen from each section, for example specimens 1, 3, 5 (see Figure 1). Only three specimens were chosen per section and per stem (and not the whole set of six), because preparing the specimens was time-consuming and intricate. The number of specimens was therefore limited. All these specimens then underwent two different absorption/desorption tests: the specimens were first dried in an oven (see description below) and then exposed to two different levels of relative humidity (33% RH and 75% RH). When reaching the moisture equilibrium state in the absorption test, they were then exposed to the 8% RH to continue the desorption test. The same specimens were used for both types of tests. They were dried between each test.

For the mechanical tests, six specimens were prepared for each of the three sections of five different stems. For each section, two of these six specimens located along the same diagonal (for instance 1-4, 2-5 or 3-6) were selected, thus giving each time a set of ten specimens (2 specimens $\times$ 5 stems). Three sets of ten specimens were thus obtained for each

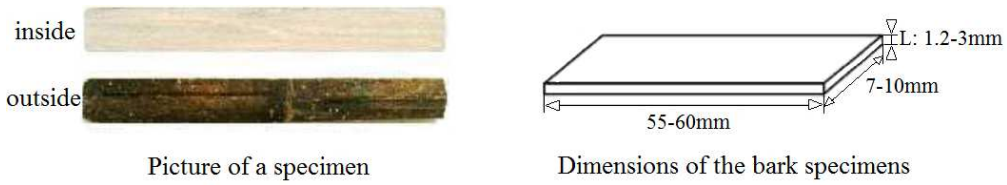

Picture of a specimen Dimensions of the bark specimens

(a) Bark specimen

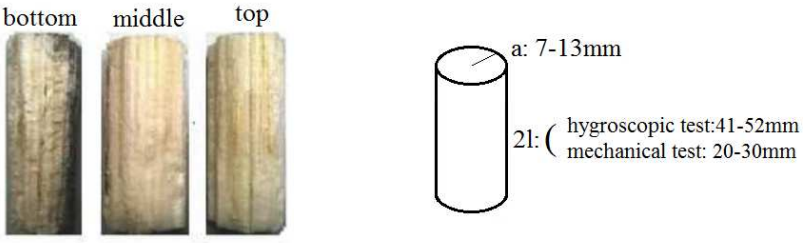

Pith at different locations Dimensions of the pith specimens

(b) Pith specimen

Figure 2 Bark and pith specimens

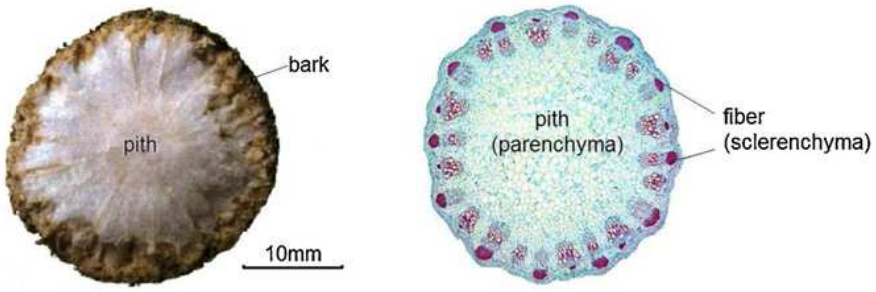

(a) Picture (b) Micrography (Tiftickjian, 2012)

Figure 3 Structure of a sunflower stem

section location (bottom, middle and top). Each of these sets was then conditioned at the following values of relative humidity: 0% RH (oven dried), 33% RH, 75% RH as described in Section 2.2.2 below.

2.1.3 Pith specimens

The pith specimens were obtained simply by removing the bark from each short portion of stem. Some typical pith specimens are presented in Figure 2-b. These pith specimens were nearly cylindrical in shape, with a diameter ranging from 14 mm to 26 mm, depending on the stems and on the level where they were cut (see Figure 2-b). It was surprised to find that the greatest diameter was obtained at the middle of each stem, not at the bottom. On average,

the diameter of the pith specimens obtained at the middle of the stem was 1.20 times the value of that obtained at the bottom, and 1.02 times the value of that at the top.

For the hygroscopic tests, five stems were tested and three specimens were extracted from each stem (one at each level), giving a total amount of five specimens per location. These three sets of five specimens (one for each section) underwent the same absorption/desorption tests as the bark specimens.

For the mechanical tests, a procedure similar to the above was followed. Fifteen stems were tested and three cylindrical specimens were extracted from each stem. Compression tests were performed, as explained below. To avoid buckling, it was decided to split each specimen into two different parts for each level, thus giving $2 \times 15 = 30$ specimens at each level. The a/l ratio (see Figure 2-(b)) ranged from 1 to 2, depending on the specimens. The same RH conditioning procedures as those used for the bark were applied. As the same three different values of RH as for the bark specimens were chosen (see further details in Section 2.2.2 below), 10 specimens were tested at each RH and at each level.

2.2 Hygroscopic tests

2.2.1 Introduction

Hygroscopic tests were performed to determine the moisture diffusion coefficient of both the bark and the pith. The first reason was that the mechanical tests were performed with specimens conditioned before mechanical testing with various values of RH. Because the testing machine used was not equipped with a conditioning chamber, specimens were first extracted from conditioning chambers where the desired RH values were adjusted (the conditioning procedure is explained below). They were then placed in the grips of the testing machine and the tests were finally performed at room temperature and RH. This meant that a certain time elapsed before each mechanical test began, during which the moisture content within the specimens could change. Knowing the moisture diffusion coefficient enabled one to predict the actual moisture content when the test began, thus making it possible to check whether it changed negligibly or not. Assessing the moisture diffusion coefficient was also justified by the fact that it affects the overall insulation properties of panels reinforced with shredded sunflower stems.

2.2.2 Experimental method

The specimens were first dried in an oven for 48 hours at 60 ℃ and 0% RH. A desiccant (phosphorus pentoxide) was placed in the oven beforehand. The specimens were then placed in two types of conditioning chamber (one for each desired value of RH). These

chambers were in fact polymer jars in which saturated aqueous salt solutions were placed. The RH depends on the nature of the salt (see Table 1). These salt solutions were chosen

Saturated aqueous salt solutions	**RH (%) at different temperatures**			
	20 °C	25 °C	30 °C	35 °C
Potassium hydroxide	9	8	7	7
Magnesium chloride hexahydrate	33	33	32	32
Sodium chloride	75	75	75	75

Table 1 Relative humidities produced by the saturated aqueous salt solutions

so that the RH was equal to 8%, 33% or 75%. The 8% RH is the value closest to 0% RH that can be obtained with salt solutions, and so was used for the desorption test that followed the absorption test. Changes in conditioning RH values for each specimen throughout the hygroscopic experimental process are shown in Figure 4. The moisture diffusion coefficients were determined using suitable relationships involving the mass of the specimen *vs.* time and its geometry. The specimens were regularly extracted from the jars and the mass was measured *vs.* time using a KERNK & Sohn GmbH electronic balance (precision: 0.1 mg). The change in mass is in fact related solely to water uptake or loss. Since absorption and desorption tests were performed, both the absorption and desorption coefficients were deduced from the mass-time curves using suitable relationships depending on the geometry of the specimens. The procedure used to prepare the different solutions

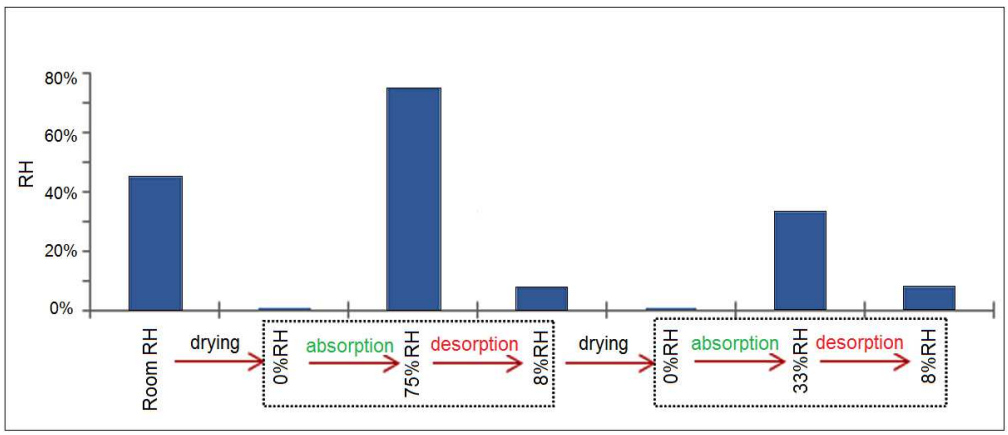

Figure 4 Conditioning RH values variations throughout the hygroscopic experimental process

corresponding to different RH levels is given in Ref. [12]. The absorption/desorption tests lasted at least three days to ensure that equilibrium was reached for the specimens. For

each hygroscopic test, the experimental moisture ratio M_t/M_{eq}, where M_t is the water uptake/loss measured at time t and M_{eq} the water uptake/loss measured at equilibrium, were computed for all the recorded data. From these measurements it is then possible to determine the moisture diffusion coefficients. Because two different geometries were used (rectangular parallelepipeds for the bark specimens, cylinders for the pith specimens), two separate diffusion models were employed.

2.2.3 Identification of moisture diffusion coefficients

Fick's second law was used here to model the diffusion process and determine the moisture diffusion coefficients from experimental measurements. This law can be simplified by taking into account the geometry of the specimens. It is assumed that specimens were plane sheets for bark specimens and cylinders for pith specimens. For a plane sheet (bark specimens) with sides parallel to the coordinate axes, Fick's second law only considers the diffusion through the thickness of the plane sheet. It is expressed as follows [13]:

$$\frac{\partial C(z,t)}{\partial t} = -D\frac{\partial^2 C(z,t)}{\partial z^2} \tag{1}$$

where C represents the concentration of diffusing substance, D the moisture diffusion coefficient and z the through-thickness direction. In the current case, each homogeneous specimen of bark was considered as a plane sheet of thickness L. Depending on the value of $\frac{M_t}{M_{eq}}$ ratio, the approximate solutions of Fick's second law are as follows [14]:

$$\begin{cases} \frac{M_t}{M_{eq}} = \frac{4}{L}\sqrt{\frac{Dt}{\pi}} & \left(\frac{M_t}{M_{eq}} \leqslant 0.5\right) \\ \ln(1-\frac{M_t}{M_{eq}}) = \ln\frac{8}{\pi^2} - \frac{\pi^2 Dt}{L^2} & \left(\frac{M_t}{M_{eq}} \geqslant 0.5\right) \end{cases} \tag{2}$$

Specimens of pith were considered as finite cylinders of length $2l$ and radius a. For this geometry, Equation 1 is [13]:

$$\frac{\partial C}{\partial t} = \frac{1}{r}\left\{\frac{\partial}{\partial r}\left(rD\frac{\partial C}{\partial r}\right) + \frac{\partial}{\partial \theta}\left(\frac{D}{r}\frac{\partial C}{\partial \theta}\right) + \frac{\partial}{\partial z}\left(rD\frac{\partial C}{\partial z}\right)\right\} \tag{3}$$

The approximate solution for Fick's second law becomes [15]:

$$\frac{M_t}{M_{eq}} = 1 - \frac{8}{\pi^2}\left[\sum_{n=1}^{\infty}\frac{4}{a^2\alpha_n^2}exp\big[-D\alpha_n^2 t\big]\right]\left[\sum_{n=0}^{\infty}\frac{1}{(2n+1)^2}exp\big[-D(2n+1)^2 t(\frac{1}{l})^2\big]\right] \tag{4}$$

where α_n is the nth positive root of $J_0(a\alpha_n)$ and J_0 the Bessel function of zero order.

The moisture diffusion coefficient was determined in each case by minimizing a cost function defined by the squared difference between experimental and theoretical values of moisture ratios. The Matlab software [16] was used for this purpose.

2.3 Observations of the bark specimen morphology

Microscopic observations of bark specimens were performed on specimens for the three locations (bottom, middle, top) to correlate the moisture diffusion coefficients with the specimen sampling location.

First, a section was separated from the stem to obtain a 1×1 cm^2 specimen. These specimens were then saturated with water, immersed, and kept in three different PEG (polyethylene glycol electrolyte) solution concentrations (30%, 60% and 100%) for 24 hours. A specimen of 20 μm thickness was cut using a LEICA RM2255 automatic rotary microtome. This specimen was then stained with the double staining method using safranin and astra blue (safranin indicates the presence of lignin and astra blue that of cellulose). After staining, the samples were dried using Joseph paper, a filter paper also used in chemistry for cleaning and drying. They were then mounted on a cover-slip with a EUKITT fast-drying mounting medium. Finally, pictures of cross sections were obtained using a ZEISS light microscope (magnification: $\times 4$).

2.4 Mechanical tests

The mechanical tests were carried out at room temperature and RH. The influence of moisture content and specimen locations on the mechanical properties was studied. Mechanical properties were deduced by processing the stress-strain curves obtained from the mechanical tests.

Tensile tests were performed on specimens of bark with a Deben MICROTEST testing machine equipped with a 2-kN load cell. The cross-head speed was equal to 2 mm/min. The specimen clamping length was 30 mm. The longitudinal mechanical properties (Young's modulus and tensile strength) were deduced from these tests.

As the dimensions of the pith specimens were not suited to the Deben MICROTEST testing machine, compression tests were carried out with an INSTRON 5543 testing machine equipped with a 500-N load cell. The cross-head speed was 5 mm/min. The longitudinal mechanical properties (Young's modulus and compressive yield strength) were deduced from these tests.

3 Results and discussion

3.1 Hygroscopic results

3.1.1 Bark specimens

The moisture diffusion coefficients were determined using experimental data and Fick's second law. A typical best-fitting curve is plotted in Figure 5.

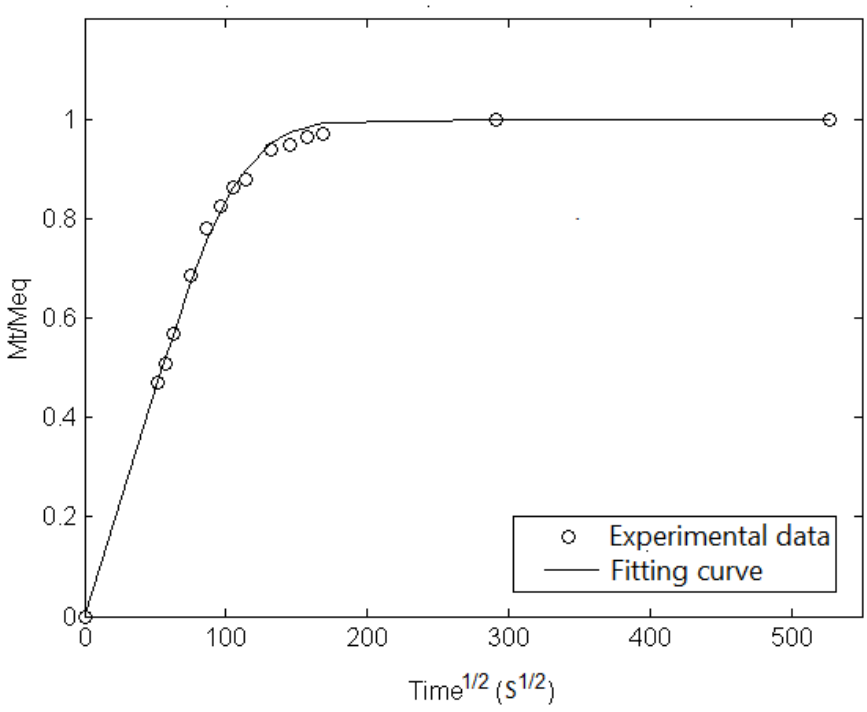

Figure 5 Typical water absorption curve for bark

Influence of the location of the specimens along the stems The moisture diffusion coefficients of bark specimens are shown in Figure 6 for the three locations, the two conditioning RH (33% and 75%), and the absorption/desorption tests. Each bar in the figure presents the mean value of six specimens obtained from the same height location. The specimen height location influences the value of the moisture diffusion coefficient. This value decreases according to the height of the stem: the mean moisture diffusion coefficient (of all the specimens tested in this study) at the bottom of the stem is 2.4 times the value of the moisture diffusion coefficient at the top, and 1.6 times the value of the moisture diffusion coefficient at the middle. This significant difference may be linked to the microscopic structure of the bark. Microscopic morphological observations were performed

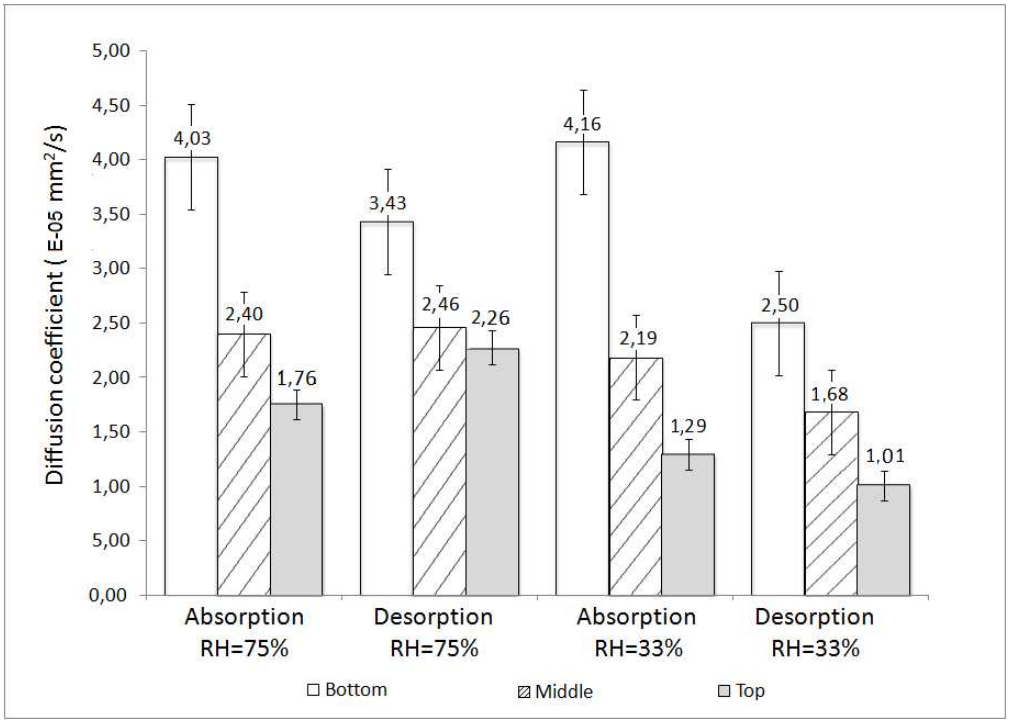

Figure 6 Diffusion coefficient determined for bark

on the bark extracted at the bottom, middle and top of the stem to find out more about this effect (see Figure 7 (a)).

The microscopic images show that the bark can be considered as a porous medium. The microscopic pores are due to the cell cavities, which are surrounded and separated by cell walls. The moisture transport mechanism in the bark is directly linked to these cell cavities, as described and explained for other materials such as wood [17]. Like the moisture diffusion process in wood [17], moisture diffusion in bark is governed by two mechanisms: vapor diffusion through the cell cavities and bound water diffusion through the cell walls. Also, in wood materials [17] the moisture diffusion coefficient of cell cavities is much greater than the moisture diffusion coefficient of cell walls. It can therefore be considered that the porosity of bark specimens influences the macroscopic diffusion coefficient obtained from the hygroscopic tests. In this case, the increase in porosity or the decrease in cell wall content of specimens may have caused the increase in the moisture diffusion coefficient of specimens. To highlight the influence of the microscopic porosity on the moisture diffusion coefficient, a porosity analysis was performed.

The porosity (pore fractions and pore sizes) was analyzed using both bottom- and top-sampled microscopic images. The porosity ratios were calculated using the ImageJ image processing software [18]. A representative part of the microscopic bark structure in each

image was chosen for the porosity analysis (see rectangles in Figure 7(a)). The dimensions of these representative parts were chosen according to the dimensions of the bark specimens tested. They also depend on their locations. Binarized figures are presented in Figures 7(b)(c). The pore area fractions were calculated for different size ranges. The results are given in Table 2.

Area range of pore (μm^2)	**Pore area fraction** Bottom	Top
0-500	13.0	12.7
500-1500	8.1	3.9
>1500	37.5	36.2
Total	58.5	52.9

Table 2 Pore area fraction of bottom and top sampled bark specimens (%)

They show that bark specimens located at the bottom of the stem have a higher porosity than bark specimens located at the top. This finding can certainly explain the decrease in moisture diffusion coefficient from the bottom to the top of the stem. The value of the moisture diffusion coefficient could be influenced by the nature of the cell walls. The nature of the cell walls is now analyzed.

The nature of the cell walls may also influence the value of the moisture diffusion coefficient. The inner part of the bark is mainly composed of xylem and fewer sclerenchyma and parenchyma (pith ray) cells (see Figure 7). The cell walls of xylem and sclerenchyma are most likely to decrease moisture diffusion through the thickness of the bark specimens. This is because their cell walls contain large amount of lignin, marked red by safrin in Figure 7. Lignin makes the cell wall hydrophobic [19]. This could also be demonstrated by the basic function of xylem, which is to transport water along the stem. Hence cell walls should be able to prevent the water passing through to achieve water transport along the stem (see the circular holes in Figure 7). The presence of parenchyma, xylem and sclerenchyma depends on location along the stem (see Figure 7(a)):

- for the bottom, middle and top sections, it is observed that the pith ray (parenchyma tissue) extends and forms a channel between the pith and the cortex of the stem. Compared with the cell walls of xylem and sclerenchyma, parenchyma cell walls tend to increase the value of the moisture diffusion coefficient. The presence of parenchyma tissue is very significant in the bark at the bottom of the stems and is less significant at the top. The significant presence of parenchyma cells may help to increase the value of the moisture diffusion coefficient at the bottom of the stem;

- sclerenchyma and xylem were observed at the middle and top sections of the stem. These types of cell may therefore help to lower the value of the moisture diffusion coefficient. This result was confirmed by the results of an exploratory study during which the cellulose and lignin contents were measured. The specimens cut at the bottom and top of five stems, which underwent tensile tests, were first powdered and mixed for each of the two levels. Both resulting powders then underwent chemical analysis to measure the cellulose and lignin contents. The results obtained: 36% and 60% cellulose; 22% and 28% lignin at the bottom and the top, respectively, agree with the difference in moisture diffusion coefficients found between these two levels, as moisture diffusion coefficient is related to lignin content, as stated in Ref. [19];
- the percentage of sclerenchyma per unit volume increases from the middle to the top sections of the stem. As stated above, lignin makes the cell wall hydrophobic [19], so one can suppose that the sclerenchyma is more hydrophobic than xylem because its concentration of lignin is higher; see the red color in Figure 7. Since the minimum thickness of the specimens decreases from the bottom to the top, the percentage of sclerenchyma per unit volume increases and so may result in a decrease in the moisture diffusion coefficient.

In sum, porosity and presence of cells directly influence the value of the moisture diffusion coefficient along the stem.

3.1.2 Pith specimens

The moisture diffusion coefficients were identified from the experimental moisture ratio curves, similarly to the bark. A typical fitting curve is plotted in Figure 8. The moisture diffusion coefficient decreases along the stem (see Figure 9), whatever the RH and in both absorption and desorption tests. Taking into consideration the results obtained for all the specimens in this study, the mean moisture diffusion coefficient at the bottom of the stem is 2.2 times that at the top, and 1.2 times that at the middle.

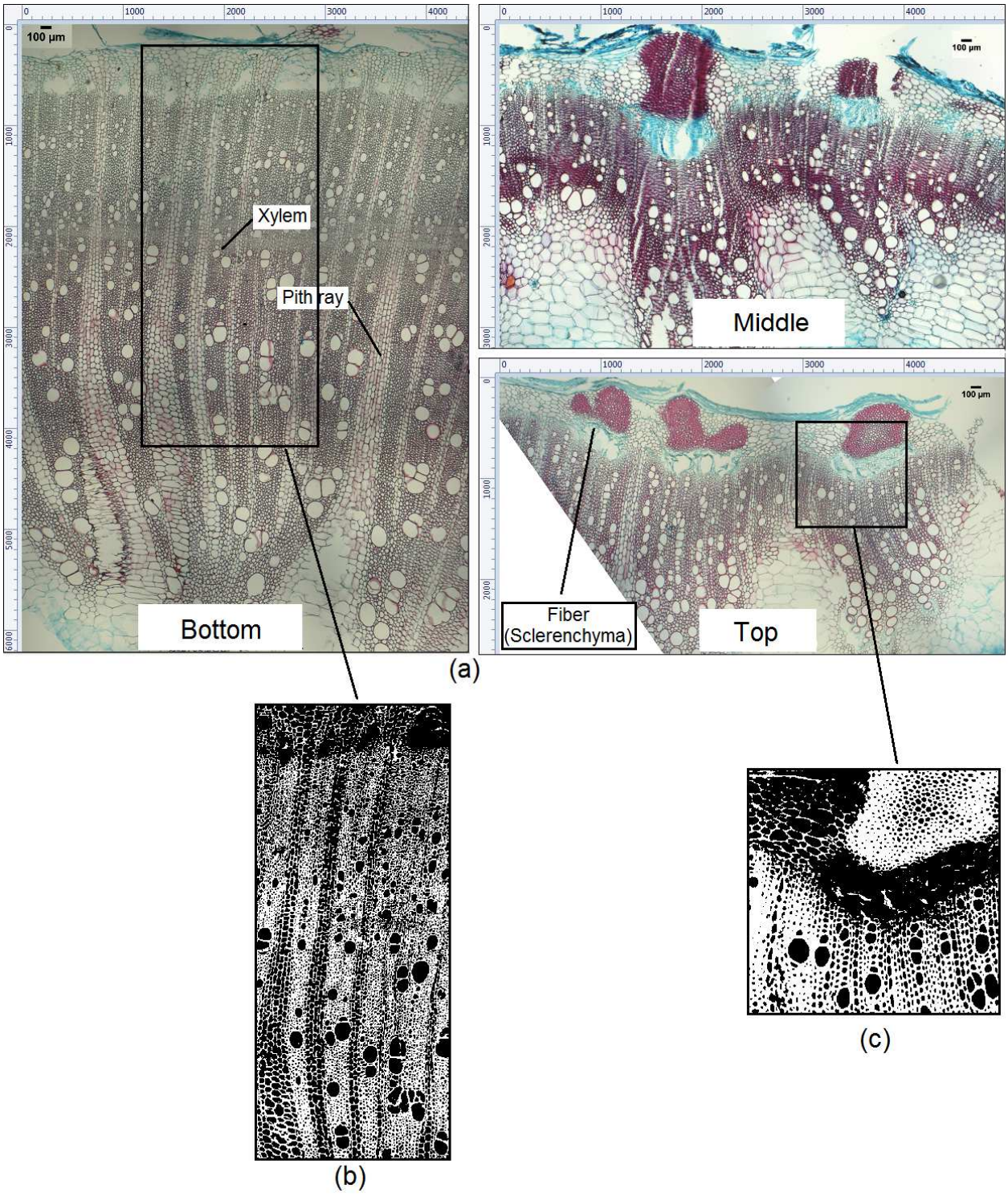

Figure 7 (a): Micrography of various cross sections of bark sampled from different locations along a stem; (b) (c): Binarized representative zones

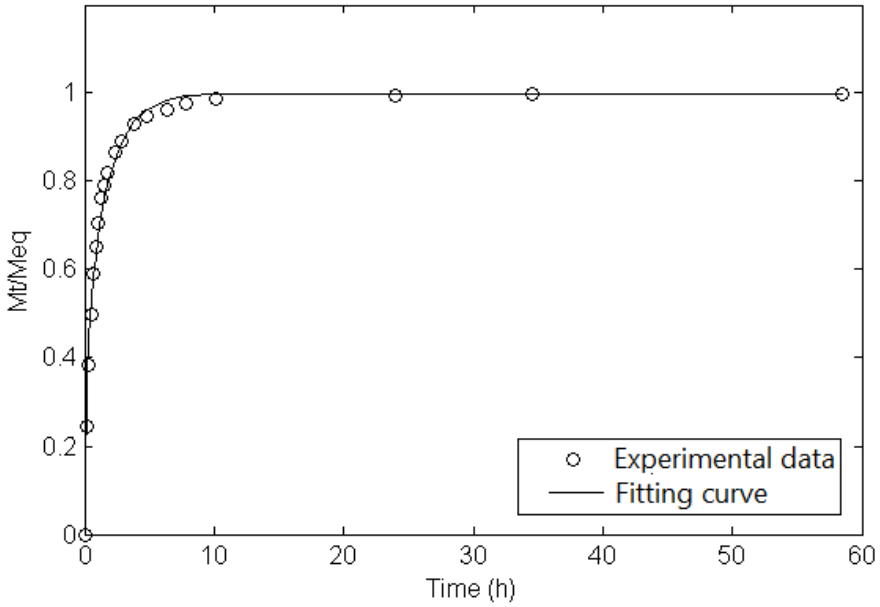

Figure 8 Typical water absorption curve for pith

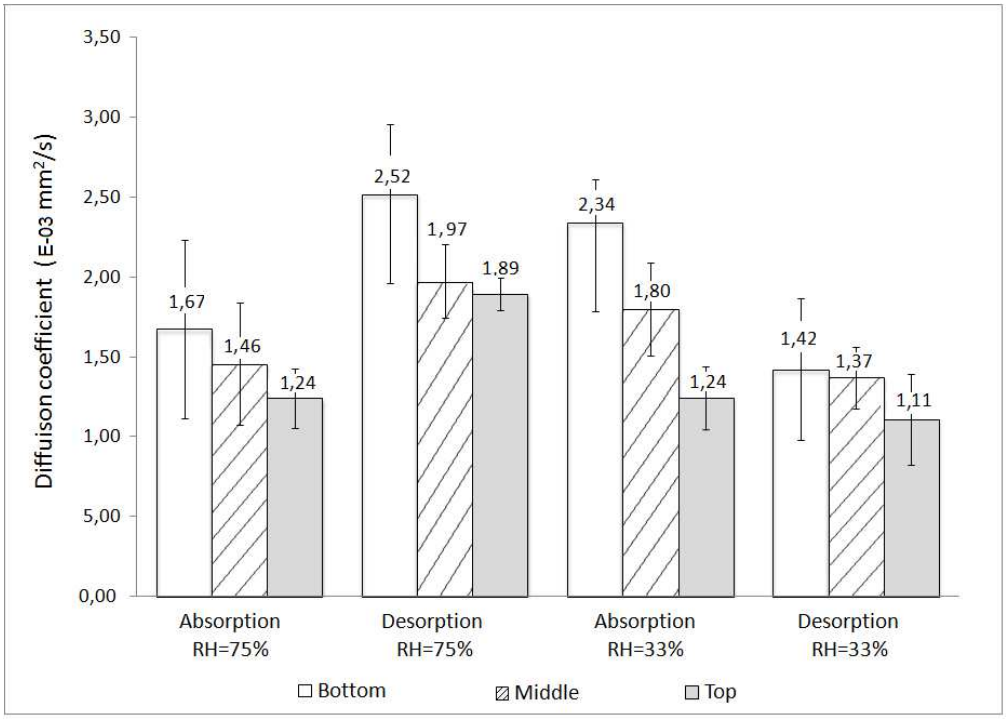

Figure 9 Diffusion coefficient determined for pith

For the pith, vapor diffusion through the cell cavities and bound water diffusion through the cell walls are the main diffusion mechanisms, as for the bark. This finding can be explained by the porosity of the specimens, which depends on location. Figure 10 shows that the bottom-sampled piths have many large cavities. Middle-sampled pith has no cavities but some wide cracks at the edge. No defect is observed for the top-sampled pith. Overall, it can be concluded that the porosity of the pith decreased *vs*. the specimen location along the stem. Hence one reason for the decrease in moisture diffusion coefficient of the pith is the decrease in porosity along the stem.

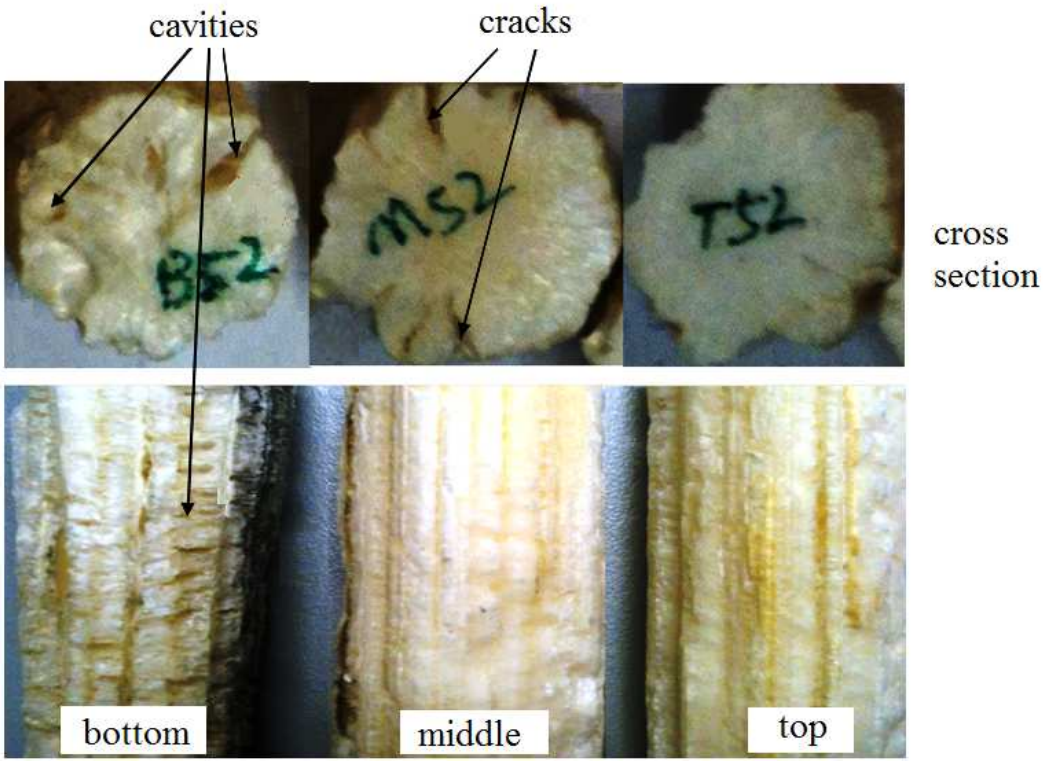

Figure 10 Pith specimens sampled at different location along a stem

3.1.3 Influence of relative humidities and absorption/desorption tests on diffusion coefficients

For both bark and pith, specimens sampled from the same location exhibited different diffusion coefficients for all the tests (absorption/desorption, 75% RH/33% RH). It has been checked that the drying procedure and hygroscopic cycles do not have a significant influence on the results of hygroscopic tests. In particular, no hysteresis effect was observed, see Figure 11. Some variations of the results may be caused by various uncontrolled factors

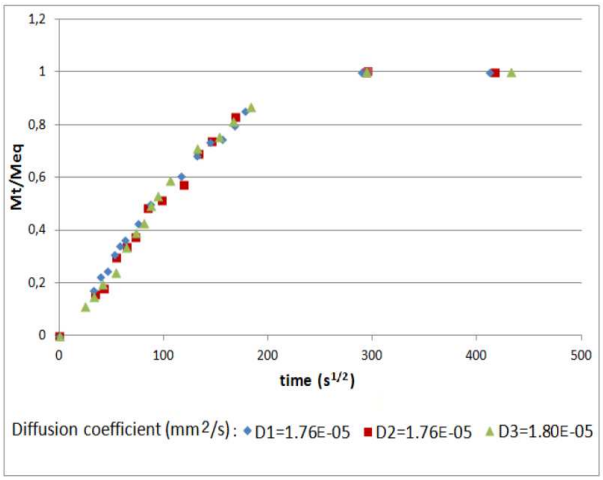

a- pith

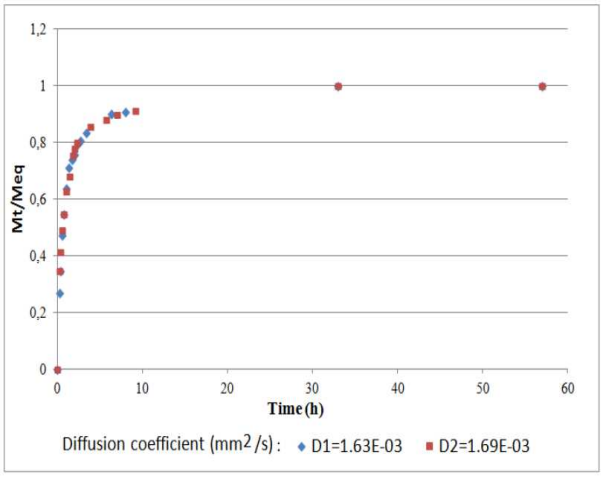

b- bark

Figure 11 Repeated absorption curves and associated diffusion coefficients D of bark and pith specimens at 33% RH

that may have influenced the experiments: room temperature and humidity, moisture concentration of specimens and air velocity around the specimens, which may favor or impede water exchanges between specimens and the outside. However, these factors are not taken into account in the diffusion equations used to determine the diffusion coefficient. However the authors have paid special attention to limit the influence of uncontrolled environmental factors (room humidity ...) by quickly weighting the specimens.

3.1.4 Moisture change during specimen mounting in the testing machine

Because the specimens tested with the micro-tensile machine were conditioned before testing under a prescribed moisture content in a chamber, the possibility arose of the moisture content within the specimens significantly changing during specimen mounting, thus leading to bias. However, taking a specimen from the chamber and mounting it in the testing machine did not take more than about one minute, and the tests themselves did not last more than one minute for both bark and pith specimens. The moisture diffusion coefficients identified in Sections 3.1.1 and 3.1.2 showed that the moisture content did not significantly evolve during this time period in either type of specimen, so no bias due to this effect could have occurred.

3.2 Mechanical test

3.2.1 Bark specimens

Figure 12 presents typical stress-strain curves obtained at several RH. The stress first evolves at a fairly linear rate. An apparent softening is visible before final failure. Young's modulus and tensile strength were deduced from the curves. These properties were obtained

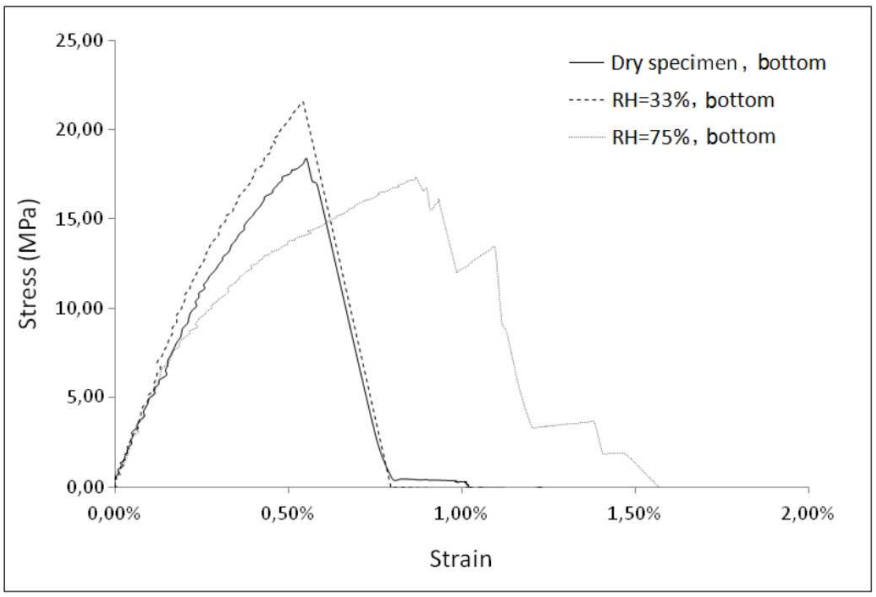

Figure 12 Typical stress-strain curves of bark specimens

from a set of 90 specimens cut from five different stems, giving ten specimens at each level and each RH (0%, 33% and 75%). Young's modulus is calculated in each case by fitting the linear part of the curve to a straight line. The tensile strength is the maximum value reached on each curve. It must be noticed that failure often occurred near the grips and not at the center of the gauge section. This is presumably due to some local fiber failures that occurred near the grips where the specimens were fixed, and which initiated cracks, causing the specimens to fail. It was found that the mean value of the ultimate strain of bark specimens for the three RH values are: 1.05%(±0.34%) at the bottom, 0.76%(±0.2%) at the middle and 0.62%(±0.15%) at the top [1]. These values do not significantly vary when the RH value changes. The influence of both the moisture content and the location of the specimens along the stems on the Young's modulus and the ultimate strength is discussed below.

Influence of the moisture content Results presented in Figures 13 and 14 show that the moisture content influences the mechanical properties of bark for all three height locations

1. The figure that represents the ultimate strain of bark is shown in Annexe A

and all three conditioning RH: 0%, 33% and 75%. Each bar in the two figures represents the mean value of 10 specimens. Specimens conditioned at 33% RH exhibit the highest Young's modulus. Whatever the height locations of the specimens, this modulus decreases when RH increases from 33% to 75%. This is consistent with results found on various species of wood [20]. This decrease in elastic modulus was due to the softening of the fiber cell walls. Water in the amorphous region of fiber reduces the interaction forces between molecules, thus facilitating molecular slippage under external effort [21]. However, results found with dry

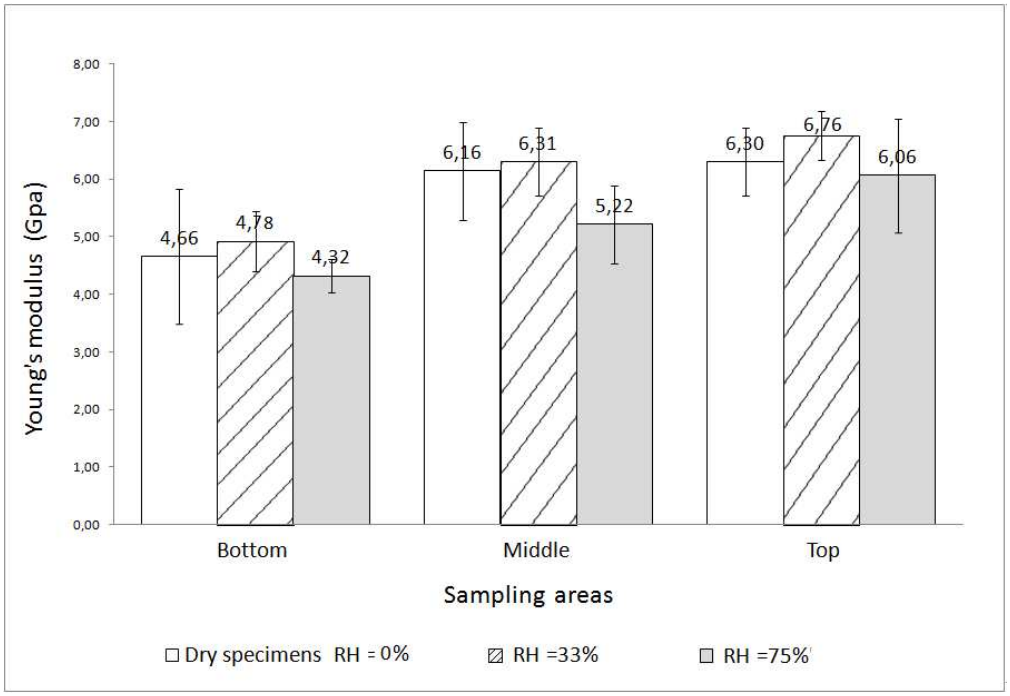

Figure 13 Young's modulus of bark

specimens did not confirm this trend. Even so, one can observe that even though the Young's modulus obtained for dry specimens is of the same order of magnitude as that obtained at 33% RH, the standard deviation in this case is significant. Hence the conclusion concerning the evolution of Young's modulus with RH is unreliable. The scatter of the results constitutes an issue which can only be tackled with suitable statistic tools applied to a much greater number of specimens than those used in the current study (see chapitre 2).

Similar trends are found for tensile strength: the highest value was found for the specimens conditioned at 33% RH. However, it must be emphasized that the changes in average values are small, and the scatter is significant. Hence it can be reasonably asserted that the moisture content has no real influence on the strength values found.

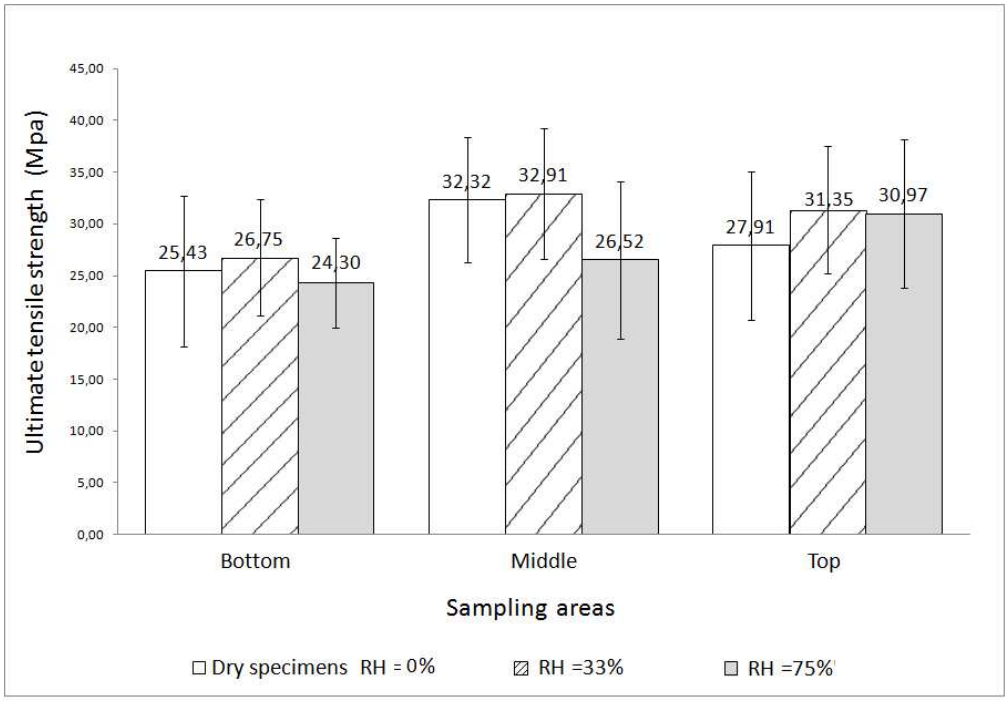

Figure 14 Tensile strength of bark

Influence of the locations of the specimens along the stems The influence of the location of the specimen along the stems on Young's modulus seems more clearcut, as it can be observed in Figure 13 that this quantity increases as the location of the specimens along the stem gose from bottom to top. This is probably due to two main effects:

- the porosity decreases along the stem, as discussed in Section 3.1.1 above (see Table 2), and so the Young's modulus understandably increases in step;
- a morphological evolution of the bark is also observed along the stem (see Figure 7). In this figure, it can be observed that:

  1. sclerenchyma and xylem fibers contained in bark increase from the bottom to the middle and top section of the stem. As described in Section 3.1.1, sclerenchyma and xylem fibers contain large amount lignin. Lignin lends stiffness to the cell walls, and so makes the fiber relatively rigid [19]. The sclerenchyma fibers seems to contain more lignin (see red color in Figure 7) and thus may be stiffer than xylem fibers. This result is also confirmed by the results of the chemical analysis stated in Section 3.1.1, in which the cellulose and lignin contents were found to be greater at the top of stems;

  2. the percentage per unit volume of sclerenchyma increases from the middle to the top of the stem. Even though there is no significant increase in amounts of sclerenchyma and xylem fibers from the middle to the top in Figure 7, Young's modulus increases

from the middle to the top. This is because the thickness of the bark (about that of the specimen tested) decreases at the same time, so the percentage per unit volume of sclerenchyma increases, and therefore so does the Young's modulus.

The ultimate strength at the bottom is slightly lower than at the middle and top. The RH value seems to have no influence on the ultimate strength, see Figure 14. A possible reason is the fact that some fibers were broken inside or close to the grips, causing early failure that did not reflect the real strength value. Changing the shape of the specimens or bonding tabs at the ends would probably limit this negative effect, but this was not readily possible here because of the curvature of the external surface of the stems, and therefore of the bark specimens. As explained above, it was decided not to polish this external surface to avoid failure or damage of sclerenchyma located at this position.

3.2.2 Pith specimens

Figure 15 shows typical stress-strain curves obtained at several RH levels. The stress evolves first in a fairly linear way. An apparent softening is then visible after the linear part.

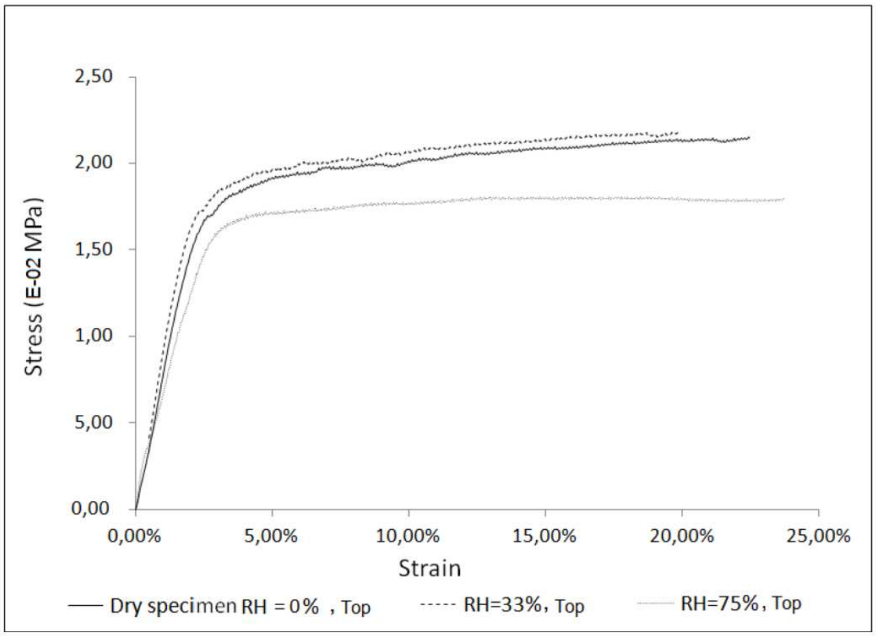

Figure 15 Typical stress - strain curves of pith specimens

The curve tends to level off before the end of the test. Young's modulus and compressive yield strength are deduced from these curves. The Young's modulus is calculated in each case by fitting the linear part of the curve to a straight line. The yield strength is obtained with an offset strain equal to 0.2%. It was found that the mean value of the yield strain of pith

specimens for the three RH values are: 2.7%(±0.75%) at the bottom, 2.78%(±0.93%) at the middle and 2.67%(±1%) at the top. At the bottom location, these values do not significantly vary when the RH value changes. However, at the middle, the values of the ultimate strains decrease when the RH value changes from 0% to 33% (yield strain changes from 3.15% to 2.83%) and from 33% to 75% (yield strain changes from 2.83% to 2.36%). At the top, the values of the yield strains decrease when the RH value changes from 0% to 33% (yield strain changes from 3.25% to 2.66%) and from 33% to 75% (yield strain changes from 2.66% to 2.10%). The influence of both the moisture content and the location of the specimens along the stems on the Young's modulus and the compressive yield strength is discussed below.

Influence of the moisture content Like the bark, pith conditioned at 33% RH exhibits the highest Young's modulus (see Figure 16), where each bar in the figure represents the mean value of ten specimens. There is a slight decrease in elastic modulus when the conditioning RH decreases from 33% to 0%. A significant decrease in Young's modulus is observed when

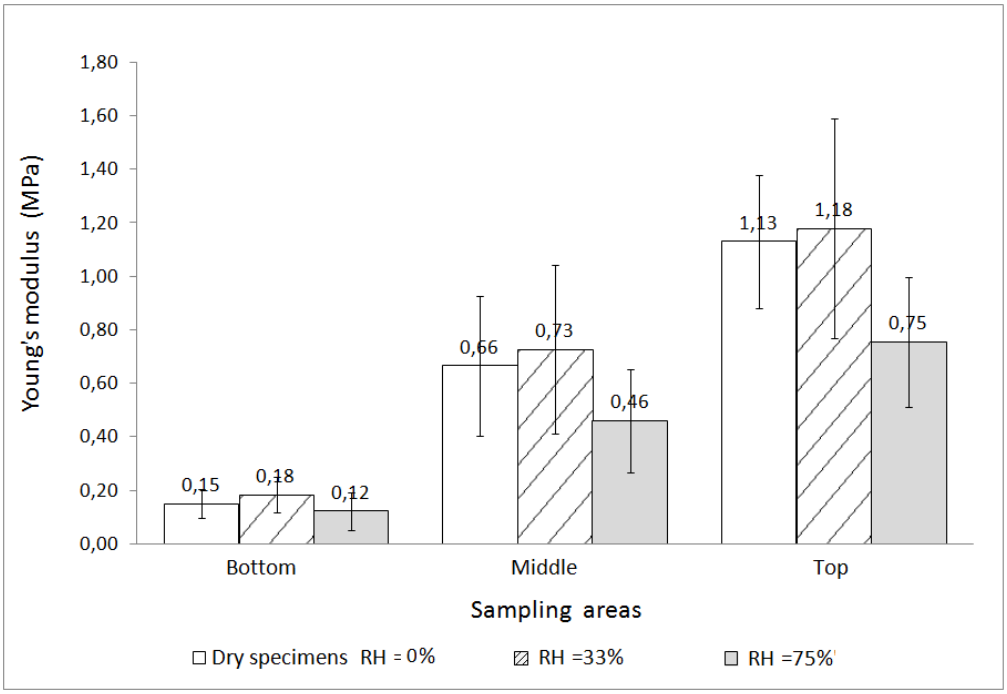

Figure 16 Young's modulus of pith

the RH for the conditioning increases from 33% to 75%. Like for the bark, this is due to the cell wall softening.

Similar trends are found for the yield compressive strength: the highest mean value is found for the specimens conditioned at 33% RH (see Figure 17, each bar in the figure presents a mean value of ten specimens). The difference between 0% RH and 33% RH is not significant

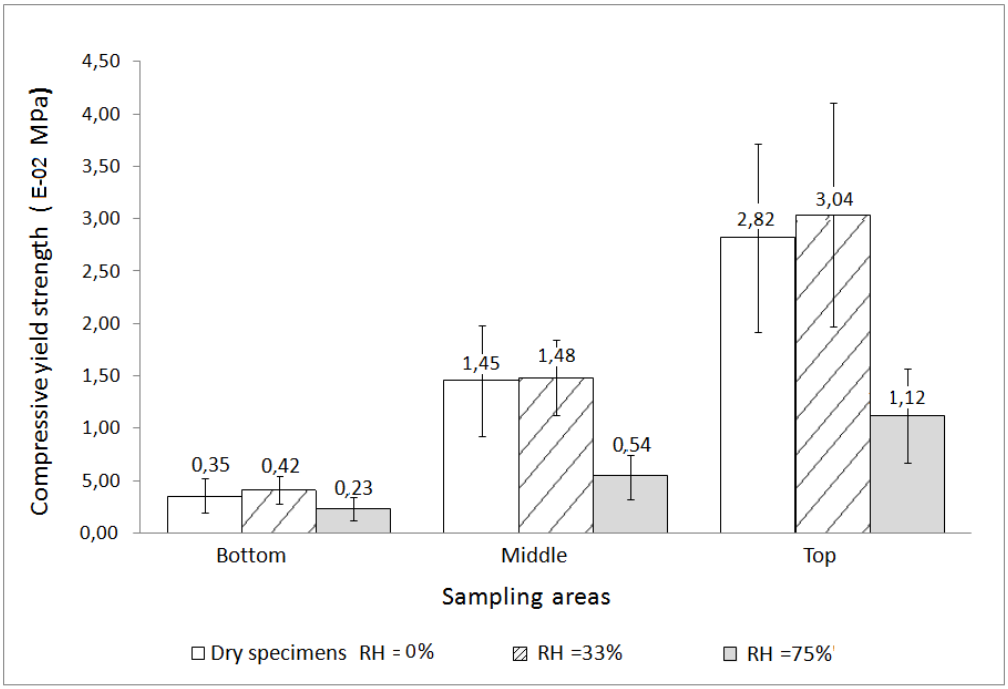

Figure 17 Compressive yield strength of pith

because of the large scatter of the results. However, the yield strength is the lowest for 75% RH.

Influence of the specimen location Figure 16 and 17 show that the Young's modulus and compressive yield strength of pith increase with the specimen location along the stem. The pith is made of only one type of cell: parenchyma. The mechanical properties of the parenchyma cell should not exhibit significant variation along the stem. Therefore, the influence of the specimen location must be mainly due to the decrease in the specimen porosity along the stem, as described in Section 3.1.2.

3.2.3 Characterization of moisture content variation during mechanical test

The specimen moisture content variations during the specimens installation were estimated from the experimental moisture diffusion coefficient found in Section 3.1.1 and 3.1.2. The time required for specimen mounting was estimated to be about 60 s. Moisture content variations were also determined by measuring the specimen weight before and after testing. Results for bark and pith are shown in Table 3 and 4. It can be observed that the moisture variations estimated by these two methods are close. These variations are not significant, and do not influence the mechanical properties presented in Sections 3.2.1 and

3.2.2.

Specimen conditioning RH	**Moisture content at equilibrium state**	**Moisture content variation** Using $D_{average}$	Experimental
75%	12.94	-0.88	-1.14
33%	4.83	-0.23	-0.23
0%	0	0.54	0.51

Table 3 Moisture content variation for bark(%)

Specimen conditioning RH	**Moisture content at equilibrium state**	**Moisture content variation** Using $D_{average}$	Experimental
75%	15.86	-1.67	-2.63
33%	6.53	-0.69	-0.31
0%	0	1.18	1.28

Table 4 Moisture content variation for pith(%)

4 Conclusion

Mechanical properties of sunflower stems were determined for different moisture contents and specimen locations. The results were analyzed according to the microstructure and chemical composition along the stem. Bark and pith exhibited different mechanical and hygroscopic properties: the Young's modulus of the bark is much greater than that of the pith, whereas the moisture diffusion coefficient of the pith is much greater than that of the bark. The specimen moisture contents influence the mechanical properties of both bark and pith: the Young's modulus and the strength are highest for 33% RH and lowest for 75% RH. These properties are mainly due to cell composition and cell morphology: bark is composed of sclerenchyma, parenchyma and xylem; pith is composed only of parenchyma. In addition, the morphological structures and porosity of both bark and pith change along the stem, corresponding to changes in both mechanical and hygroscopic properties: the Young's modulus and strength of bark and pith increased with the specimen location along the stem (going up), while the value of the moisture diffusion coefficient decreased.

Acknowledgments

The authors thank the French National Research Agency (ANR), Céréales Vallée and ViaMéca for financial support (ANR-10-ECOT-004 grant) and Pierre Conchon (INRA) for help in the microstructure observation.

Bibliography

[1] A. Mohanty, M. Misra, L. Drzal, Natural fibers, biopolymers, and biocomposites, CRC Press, 2005.

[2] M. Ardanuy, M. Antunes, J. Velasco, Vegetable fibres from agricultural residues as thermo-mechanical reinforcement in recycled polypropylene-based green foams, Waste Management 32 (2) (2011) 256–263.

[3] A. Ashori, A. Nourbakhsh, Bio-based composites from waste agricultural residues, Waste Management 30 (4) (2010) 680–684.

[4] A. Nourbakhsh, A. Ashori, Wood plastic composites from agro-waste materials: Analysis of mechanical properties, Bioresource technology 101 (7) (2010) 2525–2528.

[5] S. Panthapulakkal, A. Zereshkian, M. Sain, Preparation and characterization of wheat straw fibers for reinforcing application in injection molded thermoplastic composites, Bioresource technology 97 (2) (2006) 265–272.

[6] D. Wang, X. Sun, Low density particleboard from wheat straw and corn pith, Industrial Crops and Products 15 (1) (2002) 43–50.

[7] N. White, M. Ansell, Straw-reinforced polyester composites, Journal of Materials Science 18 (5) (1983) 1549–1556.

[8] H. Yang, D. Kim, H. Kim, Rice straw-wood particle composite for sound absorbing wooden construction materials, Bioresource Technology 86 (2) (2003) 117–121.

[9] FAOSTAT, Fao statistics division 2010: Europe sunflower seed area harvested, `http://faostat.fao.org/DesktopDefault.aspx?PageID=567`, last accessed mar, 2012.

[10] DEMETHER, Demether (anr-10-ecot-004 grant): Développement de matériaux biosourcés issus de sous-produits de l'agriculture pour l'isolation thermique des bâtiments existants, `http://demether.cemagref.fr/`, last accessed mar, 2012.

[11] J. Tiftickjian, A sunflower stem with its vascular bundles in a single ring, `http://www.doctortee.com/dsu/tiftickjian/plant-anat/stem.html`, last accessed feb, 2012.

[12] ISO483, Plastiques - Petites enceintes de conditionnement et d'essai utilisant des solutions aqueuses pour maintenir l'humidité relative à une valeur constante, NF EN ISO 483 Janvier 2006.

[13] J. Crank, The mathematics of diffusion. 2nd, Ed., Clarendon Press, Oxford, (1975).

[14] G. Park, Transport principles-solution, diffusion and permeation in polymer membranes, Synthetic membranes–science, engineering, and applications 181 (1986) 57–107.

[15] J. Young, T. Whitaker, Evaluation of the diffusion equation for describing thin-layer drying of peanuts in the hull, Transactions of the ASAE 14 (2) (1971) 309–312.

[16] MATLAB, The language of technical computing, `http://www.mathworks.com/products/matlab/`, last accessed mar, (2012).

[17] B. Time, Hygroscopic moisture, transport in wood, thesis: Norwegian Univ. of Science and Technology, (1998).

[18] ImageJ-1.440, Area measurements and particle counting, `http://rsbweb.nih.gov/ij/`, last accessed feb, (2012).

[19] M. Ek, G. Gellerstedt, G. Henriksson, Wood Chemistry and Wood biotechnology, Vol. 1, De Gruyter, (2009).

[20] C. Gerhards, Effect of moisture content and temperature on the mechanical properties of wood: An analysis of immediate effects, Wood and Fiber Science 14 (1) (1982) 4–36.

[21] D. Li, Materials Science of Fiber, China Textile & Apparel Press, Beijing, (2006).

Chapitre 2

Characterizing the variance of mechanical properties of sunflower bark for biocomposite applications

Article publié dans le journal : BioResources
Année : 2014
Numéro de volume : 9
Pages : 922-937

Introduction au chapitre 2

Le premier chapitre a permis de caractériser les propriétés hygro-mécaniques de la moelle et de l'écorce des tiges de tournesol. Les premières conclusions de cette étude ont montré une influence de l'humidité relative et de la position des éprouvettes le long de la tige sur leurs propriétés mécaniques. Cependant ces conclusions sont qualitatives du fait de la dispersion des résultats obtenus. L'objectif de ce deuxième chapitre est de caractériser cette fois-ci de manière quantitative l'influence de l'humidité relative et de la position le long de la tige sur les propriétés mécaniques. L'étude s'est focalisée uniquement sur l'écorce. Pour mener à bien cette étude statistique, plus de 800 éprouvettes ont été testées. Ce nombre important d'éprouvettes a permis d'utiliser des méthodes statistiques (identification des lois de probabilités, tests d'hypothèse, calcul de coefficient de corrélation) afin de dégager des tendances sur l'évolution des propriétés mécaniques avec un intervalle de confiance significatif.
En plus des résultats présentés dans l'article, quelques figures et tableaux supplémentaires sont présents dans l'Annexe B pour compléter l'analyse faite dans ce chapitre.

Characterizing the variance of mechanical properties of sunflower bark for biocomposite applications

Shengnan SUN[1], Jean-Denis MATHIAS[2†], Evelyne TOUSSAINT[1]and Michel GREDIAC[1]
[1] *Clermont Université, Université Blaise Pascal, Institut Pascal, UMR CNRS 6602 BP 10448, 63000 Clermont-Ferrand, France*
[2] *IRSTEA, Laboratoire d'Ingénierie pour les Systèmes Complexes 9 Avenue Blaise Pascal, CS20085, 63178 Aubière, France*
† *corresponding author. Tel. : +33 473440600 ; fax :+33 473440696, jean-denis.mathias@irstea.fr*

Abstract

Characterizing the variance of material properties of natural fibers is of growing concern due to a wide range of new engineering applications when utilizing these natural fibers. The aim of this study was to evaluate the variance of the Young's modulus of sunflower bark by (i) determining its statistical probability distribution, (ii) investigating its relationship with relative humidity, and (iii) characterizing its relationship with the specimen extraction location. To this end, specimens were extracted at three different locations along the stems. They were also preconditioned in three different relative humidity environments. The χ^2-test was used for hypothesis testing with normal, log-normal, and Weibull distributions. Results show that the Young's modulus follows a normal distribution. Two-sample t-test results reveal that the Young's modulus of sunflower stem bark strongly depends on the conditioning's relative humidity and the specimen's extraction location; it significantly decreased as the relative humidity increased and significantly increased from the bottom to the top of the stem. The correlation coefficients between the Young's modulus of different relative humidity values and of specimen extraction locations were determined. The calculation of correlation coefficients shows a linear relation between the Young's modulus and the relative humidity for a given location.

Keywords: Sunflower bark, Mechanical testing, Young's modulus, Statistical analysis, Relative humidity, Specimen extraction location

1 Introduction

In recent decades, the use of natural fibers such as wood, hemp, flax, jute, and sisal in composites has substantially increased due to growing environmental concerns; these fibers exhibit good qualities in terms of environmental safety, recyclability, low cost, and mechanical properties. These natural fibers can be classified in two groups depending on their production: primary plants and secondary plants. Primary plants are those grown for fiber production and to which agricultural fields are dedicated. Secondary plants produce a primary product, and their by-products are used as natural fibers. Agricultural by-products such as wheat straw, rice straw, and corn pith exhibit valuable environmental properties. Some of these agricultural products possess qualities similar to those of natural fibers from primary plants, and they are relatively cheaper. They are therefore being used in different biocomposite applications [1–5].

Boards made of rice husk and sawdust exhibit good material properties, such as mechanical strength and water resistance, as well as noise and thermal insulation, with a competitive price when compared to wood board. Yang et al. report that the noise and thermal insulation properties of rice straw have led to its substitution for wood in particle board and insulation board in wooden constructions [5]. Viswanathan and Gothandapani produced and tested ceiling boards from agricultural rice husk and sawdust waste [6]. They found that the produced sheets showed similar physical properties to those of commercial samples with respect to moisture content, water absorption rate, and mechanical strength. These advantages make agricultural by-products extremely competitive for use in composites, especially for industrial applications that need a compromise between mechanical properties, environmental compatibility, and cost.

We focus here on a promising agricultural by-product, sunflower stems. In Europe, sunflowers are widely cultivated for the edible oil extracted from their grains; however, there is no significant industrial use of the sunflower stems, which are shredded after the flowers are harvested. In a dry stem, the density of bark is 0.35 which is about 16 times greater than the pith. Considering a set of ten stems, it has been observed that the weight of the bark is equal to 89 ± 33 grams. This corresponds to 94% of the total mass of the stem. The abundant sources [7] and favorable mechanical properties of the bark [2] make it possible to use this by-product for bio-sourced composite materials. Nevertheless, a main drawback is the lack of its reliability due to the large variance of its properties. Hence, characterizing the variance of its mechanical properties is necessary for future biocomposite purposes.

The variance of several natural fiber properties has been already studied in the literature. The first study concerns the statistical analysis of fiber strength distribution and

fiber dimension aspect distribution using symmetrical Gaussian and non-symmetrical Weibull/log-normal distributions. Zafeiropoulos et al. have highlighted the effect of surface treatment on flax fiber strength by the analysis of variance (ANOVA) based on the assumption that fiber strength follows a normal distribution [8]. The surface treatment effect has also been studied in the case of Weibull distribution [9]. However the ANOVA method cannot be used in this latter case; thus, the significance analysis is performed only by observing whether the mean values are within confidence intervals. Both methods find that surface treatment does not significantly change fiber strength. The elementary flax fiber studies of Joffe et al. [10] and Andersons et al. [11] revealed that fiber strength is reasonably well-approximated by the two-parameter Weibull distribution. Distribution parameters were determined using the maximum likelihood method. For wheat straw fibers, a good fit was observed between fiber strength and the two-parameter Weibull distribution [1]. The dimension aspect distribution of wood pulp fibers was studied by Pulkkinen et al. with normal, log-normal, Weibull and Gamma distribution [12]. Among these, Weibull distribution was found to fit the experimental distributions. Yao et al. found that fiber length and aspect ratio distributions for all fibers in rice straw fiber-reinforced composite followed a log-normal distribution [13].

The second type of study on variance concerns the analysis of physical and structural property relationships [14]. The conclusion is that variance in the mechanical properties of flax fiber may be primarily due to the variation in the cellulose content from one fiber to another, and also to the randomness of the location and size of defects along each fiber. Concerning sunflower stem properties, it was found in a previous study [2] that the variance of the Young's modulus of sunflower bark specimens is not only due to natural variability in plants, but may also be due to the conditioning's relative humidity and to the specimen extraction location along the stem. However, the sample size was not large enough to conduct a statistical test and to give confidence in the results.

Consequently, 810 mechanical tests were conducted in the present study to provide a sufficient number of results to study the variance of the Young's modulus. In a first part, we describe the mechanical experimental set-up, including specimen preparation. In the second part, we present the statistical tools used in this study: statistical distribution histograms of Young's modulus, χ^2-test, two-sample t-test, and correlation coefficients. In the third part, both the statistical distribution of the Young's modulus and the influence of relative humidity and specimen extraction location on the Young's modulus are investigated using statistical tools applied to our experimental results.

2 Material and methods

2.1 Specimen preparation and mechanical tests

Bark specimens were extracted from different stem locations and conditioned at different relative humidity (RH) conditions before each test to evaluate the influence of these parameters on the Young's modulus of the bark.

2.1.1 Bark specimens

The sunflower species used for this study was LG 5474 (Limagrain Verneuil Holding LVH), grown in Perrier, France, in 2010. The locations on the sunflower stem where bark specimens were extracted are presented in Figure 1. Stems were selected that were 765 mm in length.

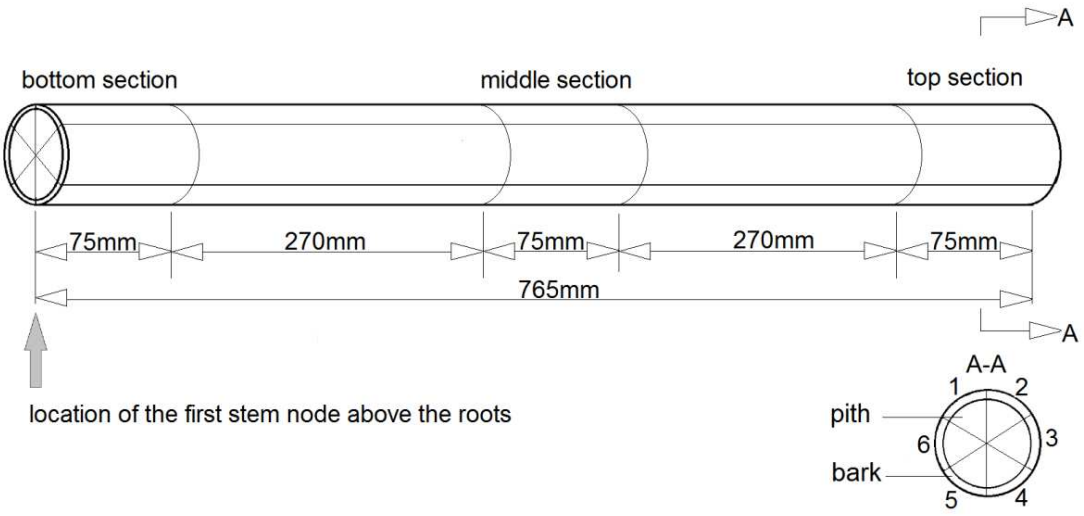

Figure 1 Specimen extraction locations

One end of the stem was the location of the first stem node above the roots. From this end of the stem, three different height sections (bottom, middle, and top) that were 75 mm in length were cut out to obtain bark specimens. Using these three sections enables the influence of the specimen extraction location on the Young's modulus to be evaluated. Each section was longitudinally divided (along the fiber direction) into six parts (see cross section A-A in Figure 1). These six parts were then processed to obtain rectangular-shaped bark specimens. For this purpose, the inner part of the bark was carefully polished with sandpaper to remove the protruding material (i.e., xylem-type tissue). This process did not influence the result of the test because the quantity of xylem-type tissue removed was small when compared to the quantity of bark. In this study, 270 bark specimens were obtained to provide sufficient

data for statistical tests. They were cut from 15 different stems. This means that there were 90 specimens at each specific height location, which accounted for one-third of the total quantity. Each specimen was conditioned at different RH for the mechanical tests and was therefore reconditioned at a different RH before each mechanical test.

2.1.2 Humidity conditioning

Specimens were conditioned in chambers at different RH values before testing to evaluate the influence of the specimen's moisture content on the Young's modulus. The RH conditioning values used for this study were 0% RH, 33% RH and 75% RH. The conditioning chamber at 0% RH was an oven set at 60 °C and equipped with P_2O_5 desiccant. The 33% RH and 75% RH conditioning chambers were constructed using the method described in ISO Standard 483:2006 [15], i.e., different saturated aqueous solutions were placed in the chambers: saturated solution of magnesium chloride for 33% RH; saturated solution of sodium chloride for 75% RH. The temperature in the chambers was equal to the room temperature. According to the experimental observations obtained in a previous study [2], specimens were kept in the chamber for at least three days to reach moisture equilibrium. The room temperature at the end of the conditioning stage was 20 ± 2 °C.

2.1.3 Mechanical tests

Tensile tests were carried out on a Deben MICROTEST 2KN testing machine (Deben UK Ltd., Edmunds, Suffolk, UK), which is suitable for testing small specimens. The machine was equipped with a 2-kN load cell. The cross-head displacement rate during the tests was equal to 2 mm/min. The clamping length was 30 mm. Specimens were carefully clamped to prevent fiber damage and to ensure that the clamping force was sufficient to avoid any test slippage. The room temperature during the mechanical tests was 20 ± 2 °C.

2.2 Statistical analysis methods

As noted above, the experimental results obtained in the study of Sun et al. [2] exhibit significant variability. We therefore proceeded to characterize this variance using suitable statistical tools. The probability distribution function was first studied to determine the variance properties of the Young's modulus obtained at each RH and specimen extraction location. Knowing the probability distribution function is also important for choosing the correct statistical method for significance testing. The RH value and specimen extraction location were examined to determine if they had a significant influence on the Young's

modulus. Finally, correlation coefficients were calculated to determine the potential statistical dependency of RH and extraction location on the Young's modulus.

2.2.1 Probability distribution test

We used histograms to determine some assumptions concerning the probability distribution of the Young's modulus of sunflower bark. A statistical hypothesis test was then performed to determine the distribution followed by the sunflower bark.

Statistical histograms In statistical analysis, the histogram, one of the most relevant graphs, visually and directly presents the frequency distribution of a dataset [16]. Hence, the frequency distribution histograms of the Young's modulus were plotted. These distribution histograms enabled us to model the probability distribution function of the data. Statistical hypothesis testing, described in the following Section (*"Statistical hypothesis testing of probability distributions"*) was performed on these datasets with the various probability distribution functions estimated from the histograms. The selection of the bin number (or bin size) is important for the representation and the description of histograms. A large bin number may generate perturbations, while a small bin number may lead to a loss of information. Previous methods for determining the bin numbers [17, 18] have these disadvantages. In the present work, we propose a method that has recently been suggested by Shimazaki and Shinomoto [19]. In the cited paper, the optimal bin number is determined by minimizing an estimated cost function obtained from a modified mean integrated square error (MISE) method. The MISE supplies the error between the estimated probability density represented by the histogram and the actual (and unknown) probability of a dataset.

Statistical hypothesis testing of probability distributions Once the statistical data had been obtained, it was necessary to determine the probability distribution. For this purpose, we used statistical hypothesis testing on the experimental Young's modulus distribution of the bark. The hypothesis testing for the probability distribution consists of the following steps:

- Stating a null hypothesis H_0: The probability distribution of the Young's modulus, $E^{RH}_{location}$, of the sunflower bark extracted at a certain location and preconditioned at a certain RH follows either a normal, log-normal, or Weibull distribution.
- Deciding whether to reject or accept H_0: The decision is often taken with a probability threshold, α, which is called the significance level. If the p-value$<\alpha$, H_0 is rejected and the difference between the probability distribution of the $E^{RH}_{location}$ and the currently

tested distribution is significant. If the p-value>α, H_0 is accepted, and the difference between the probability distribution of the $E^{RH}_{location}$ and the currently tested distribution is not significant. This means that we can not reject the hypothesis that the data follow the current tested distribution function. The α value is conventionally chosen to be 0.05 because this is the critical point between weak and strong evidence against H_0, as described by Wasserman [20]. The p-value is the probability of wrongly rejecting H_0 if it is in fact true. Thus, the p-value is also a measure of the evidence against H_0. Therefore, the smaller the p-value is, the stronger the evidence against H_0 [20]:

- p-value<0.01: very strong evidence against H_0;
- 0.01< p-value<0.05: strong evidence against H_0;
- 0.05< p-value<0.1: weak evidence against H_0;
- p-value>0.1: little or no evidence against H_0.

In the present work, the χ^2-test is conducted for hypothesis testing using the chi-squared goodness-of-fit function, $chi2gof$, in the statistical toolbox of the MATLAB software program [21]. Using this function enabled us to obtain the p-value to perform hypothesis testing. The χ^2-test is performed by assembling the data into bins, calculating the observed and expected counts for these bins, and computing the χ^2-test. The expected counts should be at least 5 to validate the χ^2 approximation. The χ^2-test is sensitive to the choice of bins. There is no optimal choice for the bin width for the χ^2-test; however, reasonable choices should produce similar results. The $chi2gof$ function of MATLAB sets the number of bins to 10 by default, and bins with an expected count less than 5 are pooled with neighboring bins until the count in each extreme bin is at least 5. The χ^2-test equation is:

$$\chi^2 = \sum_{i=1}^{N} \frac{(O_i - E_i)^2}{E_i} \tag{1}$$

where O_i are the observed counts in each bin concerned by the tested data, E_i is the expected count in each bin corresponding to the current tested probability distribution and N is the number of bins. The corresponding p-value is found in the statistical χ^2-table.

2.2.2 Significance test

The purpose of the significance test is to evaluate the significance of the differences in the mean values of the Young's modulus obtained at various locations and RH values. This allows us to determine if the specimen extraction location and the moisture content of the specimens influence the Young's modulus. Testing methods depend on the normality of the data. The two-sample Student t-test is the most commonly used method to evaluate the

differences in the means of two datasets. To use the t-test, the datasets must exhibit a normal distribution. As described earlier, the normality assumption can be evaluated by observing the data distribution (*via* histograms) and by performing a normality hypothesis test. The mean value of a dataset is denoted as $Mean(E^{RH}_{location})$. The two-sample t-test procedure consists of the following steps [20]:

- Establishing the null hypothesis H_0. For example, $Mean(E^{33\%}_{bottom}) = Mean(E^{33\%}_{middle})$ is denoted as $M1 = M2$.
- Applying the statistical test with [20]

$$t = \frac{M_1 - M_2}{\sqrt{\frac{s_2^2}{n_2} + \frac{s_1^2}{n_1}}} \tag{2}$$

  where s_1 and s_2 are the dataset standard deviations, and n_1 and n_2 are the sample sizes.
- Finding the p-value in the Student's t distribution table.
- Comparing the α value (for instance 0.05) and the p-value, as has been described earlier in Section 2.2.1. Here the difference between $Mean(E^{33\%}_{bottom})$ and $Mean(E^{33\%}_{middle})$ is significant when the p-value$< \alpha$. This test can be performed by using the two-sample t-test function, $ttest2$, in the statistical toolbox of MATLAB software program [21].

In the case of non-normality of the data, the Mann-Whitney U test (a non-parametric test of the H_0) can be performed in the place of the two-sample t-test [22]. It presents the main advantage of not requiring the assumption of normality. The U test method is different for small and large samples ($n_1, n_2 >$20). Because the present study has a large sample size, the determined U value in the test is assumed to be normally distributed. Taking the H_0 of $Mean(E^{33\%}_{bottom}) = Mean(E^{33\%}_{middle})$ as an example, the test procedure is as follows:

- Arranging the data: Arranging all the data of the two datasets $E^{33\%}_{bottom}$ and $E^{33\%}_{middle}$ into a single ranked series, then adding up the ranks of the data that come from the dataset $E^{33\%}_{bottom}$ and $E^{33\%}_{middle}$. The sums are denoted as R_1 and R_2, and they have the relationship $R_1 + R_2 = (n_1+n_2)(n_1+n_2+1)/2$;
- Determining $U = min(U_1, U_2)$ with:

$$\begin{cases} U_1 = R_1 - \frac{n_1(n_1+1)}{2} \\ U_2 = R_2 - \frac{n_2(n_2+1)}{2} \end{cases} \tag{3}$$

– Calculating μ_U and σ_U, the mean and standard deviation of U, respectively:

$$\begin{cases} \mu_U = \frac{n_1 n_2}{2} \\ \sigma_U = \sqrt{\frac{n_1 n_2 (n_1+n_2+1)}{2}} \end{cases} \tag{4}$$

– Calculating the standard normal statistic:

$$z = \frac{(U - \mu_U)}{\sigma_U} \tag{5}$$

– Determining the p-value from the statistical z-table (normal distribution): The decision rule here is the same as that described for the two-sample t-test. This test can be carried out using the Wilcoxon rank sum test function, *ranksum*, in the statistical toolbox of the MATLAB software program [21].

2.2.3 Correlation coefficient between different testing conditions

Specimens were expected to show a statistical dependence according to their extraction location and the RH. This dependence may be estimated by calculating the correlation coefficient. The correlation coefficient represents the strength of a linear relationship between the variables (in this study, the specimen extraction locations and the RH). It is calculated with the correlation coefficients function, $corrcoef(DATA)$, of the MATLAB software program [21]. $DATA$ is an N×2 matrix in which the rows are the observations and the columns are the two different testing conditions (e.g., different RH for the same specimen extraction location, or different specimen extraction locations for the same RH). N is the number of specimens for which the testing results are used. It is smaller than 90 because in the present study some specimens were damaged during the cycle of the tests. The correlation coefficient $R(i, j)$ of the 2×2 symmetric correlation matrix R is calculated as follows:

$$R(i,j) = \frac{Cov(i,j)}{\sqrt{Cov(i,i)Cov(j,j)}} \tag{6}$$

where Cov is the covariance matrix of $DATA$, and $R(i, j)$ is the correlation coefficient between two testing conditions that correspond to row i and column j in the R matrix.

3 Results and discussion

3.1 Mechanical test results

The Young's modulus of the sunflower bark tested at different specimen extraction locations and RH is now discussed. The box plot of the experimental results is presented in Figure 2. Two trends can be observed: the Young's modulus increased as the specimen

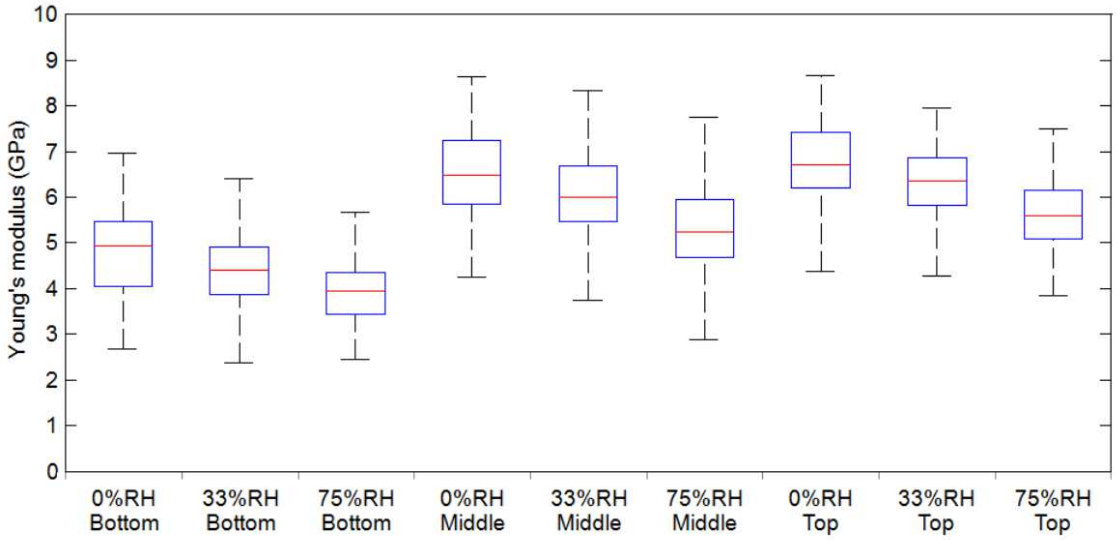

Figure 2 Box plot of the Young's modulus of bark

extraction height increased, and it decreased as the RH or the specimen moisture content increased. However, the high standard deviations make it difficult to confirm these trends. A significance test was therefore performed in order to evaluate the significance of the difference between these results (see Section 3.3) from the probability distributions determined in Section 3.2. In each case, the correlation relationship between the Young's modulus obtained for different RH and the specimen extraction location is determined. The results obtained are presented and discussed in Section 3.4.

3.2 Probability distribution function

Figure 3 represents a typical histogram and probability function plots [2]. The plotted dataset is for the specimens at 0% RH at the bottom location. In Fig. 3-(a), the fitted normal, Weibull, and log-normal distributions are superimposed. The empirical normalized cumulative distribution functions (CDF) for these three distributions are presented in Fig. 3-(b)-(c)-(d). Both the histogram and the empirical CDF plots were in good agreement with

2. The histogram and probability function plots for other test conditions are shown in Annexe B

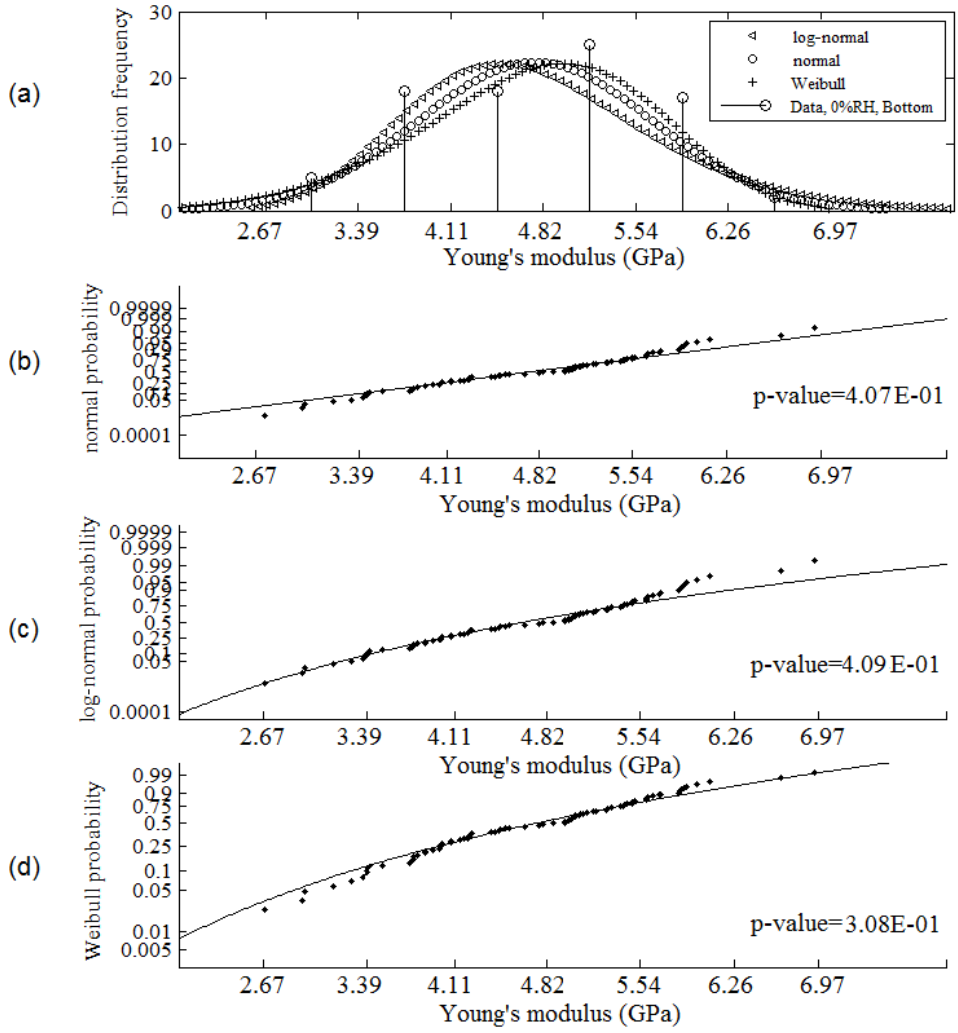

Figure 3 Histogram and probability plot at 0% RH and bottom location: (a) Histogram; (b) normal probability plot; (c) log-normal probability plot; and (d) Weibull probability plot

the fitted normal, Weibull, and log-normal distributions. Thus the nine datasets in Fig. 2 may potentially follow normal, Weibull or log-normal distributions. The objective now was to refine this first conclusion by performing hypothesis tests assuming either normal, Weibull, or log-normal distributions. It is worth recalling that: (i) the null hypothesis cannot be rejected when the p-value is greater than 0.05, and (ii) the greater the p-value, the weaker the evidence against the null hypothesis [20].

From the results of the distribution test presented in Fig. 4[3], it can be said that all the p-values were greater than 0.1. The only exception to this observation was for the 0% RH-top dataset assuming a Weibull distribution; in this case, the p-value was equal to 0.018

3. The corresponding values of the distribution test are shown in Annexe B

and thus much smaller than 0.05. This is because the observed counts were significantly lower than the expected total counts for the Young's modulus range of 4.37 to 6.09 GPa and the observed counts were greater for the range of 6.09 to 6.95 GPa. This observation can be verified by examining the details of the test results. In conclusion, the normal and

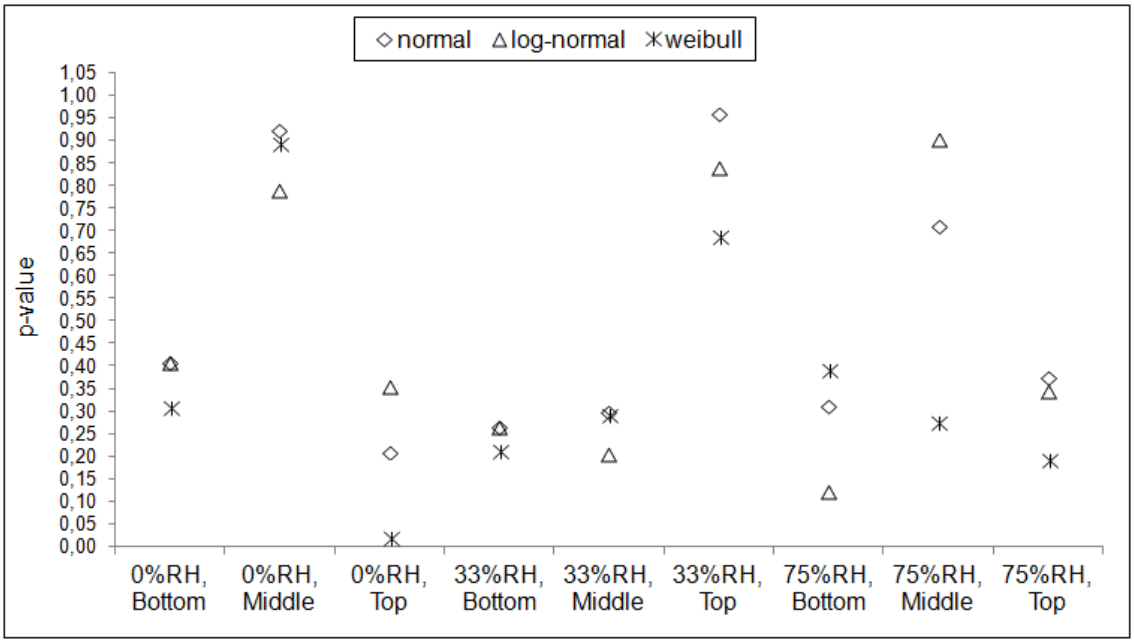

Figure 4 p-value in all distribution tests

the log-normal distributions are followed by all nine datasets. This conclusion is obtained at a 95% significance level, where α is equal to 0.05 (remembering that α corresponds to the value from which H_0 is accepted or rejected); thus, we can examine whether one of these two distributions is more representative of the datasets by comparing the p-value obtained for each of them. Among these nine datasets, six of them corresponded to a situation where the p-value of the normal distribution test was the highest, whereas the remaining three corresponded to a situation where the log-normal distribution was the highest. The p-value of the normal distribution function is, therefore in most cases, greater than that of both the Weibull and the log-normal distribution functions. This indicates that the the evidence *against* the null hypothesis that the datasets follow a normal distribution is the weakest. Therefore, the final conclusion is that the datasets are more inclined to follow a normal distribution function. The two-tailed t-test was therefore only performed for the normal distribution function to determine the influence of both the RH and the specimen extraction location. This is discussed in the following section.

3.3 Influence of RH and specimen extraction location

The influence of both the RH and the specimen extraction location is now analyzed. The $p-$value obtained from the two-sample t-test performed on the nine datasets are given in Fig. 5[4]. It can be seen that the smaller the p-value, the stronger the evidence against the

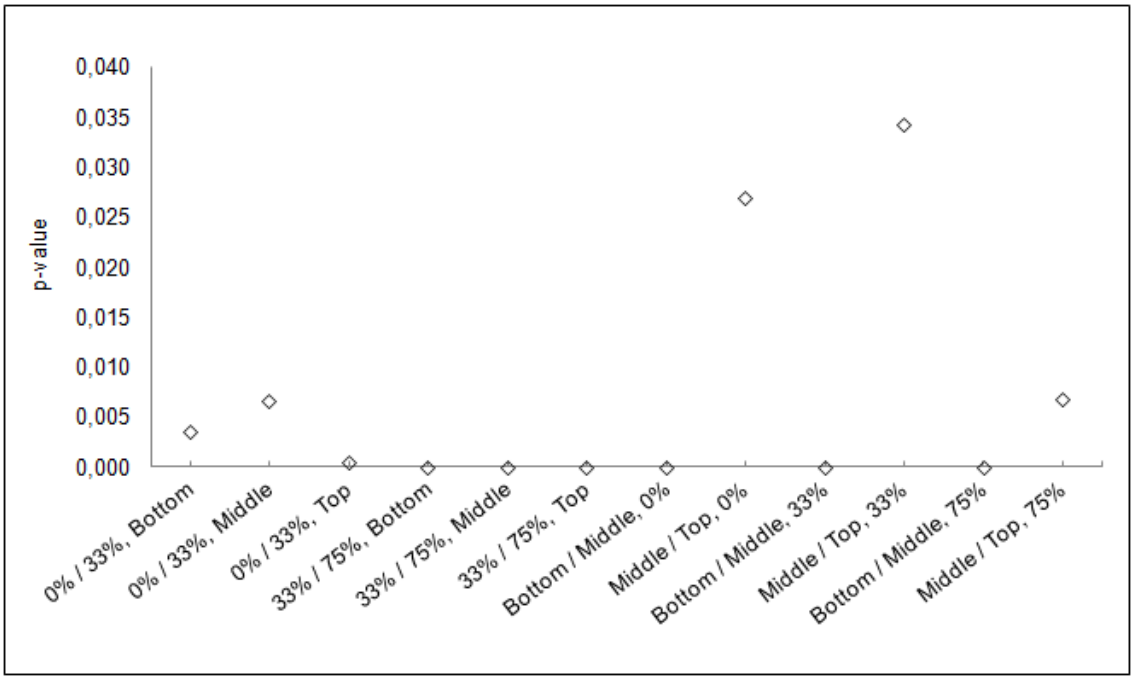

Figure 5 p-value for the two-sample $t-$test

null hypothesis. It can be observed that p-values were less than 0.035 for all the test results. This indicated that the differences between the mean values of the datasets were significant for α=0.05.

Concerning the influence of the specimen extraction location, it can be concluded from Fig. 5 that the differences between the middle and top locations for the three RH values were less significant than those between the bottom and middle locations. Indeed, the p-value of the former was the highest: $p\text{-value}^{0\%}_{middle/top}$ = 2.71E-02, $p\text{-value}^{33\%}_{middle/top}$ = 3.44E-02, $p\text{-value}^{75\%}_{middle/top}$ = 6.9E-03, and $p\text{-value}^{0\%}_{bottom/middle} = p\text{-value}^{33\%}_{bottom/middle} = p\text{-value}^{75\%}_{bottom/middle}$ $<10^{-16}$. Moreover, for the two-sample t-test between the middle and the top locations, the p-value was the smallest at 75% RH. Consequently, the difference between the Young's modulus obtained at the middle and the top locations was the most significant for this specimen's moisture content. For the influence of RH, it can be observed at the same location that the p-value of the two-sample $t-$tests between 0% RH and 33% RH is always greater than that

4. The corresponding values of the two-sample t-test are shown in Annexe B

obtained between 33% RH and 75% RH. Hence, the difference between 33% RH and 75% RH was the greatest.

In conclusion, both the specimen moisture content and the specimen extraction location have a significant influence on the Young's modulus when α=0.05. Hence, the Young's modulus significantly decreased with an increase of the specimen's RH conditioning. This confirmed the trend observed in our previous work [2]. In the latter case, it was due to the water softening the cell wall of the fiber [23]. Furthermore, the decrease was more significant when the RH value increased from 33% to 75%. This was probably because the difference between 33%RH and 75%RH is greater. It can also be said that the Young's modulus of sunflower bark tended to increase with specimen extraction location along the stem. This increase was greater from the bottom to the middle than from the middle to the top. This confirmed our earlier conclusion [2]: the increase of the Young's modulus of sunflower bark with specimen extraction location along the stems was due to the increase in the sclerenchyma content which is a rigid material and is more visible between the bottom and the middle. This observation of Young's modulus was also due to the decrease in the porosity of the bark along the stem.

3.4 Young's modulus correlation coefficient between different testing conditions

Some relevant correlation coefficients extracted from the correlation matrices are presented in Tables 1 and 2. In Table 1, the correlation that existed between the Young's modulus and the RH value is clearly evidenced for each specimen extraction location, as exemplified by the high correlation coefficient obtained in each case. In Table 2, the correlation coefficients

Correlation Coefficient between Different RH Values ($\mathbf{R}_{RH}$)				
R(0B, 33B)	R(33B, 75B)	R(0B, 75B)	mean	standard deviation
0.81	0.64	0.71	0.72	0.08
R(0M, 33M)	R(33M, 75M)	R(0M, 75M)	mean	standard deviation
0.76	0.57	0.60	0.64	0.10
R(0T, 33T)	R(33T, 75T)	R(0T, 75T)	mean	standard deviation
0.56	0.56	0.46	0.53	0.05

Table 1 Correlation coefficients between different RH values (0, 33 and 75 are 0% RH, 33% RH and 75% RH, respectively; B, M, and T are bottom, middle and top, respectively)

were much lower than in the previous case. This indicated that the correlation between the Young's modulus and the specimen extraction location was much lower than the correlation between the Young's modulus and the RH value.

Correlation Coefficient between Different Specimen Extraction Locations ($\mathbf{R}_{locations}$)				
R(0B, 0M)	R(0M, 0T)	R(0B, 0T)	mean	standard deviation
0.24	0.01	0.24	0.16	0.11
R(33B, 33M)	R(33M, 33T)	R(33B, 33T)	mean	standard deviation
0.41	0.26	0.10	0.26	0.16
R(75B, 75M)	R(75M, 75T)	R(75B, 75T)	mean	standard deviation
0.42	0.22	0.13	0.26	0.15

Table 2 Correlation coefficients between different specimen extraction locations (0, 33 and 75 are 0% RH, 33% RH and 75% RH, respectively; B, M, and T are bottom, middle and top, respectively)

This difference between correlation coefficients obtained in each case can be partially explained as follows. In the first case, the Young's modulus is obtained with the same specimens for various RH values. In the second case, however, the tested specimens are not the same because they are extracted from different stems, which can have, for instance, different maturation and growth conditions along the stem. These differences potentially induce greater variability, which partially contributes to the lower correlation coefficients.

A typical correlation curve of the Young's modulus at 0% and 33% RH is presented in Figure 6. The linear dependence is clearly visible. Similar figures can be obtained for the other RH values and locations (not shown). In each case, a linear regression equation was obtained. These equations are shown in Table 3. The average value of the slope

Linear regression of Young's modulus between different RH			
Location	RH	Linear equations	Coefficient of determination r^2
Bottom	0%-33%	$E_{33\%RH}=0.75E_{0\%RH}+0.82$	0.66
	33%-75%	$E_{75\%RH}=0.6E_{33\%RH}+1.28$	0.51
	0%-75%	$E_{75\%RH}=0.58E_{0\%RH}+1.13$	0.54
Middle	0%-33%	$E_{33\%RH}=0.68E_{0\%RH}+1.68$	0.51
	33%-75%	$E_{75\%RH}=0.56E_{33\%RH}+1.94$	0.36
	0%-75%	$E_{75\%RH}=0.47E_{0\%RH}+2.32$	0.31
Top	0%-33%	$E_{33\%RH}=0.55E_{0\%RH}+2.62$	0.54
	33%-75%	$E_{75\%RH}=0.62E_{33\%RH}+1.77$	0.31
	0%-75%	$E_{75\%RH}=0.47E_{0\%RH}+2.45$	0.26

Table 3 Linear regression of the Young's modulus between different RH

of the nine corresponding lines was 0.59 (with a standard deviation equal to 0.09). The

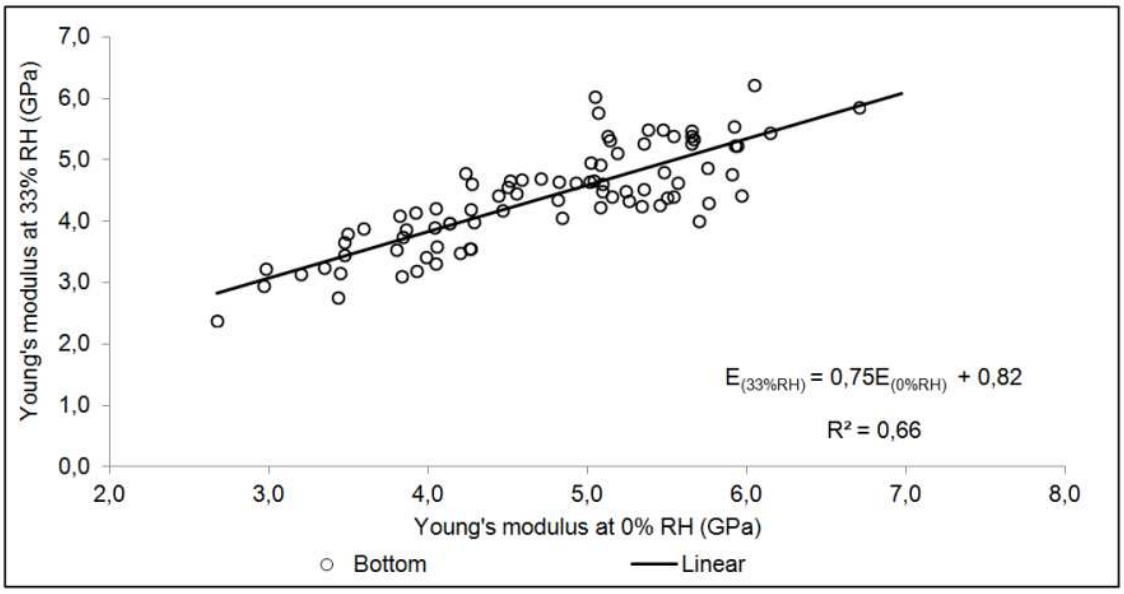

Figure 6 Correlation relationship between 0% and 33% RH at the bottom specimen extraction location

slope values tended to decrease with increasing RH between the different RH values (see column 2) and with increasing height of the specimen extraction location (see column 1). The linear regression equations representing the correlation between the Young's modulus and the different specimen extraction locations are not presented here because, as explained above, these parameters were less strongly correlated, thus leading to determination coefficients that were very small in comparison with those reported in Table 3.

4 Conclusion

- Hypothesis testing was performed on the datasets obtained in each case. Probability distribution tests showed that these datasets follow a normal distribution function.
- Significance tests showed that the Young's modulus closely depended on both the RH value and the specimen extraction location. This modulus tended to significantly increase from the bottom to the top of the stems and tended to significantly decrease with increasing RH. Statistically, the difference in Young's modulus between the bottom and middle locations was more significant than the difference between the middle and the top locations at all RH values. Furthermore, the differences in the Young's modulus between the middle and the top locations were greater for the higher RH values. The difference in Young's modulus between 33% RH and 75% RH was greater than that between 0% RH and 33% RH. This was probably because the

difference between 33% RH and 75% RH is greater.

– The correlation coefficients between the Young's modulus at various RH and specimen extraction locations were characterized. It was found that the correlation coefficient between the Young's modulus and the RH value was greater than that obtained between the Young's modulus and the specimen extraction location. Finally, the linear regression equations relating the Young's modulus to the RH values were determined, which showed the dependence of the experimental results for a given extraction location.

Acknowledgments

The authors would like to acknowledge the French National Research Agency (ANR), Céréales Vallée and ViaMéca for their financial support (ANR-10-ECOT-004 grant). The authors are also grateful to Mr. D. ZHENG for his contribution to the experimental part of this study.

Bibliography

[1] S. Panthapulakkal, A. Zereshkian, M. Sain, Preparation and characterization of wheat straw fibers for reinforcing application in injection molded thermoplastic composites, Bioresource technology 97 (2) (2006) 265–272.

[2] S. Sun, J.-D. Mathias, E. Toussaint, M. Grédiac, Hygromechanical characterization of sunflower stems, Industrial Crops and Products 46 (2013) 50–59.

[3] D. Wang, X. Sun, Low density particleboard from wheat straw and corn pith, Industrial Crops and Products 15 (1) (2002) 43–50.

[4] N. White, M. Ansell, Straw-reinforced polyester composites, Journal of Materials Science 18 (1983) 1549–1556.

[5] H. Yang, D. Kim, H. Kim, Rice straw-wood particle composite for sound absorbing wooden construction materials, Bioresource Technology 86 (2) (2003) 117–121.

[6] R. Viswanathan, L. Gothandapani, Mechanical properties of coir pith particle board, Bioresource technology 67 (1) (1999) 93–95.

[7] FAOSTAT, Fao statistics division 2010: Europe sunflower seed area harvested, `http://faostat.fao.org/DesktopDefault.aspx?PageID=567`, last accessed mar,2012.

[8] N. Zafeiropoulos, G. Dijon, C. Baillie, A study of the effect of surface treatments on the tensile strength of flax fibres: Part I. application of gaussian statistics, Composites Part A: Applied Science and Manufacturing 38 (2) (2007) 621–628.

[9] N. Zafeiropoulos, C. Baillie, A study of the effect of surface treatments on the tensile strength of flax fibres: Part II. application of weibull statistics, Composites Part A: Applied Science and Manufacturing 38 (2) (2007) 629–638.

[10] R. Joffe, J. Andersons, L. Wallström, Strength and adhesion characteristics of elementary flax fibres with different surface treatments, Composites Part A: Applied Science and Manufacturing 34 (7) (2003) 603–612.

[11] J. Andersons, E. Spārniņš, R. Joffe, L. Wallström, Strength distribution of elementary flax fibres, Composites science and Technology 65 (3) (2005) 693–702.

[12] I. Pulkkinen, K. Ala-Kaila, J. Aittamaa, Characterization of wood fibers using fiber property distributions, Chemical Engineering and Processing: Process Intensification 45 (7) (2006) 546–554.

[13] F. Yao, Q. Wu, Y. Lei, Y. Xu, Rice straw fiber-reinforced high-density polyethylene composite: Effect of fiber type and loading, industrial crops and products 28 (1) (2008) 63–72.

[14] K. Charlet, J. Jernot, J. Breard, M. Gomina, Scattering of morphological and mechanical properties of flax fibres, Industrial Crops and Products 32 (3) (2010) 220–224.

[15] ISO483, Plastiques - Petites enceintes de conditionnement et d'essai utilisant des solutions aqueuses pour maintenir l'humidité relative à une valeur constante, NF EN ISO 483 Janvier 2006.

[16] C. Chiang, Statistical methods of analysis, World Scientific Pub Co Inc, 2003.

[17] H. Sturges, The choice of a class interval, Journal of the American Statistical Association 21 (153) (1926) 65–66.

[18] D. Scott, On optimal and data-based histograms, Biometrika 66 (3) (1979) 605–610.

[19] H. Shimazaki, S. Shinomoto, A method for selecting the bin size of a time histogram, Neural Computation 19 (6) (2007) 1503–1527.

[20] L. Wasserman, All of statistics: a concise course in statistical inference, Springer Verlag, 2004.

[21] MATLAB, The language of technical computing, `http://www.mathworks.com/products/matlab/`, last accessed mar, 2012.

[22] K. Sijtsma, W. Emons, Nonparametric statistical methods, International encyclopedia of education (2010) 347–353.

[23] D. Li, Materials Science of Fiber, China Textile & Apparel Press, 2006.

Chapitre 3

Applying a full-field measurement technique to characterize the mechanical response of a sunflower-based biocomposite

Article soumis au journal : Construction and Building Materials

Introduction au chapitre 3

Une fois que les constituants de base ont été caractérisés (chapitres 1 et 2), des premiers biocomposites ont été fabriqués par l'un des partenaires du projet ANR. Le chapitre 3 est dédié à la caractérisation de ces premiers biocomposites à base de tiges de tournesol dont le liant est assuré par une biomatrice à base de chitosane. Afin de caractériser le comportement mécaniques de ce biocomposite, une méthode de mesures de champs sans contact a été utilisée : la méthode de grille. La principale difficulté rencontrée lors de cette étude est le marquage de la surface d'un tel matériau. En effet, la colle classiquement utilisée pour le transfert de grille présente une rigidité telle qu'elle aurait perturbée la réponse mécaniques en surface du biocomposite. Une nouvelle méthode de marquage a donc été développée afin de ne pas perturber la réponse cinématique du biocomposite. Plusieurs éprouvettes ont été testées avec des pourcentages massiques de chitosane différents afin de montrer l'influence de ce paramètre sur la réponse cinématique du biocomposite.
En plus des principaux résultats présentés dans l'article, des figures supplémentaires sont disponibles dans l'Annexe C.

Applying a full-field measurement technique to characterize the mechanical response of a sunflower-based biocomposite

Shengnan SUN[1], Michel GREDIAC[1†], Evelyne TOUSSAINT[1], Jean-Denis MATHIAS[2] and Narimane MATI-BAOUCHE[1]

[1] *Clermont Université, Université Blaise Pascal, Institut Pascal, UMR CNRS 6602 BP 10448, 63000 Clermont-Ferrand, France*

[2] *IRSTEA, Laboratoire d'Ingénierie pour les Systèmes Complexes 9 Avenue Blaise Pascal, CS20085, 63178 Aubière, France*

[†] *corresponding author, tel: +33 4 73 28 80 77, fax: +33 4 73 28 80 27, michel.grediac@univ-bpclermont.fr*

Abstract

This work is part of a project aimed at developing a new biocomposite material that can be used for thermal insulation purposes. This material is mainly composed of sunflower stem chips. A chitosan-based biomatrix is used as binder between them. We focuse here only on the mechanical response of this biocomposite. The goal is to investigate experimentally the link between its macroscopic response and phenomena which occur at the scale of the constituents, namely the bark and pith chips. The grid method, which is one of the full-field measurement systems employed in experimental mechanics to measure displacement and strain fields, is employed because of the very heterogeneous nature of this material. This heterogeneity is not only due to the contrast in rigidity between bark and pith, but also to the presence of voids within the material. These voids, as well as the presence of pith, lead us to develop and employ a specific marking procedure for the specimen surface under investigation. Two values for the mass percent fraction of chitosan are investigated, to observe the influence of this parameter on the global stiffness of the material and on local phenomena that occur in its bulk. The full-field measurement technique employed here leads us to detect and quantify significant heterogeneities in the strain fields, which are closely related to the material heterogeneities themselves.

Keywords:biocomposite, biomatrix, chitosan, composite, displacement and strain measurements, grid method, sunflower

1 Introduction

This work deals with the mechanical characterization of biocomposites composed of sunflower stems and a biomatrix derived from chitosan. This type of composite is being developed initially for building thermal insulation purposes, but panels made of this material must exhibit minimum mechanical properties to be able to sustain various mechanical loads such as dead weight or local stress peaks due to the wall-mounting process. In addition, this material features a very low density (about 0.17), so it is necessary to study its specific mechanical properties for applications other than thermal insulation only, as is the case for other insulating materials, see for instance [1, 2] for mineral wool.

From an economic point of view, one of the main interests of such a material is the fact that sunflower stems are agricultural by-products which are potentially cheap and abundant. Using such environmentally-friendly products in construction is becoming more and more popular in civil engineering, as illustrated by numerous papers recently published in this field [3–10]. The biocomposite studied here is very heterogeneous, with local heterogeneities mainly due to the fact that stems are made of stiff bark and soft pith [11, 12]. The stems are generally ground during the sunflower harvest, and the resulting chips are some millimeters in size. Characterizing the mechanical properties of this biocomposite by using "classic" mechanical tests has been carried out in a separate study, presented in Ref. [13]. The main result is that this biocomposite amply fulfills the requirements in terms of mechanical properties for insulating materials, such as a minimum strength value of 50 kPa [14].

The aim of the present study is to understand the link that exists between local phenomena that occur in such very heterogeneous materials and the global mechanical behavior of the biocomposite at a macroscopic scale. A full-field measurement system was employed for this purpose during compression tests performed on small briquettes made of this material, in order to see if a difference could be detected between the mechanical responses of the components of the sunflower stems, namely bark and pith, and to ascertain the role played by the voids which are present in this material. This can help establish a link between the local and global response of the tested briquettes.

One problem here is that the size of the sunflower chips (some millimeters), the amplitude of the local displacement and strain throughout the specimens reached during the tests and the spatial resolution of the full-field measurement systems which are easily available in the experimental mechanics community make it difficult to obtain reliable information on the sought displacement/strain fields. The grid method was employed here to face this

challenge. This technique consists of retrieving the displacement and strain maps by marking the external surface of the tested specimen with a regular grid. The grids usually employed for this technique are transferred using a layer of adhesive [15], and they could not be used in this study because the stiffness of the pith is very low [11]. Grids were therefore painted directly onto the surface, which was sanded and prepared specifically beforehand. It was shown that this technique enables us to detect and quantify significant local strain gradients and movements of stem chips. This information was finally analyzed with respect to the global response of the specimens during the tests.

2 Material, specimens and testing conditions

The biocomposites studied here were obtained by mixing bark and pith chips with a biomatrix derived from chitosan [16–18]. Bark and pith chips were first placed in a plastic container. The desired quantity of biomatrix was then added and mixed with the chips by hand using a stainless spatula. The bark was expected to provide the main contribution to the mechanical properties of the biocomposite in terms of stiffness and strength. The pith provides the main thermal insulation properties. A biopolymer constitutes the matrix of this bio-based composite material, which is totally derived from renewable resources.

Sunflower stems are abundant, since the world sunflower crop production reached 24.84 millions ha in 2012 [7]. This plant is thus widely cultivated. Some other plants, such as hemp and flax, are grown in dedicated agricultural fields mainly for fiber production purposes. Nowadays, these fibers are used for their interesting mechanical properties in composite materials [20–22]. On the contrary, sunflower stems are agricultural by-products, the primary product being the flower itself, used in oil production. Consequently, this material does not require specific agricultural fields, is already available and exhibits valuable environmental properties. Sunflower stems constitute therefore a raw material which is cheap, in addition to being abundant [23].

Polymeric matrices used in composites, such as epoxy and polyester, are based on petrochemical resources and made of volatile organic and/or toxic compounds. On the other hand, chitosan is a biopolymer (more precisely a polysaccharide) derived from the shells of sea crustaceans such as shrimps or crabs. It is widely commercially available and potentially cheap, depending on the quality and quantity purchased for a given application. It was recently shown that chitosan could be employed in association with other chemical components to obtain various types of resins featuring interesting mechanical properties. These are comparable to the properties of materials employed for semi-structural (if not structural) applications [16–18]. The characteristics of the biomatrix employed here were

adjusted to reach viscosity and wettability values suitable for bark and pith chip impregnation [24]. It is worth noting that the solvent for this biomatrix is simply water containing a low percentage of acetic acid (1%).

Two mixes were considered in this study. They are defined by the mass percent fraction of chitosan, which was equal to 6.25% or 4.15%. Note that this percentage is rather small; it is however important to observe its impact on the mechanical properties to try to limit the amount of biomatrix employed to prepare this biocomposite. The reasons are manifold: the cost of chitosan is greater than that of sunflower stem chips, its environmental impact is higher [25] and its insulating properties are lower [24].

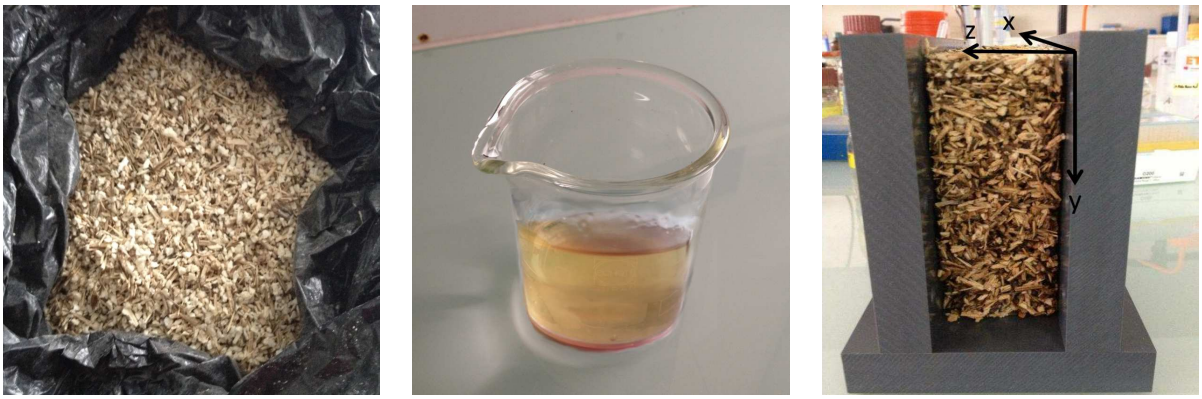

a- bark and pith chips b- chitosan-based biomatrix c- side view of mould with specimen inside

Figure 1 Constituents and mould. Compression tests and compaction are performed along direction y. The grid is painted in the $x - y$ plane after demolding and preparation of the surface.

The size of the bark and pith chips used to prepare this biocomposite were calibrated: they measured between 3 and 5 mm to avoid being either too small or too large. Such calibrated chips were separated from the others (larger or smaller chips) using sieves. The obtained mixes were placed in a small mold, whose dimensions were $x \times y \times z = 50 \times 92 \times 180$ mm^3. Note that 120 g of bark and pith and 200 ml of biomatrix are necessary to prepare a specimen. A compaction pressure of 32 kPa was applied along the y direction before drying. After drying, briquettes were obtained. They were cut with a band saw to obtain the desired dimensions for the tested specimens: about $50 \times 80 \times 122$ mm^3. Figure 1 gives an overview of the different constituents and the mold used to prepare the specimens. More details on biocomposite preparation are given in Ref.[13].

Typical results obtained with two specimens by mixture are given and discussed in this study. The specimens are numbered $i - j$ in the following, where $i = 1$ for a mass percent

fraction of chitosan equal to 6.25% and $i = 2$ for a mass percent fraction of chitosan equal to 4.15%. j is the number of the specimen for each mix i.

It must be pointed out that the biocomposite under study features numerous voids, which are clearly visible to the naked eye, see Figure 2-a for instance. These voids cannot be considered as defects if their volume fraction remains low. The reason is that this composite is developed to be employed as a thermal insulant. Various numerical simulations on a model constructed using SALOME software [26] and carried out with ASTER finite element software [27] (results not discussed here) have shown that voids, within certain limits, have no real effect on the thermal insulation properties of the original mixes, or at most only slightly impair these properties [28]. The thermal conductivity measured with the hot-wire method [13] is equal to about $\lambda = 0.06$ W/mK [13]. This is slightly greater than that of various synthetic materials commercially available for insulation purposes, such as glass-wool ($\lambda = 0.04$ W/mK) or extruded polystyrene ($\lambda = 0.03$ W/mK) [29], but it remains lower than the threshold value beyond which materials are no longer considered as insulating materials: $\lambda = 0.10$ W/mK.

a- raw surface after cutting with sealant and sanding

b- front face after
filling with sealant and sanding

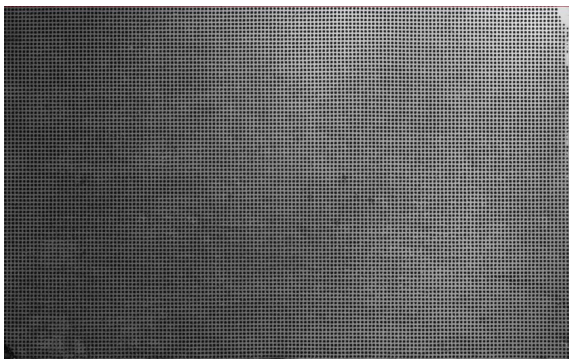

c- grid paint on the front face of the
specimen after filling with sealant and sanding

Figure 2 Front face of Specimen 1-1

The specimens were subjected to compression tests performed using a ±20kN Zwick-Roell testing machine. The tests were displacement-controlled with a cross-head speed equal to 0.02 mm/s, the maximum imposed displacement being equal to 4 mm. The tested specimens rested on a small steel plate located at their bottom and the load was applied by imposing a displacement on the upper side, a stiff steel plate being placed on the upper side of the specimen to help obtain homogeneous imposed displacement and pressure on this side. Note that since the lower and upper sides were not parallel, a 2 mm thin elastomer sheet was placed between the upper side of the specimens and the moving plate to accommodate the displacements imposed on the upper side.

Heterogeneous stress and strain fields were expected to occur in these specimens because of the very heterogeneous nature of this type of composite material. A full-field measurement method was therefore employed to detect and quantify these heterogeneities. However, the presence of voids, the size of the constituents, the softness of these constituents and the fact that most of the full-field measurement systems are devoted to 2D-measurements, make this type of measurement very challenging. Some preliminary measurements performed with digital image correlation (DIC) [30] showed that the compromise between spatial resolution in the strain maps (defined here by *the shortest distance between two spatially independent measurements) and resolution (defined here by the change in quantity being measured that causes a change in the corresponding indication greater than one standard deviation of the measurement noise [31]), was not suitable for the current application, the strain level in the different constituents being indistinguishable.* It was therefore decided to employ another technique, namely the grid method, to perform these measurements. The principle of this technique is briefly recalled in the following section.

3 Measuring displacement and strain fields using the grid method

3.1 Principle

The grid method consists first of depositing a grid on the surface of the specimen under investigation. The idea is then to capture images of this grid with a camera and to extract displacement and strain fields from the grid images while the specimen under test deforms. Indeed displacements are directly proportional to phase changes between two grid images, and thus deformations are directly proportional to the space derivatives of these changes. The phase changes between two images, denoted $\Delta\Phi_x$ and $\Delta\Phi_y$, are related to the in-plane

displacements u_x and u_y through the following equations [32, 33]

$$\begin{cases} u_x = -\dfrac{p}{2\pi} \times \Delta\Phi_x \\ u_y = -\dfrac{p}{2\pi} \times \Delta\Phi_y \end{cases} \tag{1}$$

where p is the pitch of the grid. The in-plane strain components are therefore deduced from the phase derivative variations using the following equations:

$$\begin{cases} \epsilon_{xx} = -\dfrac{p}{2\pi} \times \Delta\dfrac{\partial\Phi_x}{\partial x} \\ \epsilon_{yy} = -\dfrac{p}{2\pi} \times \Delta\dfrac{\partial\Phi_y}{\partial y} \\ \epsilon_{xy} = -\dfrac{p}{4\pi} \times \left(\Delta\dfrac{\partial\Phi_x}{\partial y} + \Delta\dfrac{\partial\Phi_y}{\partial x}\right) \end{cases} \tag{2}$$

Phases can be deduced from grid images using an image processing technique based on the windowed Fourier transform (WFT), which is defined as follows [33]:

$$\begin{aligned} \Psi(x,y,\theta) &= \int_{-\infty}^{+\infty}\int_{-\infty}^{+\infty} s(\xi,\eta) g_\sigma(x-\xi, y-\eta) e^{-2i\pi f(\xi\cos(\theta)+\eta\sin(\theta))\xi\eta} \\ &= R(x,y,\theta) + iJ(x,y,\theta) \end{aligned} \tag{3}$$

where s is the gray level at each pixel of the grid image. $\Psi(x,y,\theta)$ is a complex number calculated at every pixel of the camera sensor. Its change in argument between reference and current grid images enables us to determine the displacement at every pixel along a direction which depends on θ (x for $\theta = 0$, y for $\theta = \dfrac{\pi}{2}$), as briefly explained below. R and J are the real and imaginary parts of Ψ respectively, and g_σ is a 2D window function. It is symmetric, positive, and integrates to 1. In practice, this window can be a triangle, as suggested in [33], or a Gaussian, as in [34, 35]. A Gaussian function is used in the current work. f is the frequency of the grid. It is defined by the inverse of its pitch. Parameter θ can be equal to either 0 or $\dfrac{\pi}{2}$, depending on the direction under consideration: x or y, respectively. The actual phase changes $\Delta\Phi_x(x,y)$ and $\Delta\Phi_y(x,y)$ are approximated by $\Delta\widetilde{\Phi_x}(x,y)$ and $\Delta\widetilde{\Phi_y}(x,y)$ which are obtained as follows:

$$\begin{cases} \Delta\widetilde{\Phi_x}(x,y) = \Delta\arctan\left(\dfrac{J(x,y,0)}{R(x,y,0)}\right) \\ \Delta\widetilde{\Phi_y}(x,y) = \Delta\arctan\left(\dfrac{J(x,y,\pi/2)}{R(x,y,\pi/2)}\right) \end{cases} \tag{4}$$

It is shown in [36] that $\Delta\widetilde{\Phi_x}(x,y)$ and $\Delta\widetilde{\Phi_y}(x,y)$ are actually first-order approximations of the convolution of the actual phase changes $\Delta\Phi_x(x,y)$ and $\Delta\Phi_y(x,y)$, by the envelope of the kernel used in the WFT. This means that even though the phases are calculated pixel-wise, the distance between two independent measurements is not equal to one pixel, since the actual value at a given point is influenced by the value at the pixels located in its neighborhood, thus causing the displacement maps, and mainly the strain maps, to be blurred. Unblurring the maps is theoretically possible by deconvolution [37] but this procedure could not be applied here, the noise corrupting the maps not being accurately characterized.

Note finally that the grid method has been improved [38] and successfully used with different variants in the recent past to characterize various types of materials, such as concrete [39], composites [40], steels, and structures such as pipes [41]

3.2 Surface preparation

As mentioned in Section 2 above, there are voids in the biocomposite and some of them are clearly visible on the front face of the specimens to be tested, see Figure 2-a for instance. Since a 2D measuring system was used in this study, it was decided to fill these voids with sealant (Sikaflex-11FC+, Le Bourget, France). The Young's modulus of this material is very low: E = 0.6 MPa and the deformation at failure is equal to 700% [42]. The impact of this filling material on the response of the specimen is therefore expected to be negligible. After filling the voids with sealant, the surface was carefully sanded and cleaned (see the surface after filling the voids and sanding in Figure 2-b). In recent studies where displacement and strain maps were measured using this technique, surface marking was generally obtained by transferring a grid, using for instance the technique described in [15]. The problem is that a layer of adhesive is necessary in this case. This marking technique is therefore not directly applicable here because the Young's modulus of this adhesive is much more higher than that of the biocomposite. It was therefore decided to paint the grid directly onto the surface using a stencil (Chiropo pochoire, Le Thor, France) [5]. White paint (Peintures Techniques Julien, Montataire, France) was first sprayed on the surface of the specimen. The stencil was then placed on this surface and black acrylic ink (Ref. 28702, Schmincke, Erkrath, Germany) was sprayed though the stencil with a V type Paasche airbrusher (Paasche Airbrush Company, Chicago, IL, USA). The minimum size of the square holes that can be cut in the stencil is the limitation of this technique here. It is equal to 0.4 mm. This finally leads to a grid featuring a frequency of 1.25 lines/mm, thus a nominal pitch equal to 0.8 mm. Figure 2-c shows the grid obtained after painting.

Note that the approach described in Section 3.1 above relies on a perfectly regular marking

5. Details concerning the surface preparation are presented in Annexe D

of the surface, but actual grids are not perfect. In particular, defects such as slight pitch changes are observed on the grids. They are detected by the WFT within certain limits, and might be considered as caused by a fictitious straining of the tested material beneath the grid. This artifact was eliminated here by using the procedure described in [34, 35].

3.3 Metrological performance of the measuring technique

The grid pitch given above enables us to estimate the spatial resolution of the measuring technique. It is important to know this quantity in the current study, for which small constituents are involved and expected to deform in different ways. Using the classic "3-sigma rule" [43], the spatial resolution can be estimated as being equal to 6 times the standard deviation σ of the Gaussian envelope used in the WFT. This standard deviation is equal here to the pitch of the grid, thus $\sigma = 9$ pixels, since the pitch of the grid is encoded with 9 pixels (see Section 3.4 below). Note that taking the standard deviation as equal to the pitch of the grid is the minimum value that can be used with a Gaussian envelope, as rigorously demonstrated in [36]. The spatial resolution is thus equal to $0.8 \times 6 = 4.8$ mm or $9 \times 6 = 54$ pixels. It means that an independent measurement is found every 4.8 mm or 54 pixels in the image, even though a different value for displacement or strain is displayed at every pixel. Note that the 3-sigma rule is somewhat conservative. The 2-sigma rule provides 3.2 mm (or 36 pixels) for the spatial resolution. In either case, the displacement and strain maps are convolved, as demonstrated in [36], and the kernel for this convolution is, as a first approximation, the Gaussian envelope used in the WFT [36]. This causes the noise to be erased and the images to be smoothed, and thus blurred. Since the size of the constituents has approximately the same order of magnitude as the spatial resolution of the measurement technique, actual details in the strain maps within each chip cannot be captured, but contrast in strain between phases can be detected, and mean values for the strain in the constituents can be considered for the analysis of the mechanical response.

3.4 Image acquisition

A SENSICAM QE camera featuring a 12-bit/1040×1376 pixel sensor was used to capture the images of the grid. A 105 mm SIGMA lens was mounted on the camera. The camera was fixed on a mounting plate whose location could be precisely changed using two adjustment screws. The grid period was digitized with 9 pixels, so the maximum size of the field that could be investigated was about 92×122 mm^2. It was therefore possible to measure the strain field on the whole gauge section of the specimen, since its dimensions were equal to 80×122 mm^2. The optical magnification was thoroughly adjusted in such a way that

the desired value of 9 pixels per period was achieved throughout each grid image before deformation. Adjusting this magnification (as well as the perpendicularity of the observation axis) relies on a trial-and-error procedure. The number of pixels was checked each time the camera was moved perpendicularly to the observed grid, using the setting screw of the camera mount, or was slightly rotated thanks to the ball joint located at the top of the tripod. The grid was illuminated by three flexible and movable light guides fed by a KL 2500 LCD cold light source (Schott, Mainz, Germany) which provided quasi-uniform lighting of the grid. These preliminary settings enabled a maximum use of the dynamics of the camera.

4 Results

4.1 Global response

The mean strain ϵ_{yy}^{mean}/mean stress σ_{yy}^{mean} curve is first analyzed, where y is the vertical axis and x the horizontal one. The mean stress is merely the ratio between the applied load and the cross-section of the specimen. The mean strain is calculated as follows. A small displacement of the lower support of the specimen being observed, the mean strain is obtained by measuring the mean displacement along a line of pixels located 30 pixels under the top face of the specimen to avoid possible edge effects, subtracting this displacement from the mean displacement along a line of pixels located 30 pixels above the bottom face of the specimen, and dividing the obtained result by the distance between these two lines of pixels. Comparing the mean strain measured by applying the procedure described above and that deduced from the displacement of the moving grip provided by the testing machine shows that the former is lower, as illustrated in Figure 3-a for Specimen 1-1 (similar results were obtained for the other specimens, so they are not shown here). The first curve is obtained with this definition of the mean strain given above, the second one with the mean strain provided directly by the testing machine. It can be seen that the apparent stiffness deduced from the second curve (the apparent stiffness is directly the ratio between stress and strain) is lower than with the first curve, which is a consequence of clearance take-up that occurs during the first stage of the test. All the curves shown in the following figures were obtained with the first procedure to avoid the influence of clearance take-up. It is worth noting that both curves in Figure 3-a are non-linear, which illustrates a progressive apparent softening of the material, which is interpreted below as an effect of damage.

A residual strain appeared after unloading. This cannot be observed in Figure 3-a because the force could not be recorded by the testing machine during unloading. This phenomenon is however visible in Figure 3-b, where ϵ_{yy}^{mean} vs. the number of the image is shown. ϵ_{yy}^{mean} increases at a fairly linear rate, which is a consequence of the fact that the test is displacement-

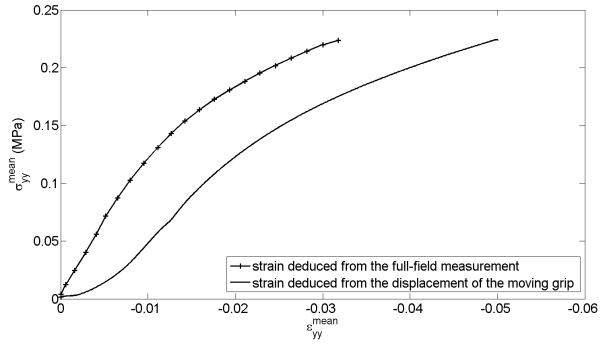

a- σ_{yy}^{mean} vs. ϵ_{yy}^{mean}. ϵ_{yy}^{mean} deduced from the displacement maps or given directly by the testing machine

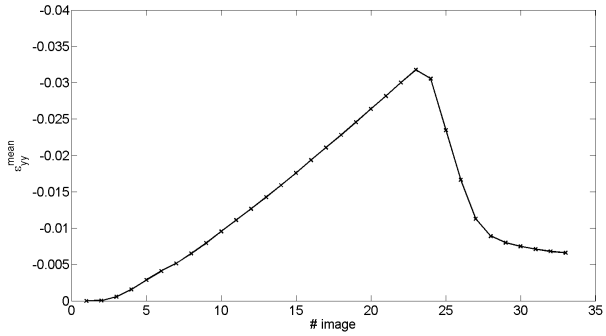

b- ϵ_{yy} vs. image #

Figure 3 Global response for Specimen 1-1

controlled. A residual strain equal to about 0.5% can be seen at the end of the test. It is not due to a viscoelastic effect, since the residual strain remains a long time after the end of the test (not shown here), but to irreversible degradation of the material during the test.

Figure 4-a shows the curves obtained for the four specimens during their first loading. The influence of the mass percent fraction of chitosan is visible. The beginnings of these curves

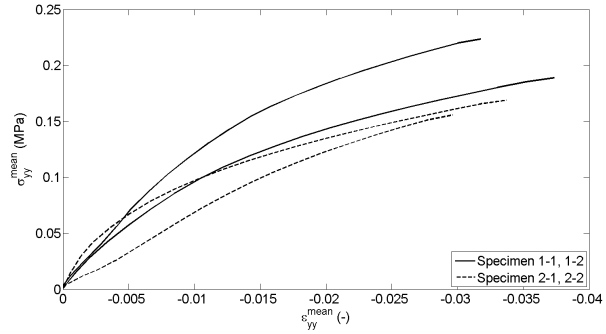

a- first load

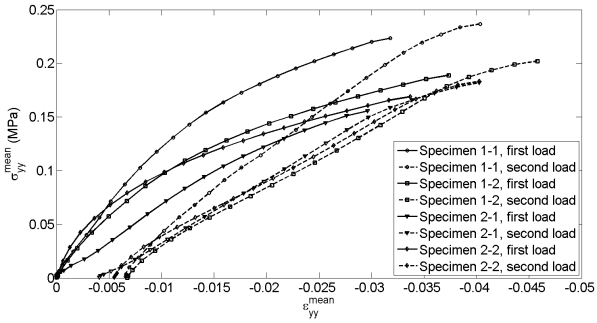

b- first and second loads

Figure 4 Global response under compression test

cannot really be compared because the contact between upper steel plate and specimen is probably not uniform despite the thin rubber strip placed between them. Beyond this first phase of the response, both specimens prepared with a 6.25% mass percent fraction of chitosan are stiffer than those prepared with a 4.15% mass percent fraction of chitosan. This result seems logical. It is confirmed by the apparent secant modulus deduced from the curves (over the [0-3]% interval, see Figure 4-a) which are reported in Table 1: they are greater for specimens prepared with a 6.25% mass percent fraction of chitosan. The second loadings

Specimen	1-1	1-2	2-1	2-2
E(MPa)	7.60	5.90	5.25	5.42

Table 1 Apparent secant modulus

presented in Figure 4-b show that the curves evolve first at a fairly linear rate, then reach the first curves after unloading and finally evolve in their continuity, which reveals a plastic response. The load was not increased further to reach failure (see Ref. [13] for information on the strength value), the goal here being mainly to characterize the mechanical response and to understand the phenomena that occur at the early stages of the tests, for strains smaller than a few percent.

4.2 Local response

he next step was to observe the underlying local mechanisms that occur as the load increases, and to establish the link between local and global responses. The full-field measurement technique described in Section 3.1 above was used for this purpose. Figures 5-a and -b show the relative vertical displacement field at maximum imposed displacement for specimens 1-1 and 2-1. These maps were obtained by subtracting at each

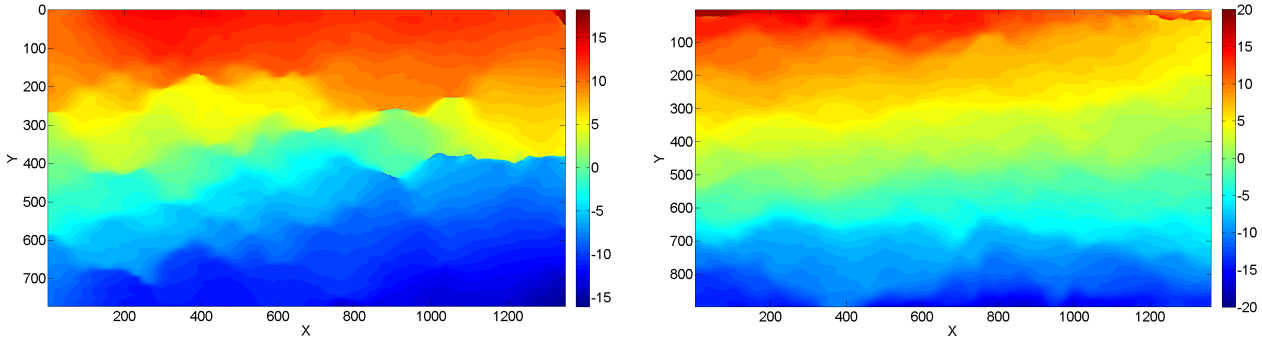

a- Specimen 1-1 b- Specimen 2-1

Figure 5 Displacement field at maximum load for Specimens 1-1 and 2-1

pixel the measured displacement and the mean value of the displacement field. All dimensions are given in pixels. Since 9 pixels are used to encode one grid pitch and since the pitch of the grid is equal to 0.8 mm, one pixel corresponds to 800/9≃89 micrometers on the surface of the specimen. It is quite logical to see that the displacement increases in both cases from the bottom to the top of the specimen, since a compression test is performed

(the moving grip is located at the top). On close inspection, however, it is worth noting that the displacement fields are irregular, especially for Specimen 1-1. This is due to very local displacement increases due to material heterogeneities. The corresponding strain fields ϵ_{yy} are shown in Figures 6-a and -b. It can be seen that the first strain distribution features very localized peaks, which are less concentrated for Specimen 2-1. Localized peaks

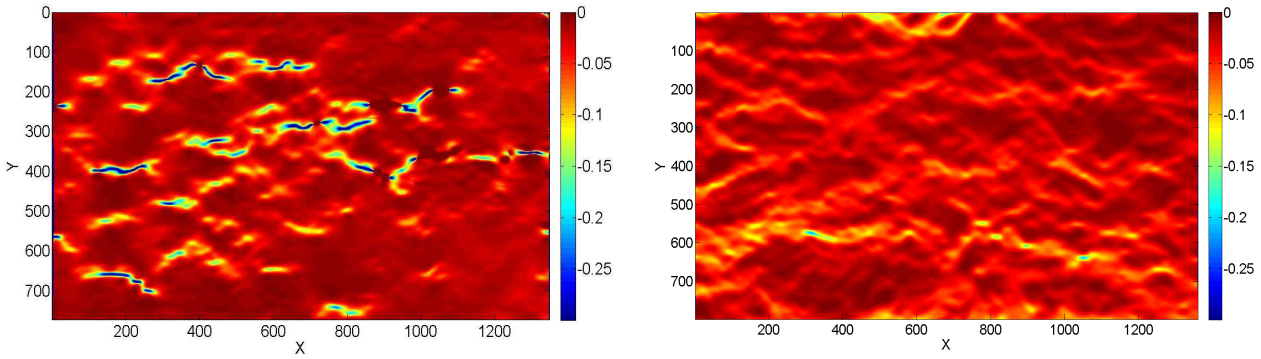

a- Specimen 1-1 b- Specimen 2-1

Figure 6 Strain field at maximum load for Specimens 1-1 and 2-1

correspond to situations for which sealant, and thus the grid, are pushed aside as voids collapse. This means that the strain values measured at these points are very high, but probably flawed because of the local out-of-plane movement of the sealant. Directly observing the grids enables us to perceive this phenomenon with the naked eye, see for instance Figure 7 where Specimen 1-1 after loading is represented: zones for which sealant has been pushed outside the voids are clearly visible.

The very different order of strain magnitude between different zones of the specimens

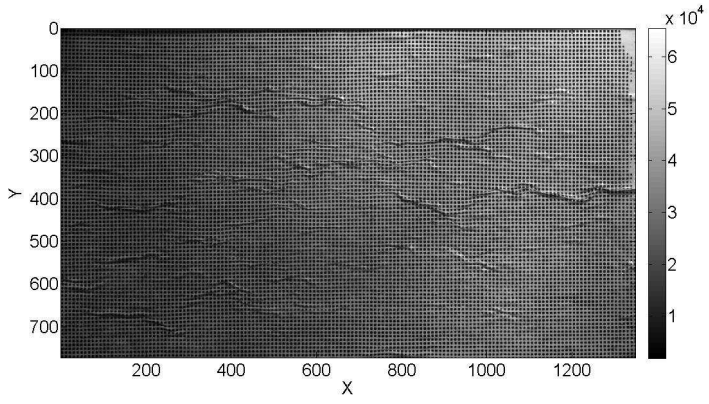

Figure 7 Deformed specimen. Specimen 1-1

tends to make the contrast in the zones for which the strain remains small not really visible. The same maps were plotted using a logarithmic scale to more clearly observe the difference in strain level in these zones. Results are shown in Figures 8-a and -b. It now becomes clearer that the strain distribution is heterogeneous in zones for which the strain level is small, even though it is blurred, as justified in Section 3.1 above.

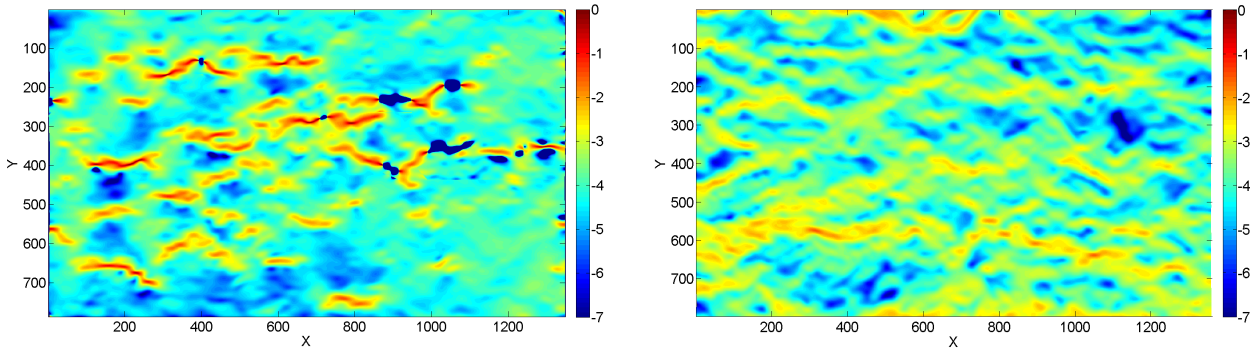

a- Specimen 1-1 b- Specimen 2-1

Figure 8 Strain field at maximum load for Specimens 1-1 and 2-1. Logarithmic scale.png

4.3 Comparison between local and global responses

It is interesting to compare the local strain value at any pixel, denoted ϵ_{yy}, and the mean strain ϵ_{yy}^{mean} already discussed above. This is done by calculating the ratio r_y, defined by

$$r_y = \frac{\epsilon_{yy}}{\epsilon_{yy}^{mean}} \tag{5}$$

between the two quantities. The corresponding maps are shown in Figure 9 with the same scale for both specimens.

Interestingly, this ratio is mainly lower than 1, but features very localized peaks which are much greater than 1 for Specimen 1-1. These peaks are obviously superposed on the strain peaks which are visible in Figure 6-a and -b above, since the maps are merely proportional between the two figures. The fact that the peaks are less pronounced for Specimen 2-1 means that the deformation mechanism is slightly different for each type of material: for the first type, deformation mainly occurs by void crushing, while bark and pith chips are more strained in proportion to the second type. This is probably due to the fact that, the amount of chitosan being smaller in the second case, impregnation of pith and bark chips is less efficient, thus leading to a lower stiffness, and thus to a greater strain level. Note that similar results are found for Specimens 1-2 and 2-2: strain peaks are more numerous

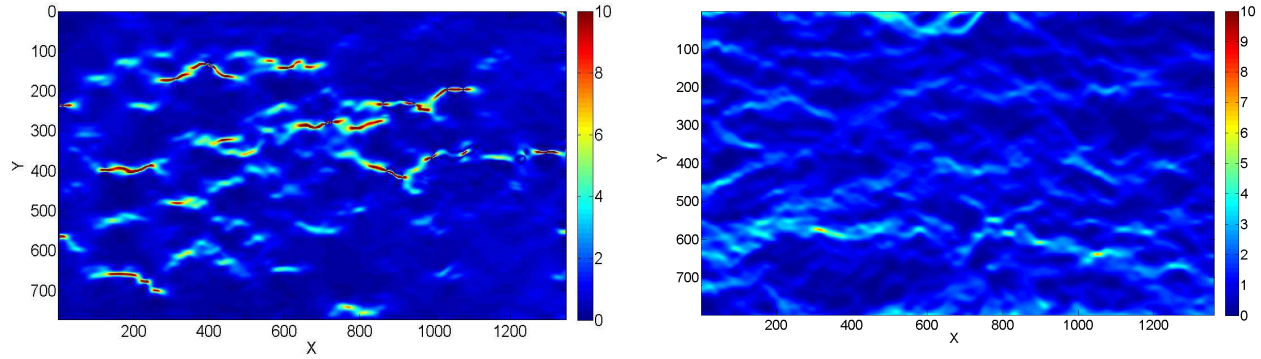

a- Specimen 1-1 b- Specimen 2-1

Figure 9 Normalization of the local strain by the mean strain

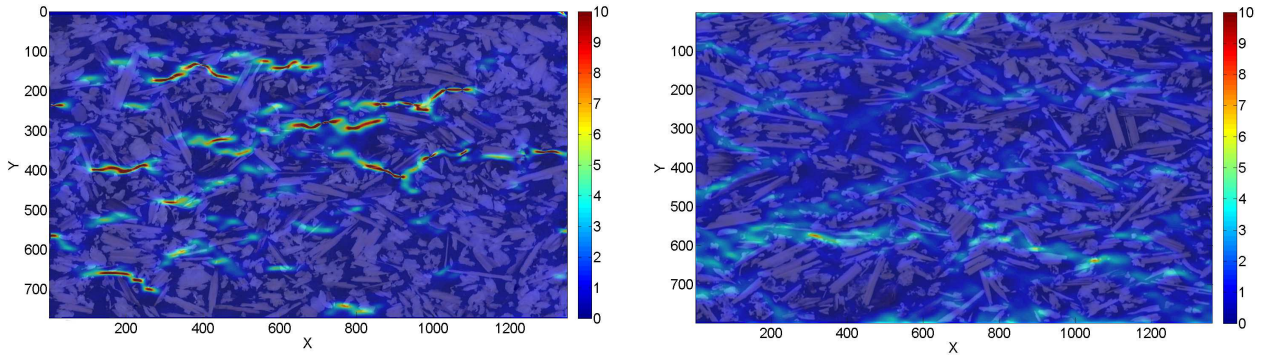

a- Specimen 1-1 c- Specimen 2-1

Figure 10 Superposition of the r_y map and the front face of the specimen

and more pronounced for Specimen 1-2 than for Specimen 2-2, and the obtained patterns for the corresponding maps are similar to those found for Specimens 1-1 and 2-1, respectively (corresponding maps not shown here).

Superposing now these maps and the front face of each specimen (see Figure 10) enables us to see that these strain peaks are actually mainly localized in the voids filled with sealant for both the specimens, as expected. This result can be quantified by using the 2D spatial correlation coefficient between the strain maps on the one hand, and the masks for pith, bark and sealant on the other hand [6]. Note that only pixels characterized by $abs(\epsilon_{yy}) > 0.07$ are kept in the strain map, this value being the threshold to detect sealant. This correlation, denoted R(strain,i), with i=sealant, bark and pith, is calculated with the corr2 function of Matlab. R(A,B) is equal to 1 when images A and B are identical and to -1 when they are

6. Details concerning the method of extraction the masks are presented in Annexe E

completely uncorrelated. The correlation numbers are reported in Table 2. It can be seen that R(strain,sealant) lies between 0.15 and 0.20 while R(strain,i), i=bark, pith, is negative and lies between -0.10 and -0.22, thus illustrating that high strain peaks are correlated with the present of voids, as expected.

The greatest part of the two r_y distributions exhibits a ratio r_y lower than 1. This is confirmed by the diagrams shown in Figure 11. They were obtained by collecting the r_y

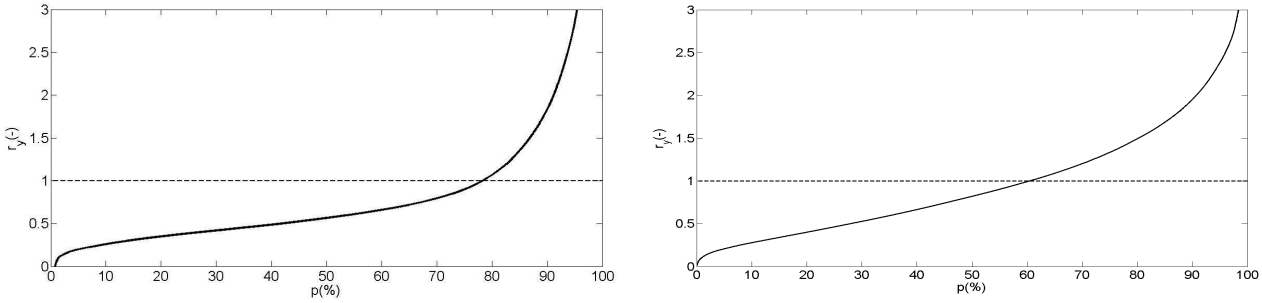

a- Specimen 1-1 b- Specimen 2-1

Figure 11 Sorted values for r_y

values for all the pixels, sorting them and plotting the resulting distributions. It can be seen that for Specimen 1-1 (Specimen 2-1, respectively), nearly 80 % (60 %, respectively) of the surface under investigation undergoes a strain lower that the mean strain sustained by the specimen, the remaining part sustaining a much greater strain level. This result tends to show that the deformation mechanism of Specimen 1-1 is dominated by void crushing, this phenomenon being less pronounced in Specimen 2-1, as already discussed above. It is worth mentioning that the spatial resolution of the measurement technique is not sufficient to detect very local strain peaks in bark, pith and mainly biomatrix. Such peaks are likely to take place around the voids because of this phenomenon. It can only be said that on average, the strain level in these constituents is lower than the mean strain, as illustrated by the blue zones (characterized by $r_y < 1$) in Figure 9.

Specimen	1-1	1-2	2-1	2-2
R(strain,sealant)	0.18	0.20	0.15	0.17
R(strain,bark)	-0.22	-0.24	-0.26	-0.19
R(strain,pith)	-0.12	-0.15	-0.11	-0.10

Table 2 Correlation coefficient between strain and sealant, bark and pith

4.4 Difference between the behavior of bark and pith

Another point is that the stiffness is very different from one constituent to another [11], so we can wonder whether the strain level sustained by theses phases is also different; in other words whether the strain distribution in the front face (apart from the sites of the voids) is heterogeneous and if heterogeneity is correlated to the nature of the constituents: bark and pith. This is not directly visible in Figure 8 despite the logarithmic scale used.

This question can be addressed by defining, for each specimen, three masks, corresponding to the zone covered by sealant, bark and pith, respectively. The first one is easily obtained by thresholding the gray levels in the images of the front face of the specimens. The color of the sealant being black and nearly uniform, the threshold value in terms of gray level is merely defined by a slightly greater value than the average gray level corresponding to this black color. The remaining part of the front face is then split into two additional masks: one for the pith and the other for the bark. Choosing the threshold value is trickier in this case, but a trial-and-error procedure led to a value which actually enables us to clearly distinguish these two phases. The Matlab software package [44] was used to determine the masks. The strain field in the pith and bark was then obtained by multiplying, pixel by pixel, each of the corresponding masks by the strain map. The mean value of each distribution was been calculated for each constituent. This procedure was applied to the whole set of images analyzed in this study. Note that some small zones, localized in the vicinity of the voids, exhibit a significant strain level. The points in these zones were therefore considered as outliers, and removed for this calculation. The threshold value to remove these points is -0.07, most of the points ranging between -0.07 and 0 (see histograms discussed below). Indeed it was considered that these small zones were affected by the high apparent strain measured in the sealant filling neighboring voids. The resulting strain maps for the bark and pith are shown in Figure 12 for Specimen 1-1 (similar results are obtained for the others, so they are not shown). No clear difference can be observed at this stage to the naked eye.

Considering now the mean strain over these zones (narrow horizontal pixel strips were removed at the top and bottom of each map to avoid edge effects) enables us to see a difference in behavior between the bark and the pith. This is illustrated in Figure 13 [7] where the mean strain in each constituent (bark and pith) is plotted *vs.* the number of the image for both specimens. It can be observed that the pith sustains a greater strain than the bark in both cases, and that this difference increases during the loading phase. This result seems logical, since pith is softer than bark. This is certainly also due to the very non-linear response of pith compared to bark, since the stress-strain curve of the former exhibits a significant plastic zone, as discussed in Ref [11].

7. The results for the other two specimens are presented in Annexe C

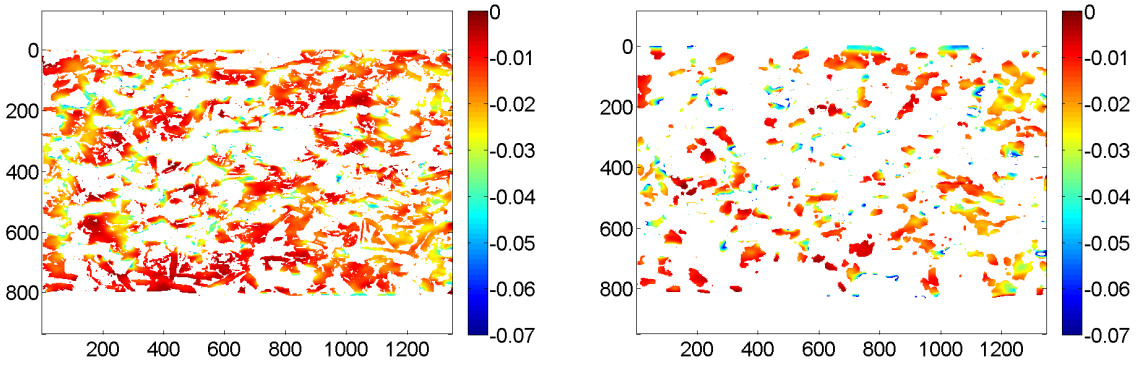

a- bark b- pith

Figure 12 Strain field in bark and pith at maximum load

This phenomenon is confirmed by plotting the histogram for ϵ_{yy} measured on the surface of each component for the highest load (image 22) (see Figure 14[8]). The number of points in each bin is lower for the pith than for the bark, because the pith spans a lower area than the bark. It can be seen to the naked eye that the pith histogram is slightly shifted to the left compared to that of the bark, thus illustrating that the absolute mean strain value in pith is greater than in bark. This trend is more visible by plotting the cumulative frequency in Figure 15: the curve for bark is shifted to the right for both specimens.

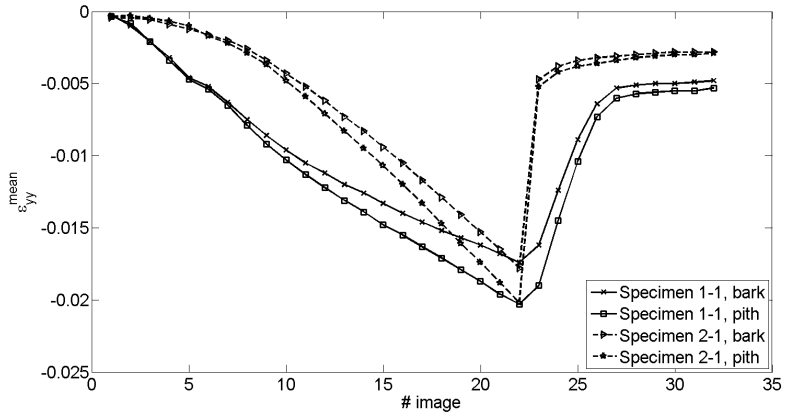

Figure 13 Mean strain in bark and pith vs. # image, Specimens 1-1 and 2-1

8. The results for the other two specimens are presented in Annexe C

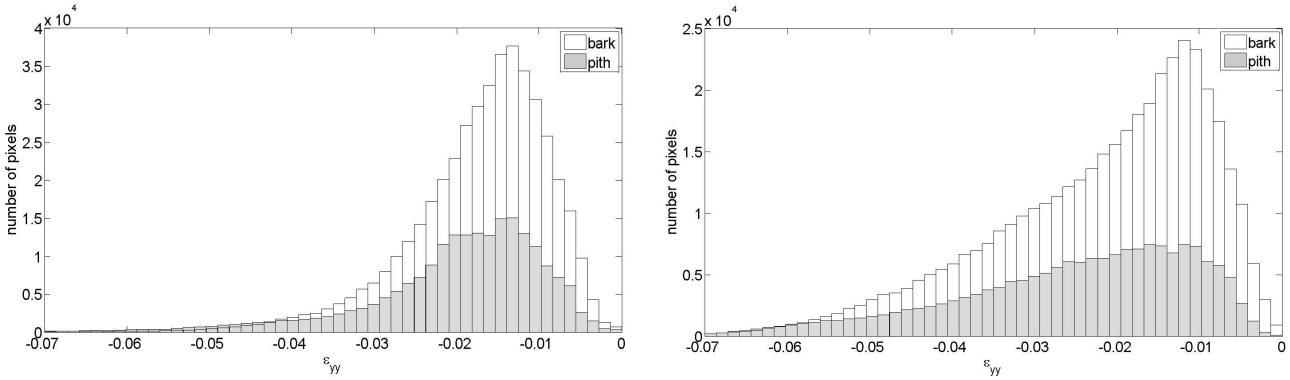

a- Specimen 1-1 b- Specimen 2-1

Figure 14 Histogram of the distribution of the strain in bark and pith at the maximum load

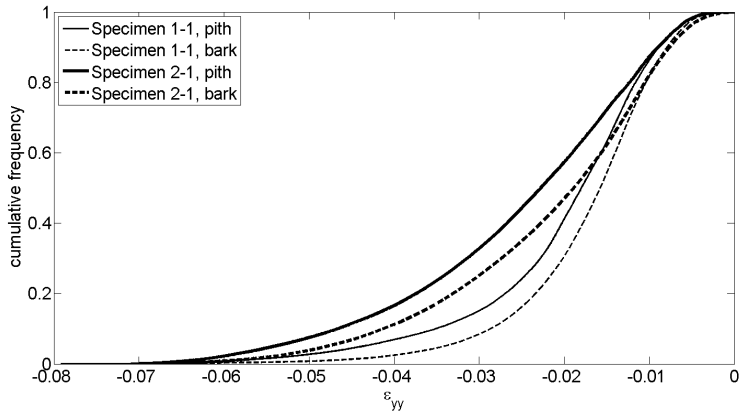

Figure 15 Cumulative frequency for the distribution of the strain in bark and pith at the maximum load. Specimens 1-1 and 2-2

5 Conclusion

The mechanical behavior of a sunflower/chitosan biocomposite was studied in this paper. Strain maps have two levels of heterogeneities. First, it was shown that the mechanical response was mainly governed by void crushing, which is equivalent to very high local strain. Second, it was shown that the strain level was greater in pith than in bark, which is due to the difference in stiffness between these two phases. The influence of the percentage of chitosan was also clearly observed.

Concerning the experimental technique used, namely the grid method, further work should be performed to investigate marking the surface under investigation with paint grids featuring a smaller pitch. Other tests should also be carried out to study other chitosan concentrations,

as well as the viscous response of this material.

Acknowlegdements

The authors acknowledge the French National Research Agency (ANR), Céréales Vallée, and ViaMéca for their financial support (ANR-10-ECOT-004 Grant).

Bibliography

[1] J. Witz, S. Roux, F. Hild, J. Reunier, Mechanical properties of crimped mineral wools: Identification from digital image correlation, Journal of Engineering Materials and Technology 130 (12) (2008) 1–7.

[2] F. Hild, E. Maire, S. Roux, J. Witz, Three-dimensional analysis of a compression test on stone wool, Acta Materialia 57 (12) (2009) 3310–3320.

[3] L. Roma, L. Martello, H. Savastano, Evaluation of mechanical, physical and thermal performance of cement-based tiles reinforced with vegetable fibers, Construction and Building Materials 22 (1) (2008) 668–674.

[4] O. Ortiz, F.Castells, G. Sonnemann, Sustainability in the construction industry: A review of recent developments based on LCA, Construction and Building Materials 23 (1) (2009) 28–39.

[5] A. Korjenic, V. Petranek, J. Zach, J. Hroudova, Development and performance evaluation of natural thermal-insulation materials composed of renewable resources, Energy and Buildings 43 (2011) 2518–2523.

[6] N. Hajj, R. Dheilly, Z. Aboura, M. Benzeggagh, M. Queneudec, Development of thermal insulating and sound absorbing agro-sourced materials from auto linked flax-tows, Industrial Crops and Products 34 (2011) 921–928.

[7] S. Panyakaew, S. Fotios, New thermal insulation boards made from coconut husk and bagasse, Energy and Buildings 43 (2011) 1732–1739.

[8] M. Bentchikou, A. Guidoum, K. Scrivener, K. Silhadi, S. Hanini, Effect of recycled cellulose fibres on the properties of lightweight cement composite matrix, Construction and Building Materials 34 (1) (2012) 451–456.

[9] M. Chikhi, B. Agoudjil, A. Boudenne, A. Gherabli, Experimental investigation of new biocomposite with low cost for thermal insulation, Energy and Buildings 66 (1) (2013) 267–273.

[10] S. Benfratello, C. Capitano, G. Peri, G. Rizzo, G. Scaccianoce, G. Sorrentino, Thermal and structural properties of a hemp-lime biocomposite, Construction and Building Materials 48 (2013) 745–754.

[11] S. Sun, J.-D. Mathias, E. Toussaint, M. Grédiac, Hygromechanical characterization of sunfower stems, Industrial Crops and Products 46 (2013) 50–59.

[12] S. Sun, J.-D. Mathias, E. Toussaint, M. Grédiac, Characterizing the variance of mechanical properties of sunflower bark for biocomposite applications, Bioresources 9 (1) (2014) 922–937.

[13] N. Mati-Baouche, H. D. Baynast, S. Sun, A. Lebert, C. J. S. Lopez-Mingo, P. Leclaire, P. Michaud, Mechanical, thermal and acoustical characterizations of a insulating bio-based composite made from sunflower stalks particles and chitosan, Industrial Crops and Products, accepted.

[14] D. 4108-10, Anwendungsbezogene Anforderungen an Wärmedämmstoffe - Werkmäßig hergestellte Wärmedämmstoffe, Ausgabe 2008-06 (2008).

[15] J. Piro, M. Grédiac, Producing and transferring low-spatial-frequency grids for measuring displacement fields with moiré and grid methods, Experimental Techniques 28 (4) (2004) 23–26, society for Experimental Mechanics.

[16] A. K. Patel, P. Michaud, H. de Baynast, M. Grédiac, J.-D. Mathias, Preparation of chitosan-based adhesives and assessment of their mechanical properties, Journal of Applied Polymer ScienceWiley. DOI: 10.1002/app.37685.

[17] A. K. Patel, P. Michaud, E. Petit, H. de Baynast, M. Grédiac, J.-D. Mathias, Development of a chitosan-based adhesive, Application to wood bonding, Journal of Applied Polymer ScienceWiley. DOI: 10.1002/app.38097.

[18] A. K. Patel, H. de Baynast, J. Mathias, M. Grédiac, P. Michaud, Adhesive Composition Including deacetylated Chitosan, 2013, united States Patent Application 20130143041.

[19] A. Semerci, Y. Kaya, The components of production cost in sunflower and its relationships with input prices, in: International Conference on Applied Economic - ICOAE 2009, 2009, pp. 593–599.

[20] Z. Yan, H. Wang, K. Lau, S. Pather, J. Zhang, G. Lin, Y. Ding, Reinforcement of polypropylene with hemp fibres, Composites Part B: Engineering 46 (2013) 221–226.

[21] J. Andersons, R. Joffe, Estimation of the tensile strength of an oriented flax fiber-reinforced polymer composite, Composites Part A: Applied Science and Manufacturing 42 (9) (2009) 1229–1235.

[22] M. Hautala, A. Pasila, J. Pirila, Use of hemp and flax in composite manufacture: a search for new production methods, Composites Part A: Applied Science and Manufacturing 35 (1) (2004) 11–16.

[23] J.-D. Mathias, A. Alzina, Grédiac, P. Michaud, P. Roux, H. D. Baynast, C. Delattre, N. Dumoulin, T. Faure, P. Larrey-Lassalle, N. Mati-Baouche, F. Pennec, S. Sun, N. Tessier-Doyen, E. Toussaint, W. Wei, Valorising sunflower stems as natural fibres for biocomposite applications: an environmental and socio-economic opportunity Submitted.

[24] N. Mati-Baouche, H. D. Baynast, C. Vial, F. Audonnet, S. Sun, E. Petit, F. Pennec, V. Prevot, P. Michaud, Physico-chemical, thermal and mechanical characterizations of solubilized and solid state chitosans Submitted.

[25] L. Q. Wu, H. Eembree, B. Balgley, P. Smith, G. Payne, Utilizing renewable resources to create functional polymers: chitosan-based associative thickener, Environmental Science and Technology 36 (2002) 3446–3454.

[26] Salome: the Open Source Integration Plateform for Numerical Simulation, http://www.salome-platform.org/, last accessed mar, (2014).

[27] Aster Code for Windows, http://sourceforge.net/projects/asterwin/, last accessed mar, (2014).

[28] F. Pennec, A. Alzina, N. Tessier-Doyen, B. Nait-Ali, N. Mati-Baouche, H. D. Baynast, D. Smith, A combined finite-discrete element method for calculating the effective thermal conductivity of bio-aggregates based materials, International Journal of Heat and Mass Transfer 60 (2013) 274–283.

[29] A. Abdou, I. Boudaiwi, The variation of thermal conductivity of fibrous insulation materials under different levels of moisture content, Construction and Building Materials 43 (2013) 533–544.

[30] M. A. Sutton and J. J. Orteu and H. W. Schreier, Image correlation for shape, motion and deformation measurements, Springer, 10 (2009) 978–0.

[31] A. Chrysochoos and Y. Surrel, Chapter 1. Basics of metrology and introduction to techniques, in M. Grédiac and F. Hild, editors, Full-field measurements and identification in Solid Mechanics, John Wiley & Sons, (2012).

[32] Y. Surrel, Moiré and grid methods in optics: a signal-processing approach, in: Proceedings of the SPIE, Vol. 2342, 1994, pp. 213–220.

[33] Y. Surrel, Photomechanics, Topics in Applied Physic 77, Springer, 2000, Ch. Fringe Analysis, pp. 55–102.

[34] C. Badulescu, M. Grédiac, J.-D. Mathias, D. Roux, A procedure for accurate one-dimensional strain measurement using the grid method, Experimental Mechanics 49 (6) (2009) 841–854.

[35] C. Badulescu, M. Grédiac, J.-D. Mathias, Investigation of the grid method for accurate in-plane strain measurement, Measurement Science and Technology 20 (9) (2009) 20:095102.

[36] F. Sur, M. Grédiac, Towards deconvolution to enhance the grid method for in-plane strain measurement, Inverse Problems and ImagingAmerican Institute of Mathematical Sciences. In press.

[37] M. Grédiac, F. Sur, C. Badulescu, J.-D. Mathias, Using deconvolution to improve the metrological performance of the grid method, Optics and Lasers in Engineering 51 (2013) 716–734, elsevier.

[38] S. K. S. X. J. Notbohm, A. Rosakis, G. Ravichandran, Three-dimensional displacement and shape measurement with a diffraction assisted grid method, Strain 49 (5), dOI: 10.1111/str.12046.

[39] A. V. S. Avril, Y. Surrel, Grid method: application to the characterization of cracks, Experimental Mechanics 44 (1) (2004) 37–43.

[40] M. R. W. J.-H. Kim, F. Pierron, S. Avril, Local stiffness reduction in impacted composite plates from full-field measurements, Composites Part A: Applied Science and Manufacturing 40 (12) (2009) 1961–1974.

[41] K. N. S. Ri, M. Saka, D. Kobayashi, Dynamic thermal deformation measurement of large-scale, high-temperature piping in thermal power plants utilizing the sampling moiré method and grating magnets, Experimental Mechanics 53 (9) (2013) 1635–1646.

[42] Sikaflex®-11 FC+ data sheet, #525 (2011).

[43] C. Chiang, Statistical methods of analysis, World Scientific Pub Co Inc., 2003.

[44] Matlab 2009 b. the Language of Technical Computing, http://www.mathworks.com/products/matlab/, last accessed mar, (2014).

Chapitre 4

Homogenizing mechanical properties of sunflower bark specimen

Article en cours de finalisation.

Introduction au chapitre 4

Les chapitres 1 et 3 ont montré que l'écorce joue un rôle important dans le comportement mécanique du biocomposite. Nous avons donc décidé d'étudier le comportement mécanique de l'écorce par une approche statistique au chapitre 2. Le chapitre 4 a pour but de développer une approche d'homogénéisation multi-échelles afin de prendre en compte les propriétés mécaniques des constituants microscopiques dans le comportement mécaniques macroscopique de l'écorce. Cette approche est basée sur trois modèles d'homogénéisation : la loi des mélanges, le modèle de porosité sphéroïdale et le modèle de porosité cylindrique. Le modèle de porosité sphéroïdale et le modèle de porosité cylindrique sont utilisés pour tenir compte de la forme des cellules à l'échelle microscopique afin d'obtenir les propriétés mécaniques des trois principaux tissus qui composent l'écorce (tissus de parenchyme, de sclérenchyme et de xylème). Les propriétés mécaniques de l'écorce sont ensuite obtenus avec la loi des mélanges appliquée à ces trois tissus. Ces modèles nécessitent des paramètres qui sont soit identifiés expérimentalement à travers des analyses d'images soit à partir de données issues de la littérature. Les résultats ainsi obtenus sont ainsi discutés que ce soit au niveau des tissus ou au niveau de l'écorce.

Homogenizing mechanical properties of sunflower bark specimen

Shengnan SUN[1], Jean-Denis MATHIAS[2†], Evelyne TOUSSAINT[1]and Michel GREDIAC[1]
[1] *Clermont Université, Université Blaise Pascal, Institut Pascal, UMR CNRS 6602*
BP 10448, 63000 Clermont-Ferrand, France
[2] *IRSTEA, Laboratoire d'Ingénierie pour les Systèmes Complexes*
9 Avenue Blaise Pascal, CS20085, 63178 Aubière, France
† *corresponding author. Tel.: +33 473440600; fax:+33 473440696, jean-denis.mathias@irstea.fr*

Abstract

Sunflower bark is a natural fibre made of different tissues which are porous at the cell scale. The tissues' content and porosity change with respect to their location along the stem. This leads to a variation in the effective stiffness of sunflower bark. We develop here a homogenization model that combines the mixture rule, the spheroidal porosity model and the cylindrical porosity model in order to estimate the effective stiffness of sunflower bark. The homogenization parameters are collected from both experimental measurements and literature references. Theoretical and experimental results are in good agreement for specimens extracted at both the bottom and the top of sunflower stems.

Keywords: Sunflower bark, Cell morphology, Homogenization methods, Mechanical testing

1 Introduction

The world is facing major environmental and socio-economic challenges today. A main challenge lies in the transition from a dependence on fossil fuels to a situation where biomass will provide a sustainable supply of renewable raw materials for industry. One solution lies in the use of natural fibres which are expected to harm the environment less than synthetic fibres such as carbon fibres for example. During the last decade, biocomposites reinforced by plant fibres such as wood, ax, hemp, jute and sisal have rapidly developed for various industrial applications, especially for the construction and automotive industries. In view of the rapid expansion of natural fibre-based composites, new composites reinforced with agriculture by-product fibres offer a potentially effective way to ease the disparities in natural fibre supply and demand. Some studies on the use of agricultural by-products as composite reinforcement

have been reported in the literature [1–7]. These by-products are corn stalk, wheat, rice or corn straw. These studies clearly show that such byproducts offer a relevant solution for some composite applications. We focus here on a promising agricultural by-product: sunflower stems.

Sunflower is widely cultivated for the edible oil extracted from its grains (world harvested area: 24.84E+06 ha [8]). The sunflower itself is clearly the most useful part of the plant. To the best of the authors' knowledge, there is no significant industrial use of the stems, which are shredded after sunflower harvesting. Sunflower stems are composed of two parts: pith and bark. A previous study has shown the hygro-mechanical properties of both the pith and the bark [9, 10]. The main result of this study was to show that the stiffness of sunflower bark changes depending on the specimen extraction location because of the morphological and porosity variations in the sunflower bark along the stems.

We propose here to determine the macroscopic properties of bark according to several microscopic properties. The dried sunflower bark is mainly composed of tissues of parenchyma, xylem, sclerenchyma and phloem: their cells are longitudinally arranged along the stem. The xylem, parenchyma and sclerenchyma are lignified yielding an increase in the stiffness of the bark. The latter can be considered as a unidirectional composite made of these longitudinally arranged tissues. These tissues exhibit varying stiffness and volume ratios in the bark. Moreover, these properties also vary along the stem.

To evaluate the stiffness of sunflower bark, a suitable homogenization model based on the knowledge of the tissue properties is developed. Three models are combined for this purpose. The first is the mixture rule. The second and third are respectively the spheroidal porosity model and the cylindrical porosity model. Homogenization parameters are obtained either from the literature or from experimental data using image analysis. This procedure yields an assessment of the effective stiffness of sunflower bark. Homogenized results are then successfully compared to experimental results, showing the relevancy of the proposed approach.

2 Statement of the problem

As explained above, the sunflower stem (macroscopic scale) is divided into pith and bark (scale order: 10^{-2}m, see Figure 1). The bark is composed of various tissues (mesoscopic scale). Tissue is a cellular organizational level intermediate between cells (microscopic scale) and bark, and composed by a set of cells. Three different scales are involved here:

- macroscopic scale: this is the scale of the stem;
- mesoscopic scale: this is the scale of the tissues;

– microscopic scale: this is the scale of the cells.

The spatial arrangement of these tissues enables us to consider the bark as a unidirectional composite at the tissue scale. From this point of view, the longitudinal stiffness of the bark can be determined with the longitudinal stiffness of each tissue using the mixture rule. It can be observed that the primary components of sunflower bark (scale order: 10^{-4}m, see Figure 1) are:

– parenchyma: parenchyma tissues are present within many plants and they can also be found in wood. Parenchyma tissues participate in different biological functions such as regeneration, wound healing and solute movements in the plant. Parenchyma tissues can clearly be distinguished in Figure 1 at the mesoscopic scale;
– xylem: the function of this tissue is to transport water. It contributes to the rigidity of bark. It is a complex tissue composed of xylem vessels, xylem tracheids and xylem parenchyma. Xylem vessel elements are open pipes which are connected to each other and form a continuous tubular vessel. These cells possess greater diameters than xylem tracheids and xylem parenchyma. Xylem parenchyma exhibit properties similar to those of parenchyma tissue. Xylem tracheids are closed pipes like xylem parenchyma but they are more elongated;
– sclerenchyma: this is mainly composed of dead cells that have been strongly lignified. Sclerenchyma is contained in the vascular bundle and is arranged in long strands.
– other tissues such as phloem and collenchyma are present in the bark. Phloem is located between the sclerenchyma and xylem tissues (see Figure 1-(a)(b)). The cells walls are not lignified and are easily breakable. Collenchyma are present in the cortex of bark, their amount is small compared to other tissues. The mechanical contribution of these tissues to the bark stiffness is negligible and they are neglected in the following.

The three previous tissues (xylem, parenchyma and sclerenchyma) contribute to the macroscopic stiffness of the bark. Performing homogenization therefore requires us first to determine the mechanical properties of these tissues before employing them to feed relevant models. Tissues are analyzed at the cellular scale for this purpose. At this scale, they can be considered as porous media (scale order: 10^{-6}m, see Figure 1 at the microscopic scale). In the following, a homogenization procedure is elaborated and takes into account the morphological and mechanical properties of the components at the different scales.

3 Homogenization method

As explained above, we use here a homogenization procedure based on three homogenization models: the spheroidal porosity model, the cylindrical porosity model and

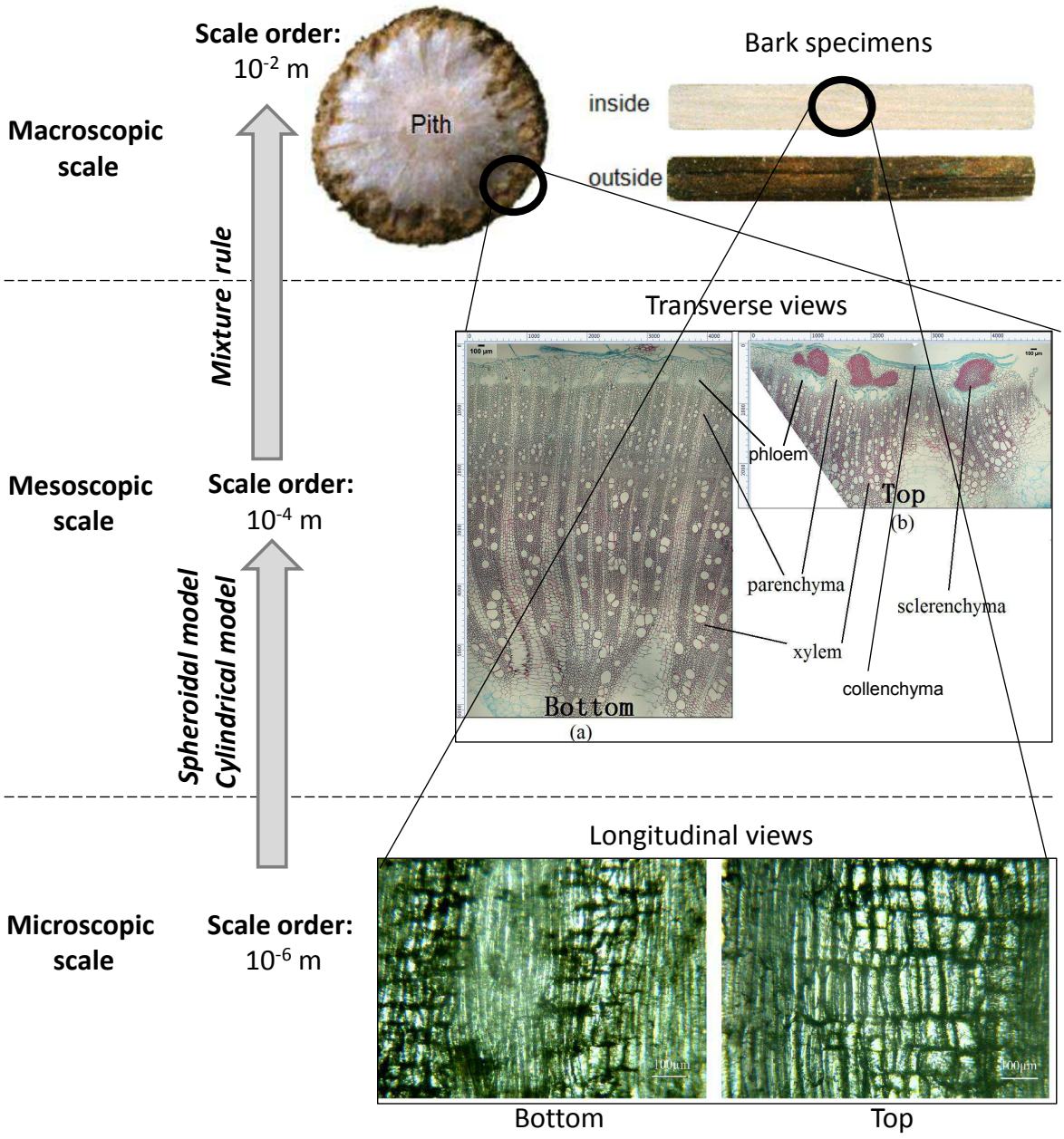

Figure 1 Multiscale approach for determining bark's properties: bark is made of three tissues (scale order: 10^{-4}m) whose properties depend on their pore shape (scale order: 10^{-6}m).

the mixture rule.

3.1 Homogenization models

3.1.1 The spheroidal porosity and cylindrical porosity models

The elongated shape of the cells at the microscopic scale (see Figure 1) leads the cell shape to be modelled by an ellipsoid. The Young's modulus is determined using Boccaccini's equation [11] modified from the work of Ondracek and Gerhard [12]. This equation enables us to take into account the influence of porosity and cell shape on the Young's modulus. The Young's modulus E_i of a tissue i is written:

$$\begin{cases} E_i = E_i^0\big(1 - P_i^{\frac{2}{3}}\big)^{s_i} \\ \\ s_i = 1.21\big(\frac{z_i}{x_i}\big)^{\frac{1}{3}}\left[1 + \big[\big(\frac{z_i}{x_i}\big)^{-2} - 1\big]cos^2\phi_i\right]^{\frac{1}{2}} \end{cases} \tag{1}$$

where P_i is the porosity of the porous media i. E_i is the homogenized Young's modulus and E_i^0 is the cell wall stiffness. $\frac{z_i}{x_i}$ is the mean axial ratio (shape factor) of the spheroidal pores. ϕ_i is the angle between the rotational axis of the spheroids and the stress direction. Cell lumens are orientated along the stem, ϕ_i is equal to zero in this case. This leads to:

$$s_i = 1.21\big(\frac{z_i}{x_i}\big)^{-\frac{2}{3}} \tag{2}$$

Equation 1 will be used for the calculation of homogenized Young's modulus of both the parenchyma and sclerenchyma tissues.

For long cylindrical pores ($\frac{z_i}{x_i} \rightarrow \infty$) orientated along the principal stress direction, Equation 1 cannot be applied. In this case, we use a cylindrical porosity model [13–16]:

$$E_i = E_i^0\big(1 - P_i\big) \tag{3}$$

This equation will be used for the calculation of the homogenized Young's modulus of xylem vessels.

3.1.2 Mixture rule

The mixture rule will be used in order to determine the effective stiffness of both the xylem tissue and the bark. It is written as follows:

$$E_{eff} = \sum_i E_i V_i \tag{4}$$

where E_{eff} is the effective Young's modulus, E_i and V_i are the Young's modulus and the

volume ratio of each component, respectively.

3.2 Homogenizing the Young's modulus of tissues and bark

The effective Young's modulus of each bark tissue is first calculated to subsequently assess the Young's modulus of the bark. The effective value of the Young's modulus E_p of the parenchyma tissue is calculated using Equation 5. Thus:

$$\begin{cases} E_p = E_p^0\big(1 - P_p^{\frac{2}{3}}\big)^{s_p} \\ s_p = 1.21\big(\frac{z_p}{x_p}\big)^{-\frac{2}{3}} \end{cases} \tag{5}$$

In the same way, the effective value of the Young's modulus E_s of the sclerenchyma tissue is :

$$\begin{cases} E_s = E_s^0\big(1 - P_s^{\frac{2}{3}}\big)^{s_s} \\ s_s = 1.21\big(\frac{z_s}{x_s}\big)^{-\frac{2}{3}} \end{cases} \tag{6}$$

The effective modulus E_x of the xylem tissue depends on the properties of three kinds of cells: the xylem vessel, the xylem tracheid and the xylem parenchyma. The Young's modulus of the xylem tracheid and the xylem parenchyma (respectively denoted E_{xt} and E_{xp}) are calculated using the spheroidal porosity model. Consequently:

$$\begin{cases} E_{xp} = E_{xp}^0\big(1 - P_{xp}^{\frac{2}{3}}\big)^{s_{xp}} \\ s_{xp} = 1.21\big(\frac{z_{xp}}{x_{xp}}\big)^{-\frac{2}{3}} \end{cases} \tag{7}$$

$$\begin{cases} E_{xt} = E_{xt}^0\big(1 - P_{xt}^{\frac{2}{3}}\big)^{s_{xt}} \\ s_{xt} = 1.21\big(\frac{z_{xt}}{x_{xt}}\big)^{-\frac{2}{3}} \end{cases} \tag{8}$$

As explained above, the lumen of a xylem vessel is considered as a long cylindrical pore. In this case, the Young's modulus E_{xv} of the xylem vessel is calculated using Equation 3. Thus:

$$E_{xv} = E_{xv}^0\big(1 - P_{xv}\big) \tag{9}$$

Then, the equivalent Young's modulus E_x of the xylem tissue is determined using the mixture rule:

$$E_x = E_{xv}V_{xv} + E_{xt}V_{xt} + E_{xp}V_{xp} \tag{10}$$

where V_{xv}, V_{xt} and V_{xp} are the volume ratios of the different components of the xylem tissue. Finally, the effective stiffness of the bark is deduced once again using the mixture rule from

tissue values:

$$E_{eff} = E_x V_x + E_p V_p + E_s V_s \tag{11}$$

3.3 Setting the model parameters

The volume ratio V_i , the cell porosity P_i and the shape factor $\frac{z_i}{x_i}$ of tissues were determined either by processing images with ImageJ software (ImageJ, 2012) or from the literature. Indeed, due to the diffculties in obtaining micrographs of sclerenchyma tissue and xylem tracheids, the shape factors $\frac{z_s}{x_s}$ and $\frac{z_{xt}}{x_{xt}}$ were obtained from the literature [17–19]. Note also that sclerenchyma fibres are only visible at the top location of the stem (see Figure 2). Consequently only parenchyma and xylem tissues are taken into consideration for the calculation of the effective Young's modulus of the bark at the bottom location.

Figure 2 shows representative zones used for analyzing the tissue distribution in the bark. From this figure, the cell porosity P_i, the volume ratio V_i and the shape factor $\frac{z_i}{x_i}$ of all tissues are determined as follows:

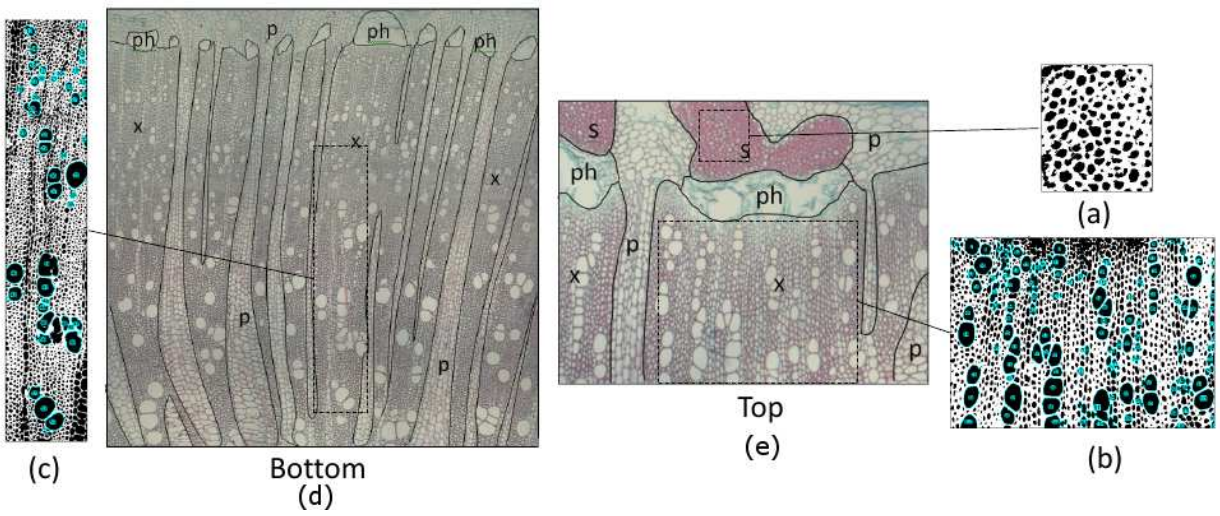

Figure 2 Typical example for determining tissues content. p: parenchyma tissue, s: sclerenchyma tissue, x, xylem tissue, ph: phloem tissue. (a) binarized sclerenchyma; (b) (c) binarized xylem tissue.

– cell porosity P_i: Figure 2-(a) presents an example of binarized sclerenchyma tissue. From this figure, the ratio between the black and white zones is calculated using ImageJ Software, enabling the determination of the porosity of the sclerenchyma tissue P_s. The same procedure is used to determine the porosities of the parenchyma P_p, xylem vessel P_{xv}, xylem tracheid P_{xt} and xylem parenchyma P_{xp};

- volume ratio V_i: the volume ratio of each tissue of sclerenchyma (V_s), parenchyma (V_p) and xylem (V_x) is determined either using ImageJ sofware from Figure 2-(d)(e) or from the literature. In the case of xylem tracheids and xylem parenchyma, we cannot determined their volume ratio because both tissues exhibit the same range of diameters. Therefore, we use literature data [19, 20] to determine V_{xt} and V_{xp};
- shape factor $\frac{z_i}{x_i}$: because of the diffculty in obtaining micrograph along the longitudinal direction, the shape factor is only determined for parenchyma. In that case, about thirty $\frac{z_{xp}}{x_{xp}}$ rratios were calculated by manually measuring both the length and the width of various cells (see Figure 3). Due to the lack of information concerning the biological characteristics of sunflowers stems, other plants were chosen to provide approximations of the shape factors of other cells. For instance, arecaceae [17] and podocarpus lambertii [18] were used to determine the shape factor of sclerenchyma and xylem tracheid, respectively.

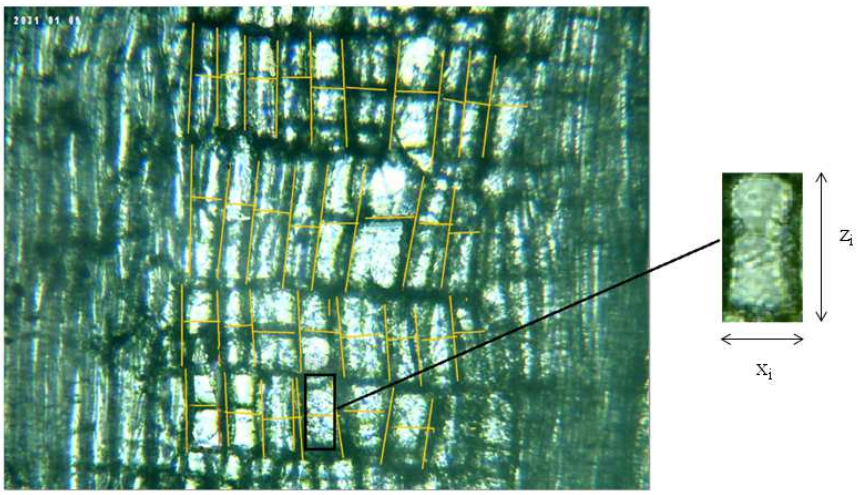

Figure 3 Example for the determination of shape factor $\frac{z_i}{x_i}$.

The cell wall stiffness E_i^0 of each tissue was determined from bamboo and wood data (see [21] for parenchyma and sclerenchyma and [22] for xylem vessels and xylem tracheids). ImageJ analysis results and literature data are presented in Table 1. Note that phloem values are not reported in this table because these values are negligible for the calculation of the stiffness of the bark as explained above.

	Parenchyma (bottom / top)	Sclerenchyma (bottom / top)	Xylem (bottom / top)		
			X_v	X_t	X_p
E_i^0 (GPa)	5.8 [b]	16.01 [b]	14.28 [c]	14.28 [c]	5.8 [b]
P_i (%)	67 / 69 [a]	-/ 33 [a]	72/ 70 [a]	48 / 49 [a]	48 / 49 [a]
z_i/x_i (-)	3.47 / 3.20 [a]	- / 6.8 [d]	-	70 / 70 [e,f]	3.47 / 3.20 [a]
V_i(%)	36 / 15 [a]	- / 13 [a]	19 / 25 [a]	23 / 23 [f,g]	14 / 16 [f,g]

Table 1 Experimental values of the three tissues. a: values from ImageJ analysis; b: Value from bamboo [21]; c: value deduced with the linear density-Young's modulus relationship of wood cell wall described in [22]. Note that the density of the xylem cell wall is approximately equal to $\frac{density\ of\ bark}{1-P_{xylem}} = \frac{0.30}{1-0.51}$=0.61g/cm^3, then $E_t^0, E_v^0 = 23.33 \times 0.61 = 14.28\ GPa$, where 23.33 is the slope of the linear relationship mentioned above; d: value from Arecaceae [17] e: value from Podocarpus lambertii [18]; f: value from Cinnamosma madagascariensis [19], g: value from AngiospermWood [20].

4 Results

4.1 Tensile tests

The sunflower species used for this study was LG5474, grown in Perrier, France, in 2010. Specimens were extracted from portions of stems of length 765 mm. For all the stems from which specimens were cut, the bottom section was chosen at the level of the first node above the roots. Specimens were extracted from the two extremities of each portion of stem (see Figure 4). The short portions of stems extracted from the two extremities were divided lengthwise into six parts. The inner face of each part was lightly polished with sandpaper to obtain nearly plane specimens and to remove pith residues.

The experimental results for the Young's modulus were determined by performing tensile tests using a Deben MICROTEST testing machine equipped with a 2-kN load cell (see Figure 5). The cross-head speed was equal to 2 mm/min. The specimen clamping length was 30 mm. The mechanical tests were carried out at room temperature. The specimens were stabilized in a 33% relative humidity environment beforehand. Ten specimens were tested for both locations. The Young's modulus was estimated from the experimental curves obtained during these tests (see Figure 5). The Young's modulus of sunflower bark conditioned at 33% relative humidity is equal to 4.73±0.63 GPa at the bottom location and 6.76 ±0.43 GPa at the top location.

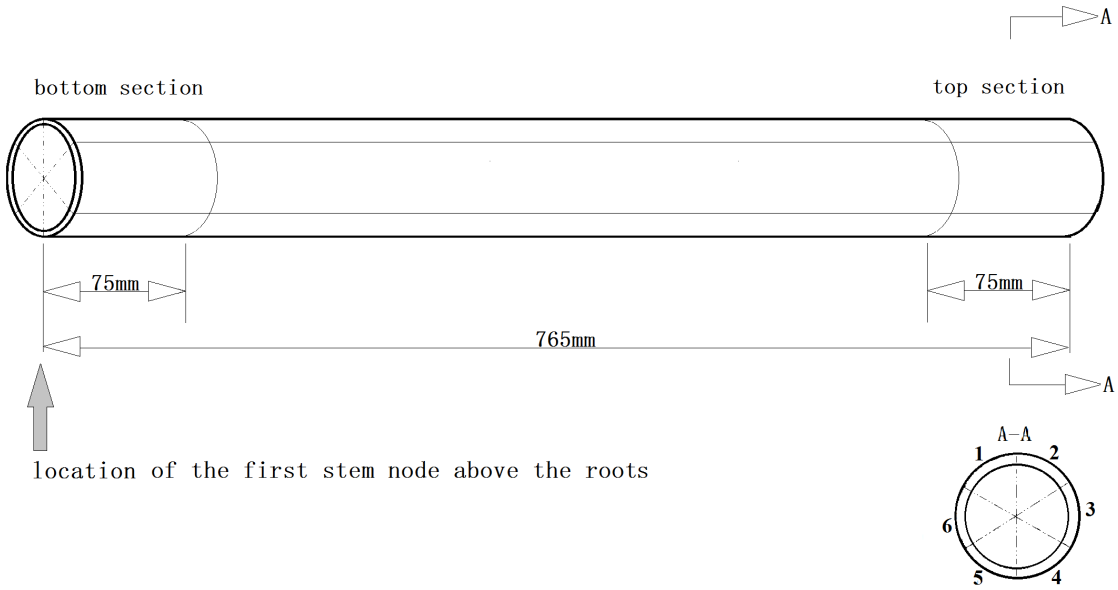

Figure 4 Specimen locations.

4.2 Tissue homogenization

The Young's modulus of each homogenized tissue are presented in Table 2. The difference in Young's modulus value of each tissue between bottom and top locations is mainly due to the difference of porosity (see Table 1).

	Parenchyma (bottom / top)	Sclerenchyma (bottom / top)	Xylem (bottom / top)
E_i (GPa)	2.68 / 2.63	- / 12.84	7.71 / 7.31

Table 2 Young's modulus of homogenized tissues.

These results are now compared with values available in the literature. The xylem tissue from tobacco plants [23] lies between 2.8 and 3.7 GPa, depending on the relative humidity (30% and 60% according to [23], respectively). These values are lower than the homogenized results (7.71/7.31 GPa) obtained in the present study. However, in the work of Niklas and Karl [24], the experimental Young's modulus of wood tissue (mainly composed of xylem tissue) was between 5 and 30 GPa which is in agreement with our result concerning xylem tissue.

In the same work [24], the Young's modulus of the parenchyma tissue of potatoes and apples ranges between 0.8 and 10 MPa, which is significantly smaller than the present homogenized results (2.68/2.63 GPa). This difference is mainly due to the fact that

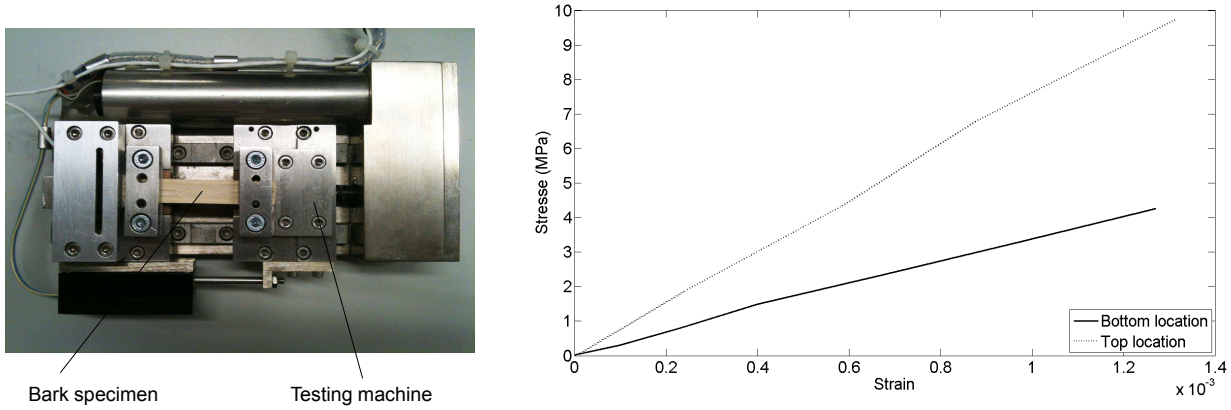

(a) Tensile testing machine

(b) Typical Stress-Strain curves for bark specimens

Figure 5 Experimental tensile tests.

potatoes and apples exhibit parenchyma cells which are not lignified (the cell walls are therefore softer).

Finally, concerning the Young's modulus of sclerenchyma, Niklas and Karl [24] studied psilotum and elderberry stem. The obtained values range between 1 and 4 GPa. Niklas [25] also studied the bast fibre (composed of sclerenchyma) and obtained a Young's modulus of 35 GPa. The present homogenized result (12.84 GPa) is in the same range as these available data.

4.3 Bark homogenization

The homogenized Young's modulus of sunflower bark is calculated using Equations 1, 3 and 4. The homogenization method gives a stiffness value equal to 5.31 GPa for the bark at the bottom and 6.82 GPa at the top of the stem. The experimental results for the Young's modulus of sunflower bark are 4.73±0.63 GPa at the bottom and 6.76 ±0.43 GPa at the top [9]. These differences between homogenized and experimental results for the bottom and top locations are respectively equal to 11% and 1%. Furthermore, the homogenization values fall within the confidence interval of the experimental results. These results validate both the homogenization models and the proposed approach.

5 Conclusion

A homogenization procedure has been developed to assess the effective stffness of sunflower bark. For this purpose, the effective properties of tissues at the mesoscopic scale were first

determined with respect to the porosity, volume ratio and shape of cells present at the microscopic scale. These values for the effective stiffness of parenchyma, sclerenchyma and xylem tissues were compared to values available in the literature. Some differences were observed due to: i) morphological properties of cells (volume ratio, shape, porosity) that can change from one plant to another; ii) the level of lignification of cells such as potatoes (not lignified) or wood (lignified). Theoretical results show that the Young's modulus of sunflower bark estimated using the homogenization model is in agreement with the experimental results. This homogenization model is expected to be suitable not only for sunflower bark but also for other plants by considering the following two main issues:

- in sunflowers, cell lumens are orientated along the stem. Other plants may exhibit a more complex spatial structure, such as wood, which presents different cell lumen configurations [26, 27]. In this latter case, cell lumens' orientations have to be considered in the spheroidal and cylindrical porosity models;
- tissues may exhibit different laminate configurations (typically wood tissues) rendering the mixture rule irrelevant. Finite element models may tackle this issue by modelling the spatial laminate configurations (see [28, 29]).

Acknowledgments

The authors would like to acknowledge the French National Research Agency (ANR), Céréales Vallée and ViaMéca for their financial support (ANR-10-ECOT-004 grant).

Bibliography

[1] M. Ardanuy, M. Antunes, J. Velasco, Vegetable fibres from agricultural residues as thermo-mechanical reinforcement in recycled polypropylene-based green foams, Waste Management 32 (2) (2011) 256–263.

[2] A. Ashori, A. Nourbakhsh, Bio-based composites from waste agricultural residues, Waste Management 30 (4) (2010) 680–684.

[3] A. Nourbakhsh, A. Ashori, Wood plastic composites from agro-waste materials: Analysis of mechanical properties, Bioresource technology 101 (7) (2010) 2525–2528.

[4] S. Panthapulakkal, A. Zereshkian, M. Sain, Preparation and characterization of wheat straw fibers for reinforcing application in injection molded thermoplastic composites, Bioresource technology.

[5] D. Wang, X. Sun, Low density particleboard from wheat straw and corn pith, Industrial Crops and Products 15 (1) (2002) 43–50.

[6] N. White, M. Ansell, Straw-reinforced polyester composites, Journal of Materials Science 18 (5) (1983) 1549–1556.

[7] H. Yang, D. Kim, H. Kim, Rice straw-wood particle composite for sound absorbing wooden construction materials, Bioresource Technology 86 (2) (2003) 117–121.

[8] FAOSTAT, Fao statistics division 2012: World sunflower seed area harvested, `http://faostat.fao.org/DesktopDefault.aspx?PageID=567`, last accessed mar, 2014.

[9] S. Sun, J.-D. Mathias, E. Toussaint, M. Grédiac, Hygromechanical characterization of sunflower stems, Industrial Crops and Products 46 (2013) 50–59.

[10] S. Sun, J.-D. Mathias, E. Toussaint, M. Grédiac, Characterizing the variance of mechanical properties of sunflower bark for biocomposite applications, Bioresources 9 (1), (2014) 922–937.

[11] A. Boccaccini, G. Ondracek, P. Mazilu, D. Windelberg, On the effective young's modulus of elasticity for porous materials: Microstructure modelling and comparison between calculated and experimental values, Journal of the Mechanical Behavior of Materials 4 (2) (1993) 119–128.

[12] G. Ondracek, The quantitative microstructure-field property correlation of multiphase and porous materials, Reviews on powder metallurgy and physical ceramics 3 (3-4) (1987) 205–322.

[13] R. Rice, Extension of the exponential porosity dependence of strength and elastic moduli, Journal of the American Ceramic Society 59 (11-12) (1976) 536–537.

[14] Z. Hashin, B. W. Rosen, The elastic moduli of fiber-reinforced materials, Journal of Applied Mechanics 31 (1964) 223.

[15] D. Hasselman, R. Fulrath, Effect of cylindrical porosity on young's modulus of polycrystalline brittle materials, Journal of the American Ceramic Society 48 (10) (1965) 545–545.

[16] R. W. Rice, Proposity of Ceramics, Vol. 12, CRC Press, (1998).

[17] J. Quiroz, R. Orellana, G. Canto, S. Rebollar, P. Herrera-Franco, Stem anatomical characteristics of the climbing palm desmoncus orthacanthos (arecaceae) under two natural growth conditions in a tropical forest, Revista de Biología Tropical 56 (2) (2008) 937–949.

[18] L. Maranho, M. Dziedzic, G. Muñiz, Y. Kuniyoshi, F. Galvão, Effects of the pollution by petroleum on the tracheids along the stem of podocarpus lambertii klotzsch ex endl., podocarpaceae, Brazilian Journal of Biology 69 (2) (2009) 263–269.

[19] P. J. Hudson, J. Razanatsoa, T. S. Feild, Early vessel evolution and the diverisification of wood function: Insights from malagasy canellales, American Journal of Botany 97 (1) (2010) 80–93.

[20] Uni-hamburg, Angiosperm wood, `http://www.biologie.uni-hamburg.de/b-online/e06/06h.htm`, last accessed mar, 2014.

[21] Y. Yu, B. Fei, B. Zhang, X. Yu, Cell-wall mechanical properties of bamboo investigated by in-situ imaging nanoindentation, Wood and Fiber Science 39 (4) (2007) 527–535.

[22] L. J. Gibson, M. F. Ashby, Cellular solids: structure and properties, Cambridge university press, (1999).

[23] D. Hepworth, J. Vincent, The mechanical properties of xylem tissue from tobacco plants (nicotiana tabacum 'samsun'), Annals of Botany 81 (6) (1998) 751–759.

[24] K. J. Niklas, Influence of tissue density-specific mechanical properties on the scaling of plant height, Annals of botany 72 (2) (1993) 173–179.

[25] K. J. Niklas, Plant biomechanics: an engineering approach to plant form and function, University of Chicago press, (1992).

[26] J.O. Hisashi Abe, K. Fukazawa : Fe-sem observations on the microfibrillar orientation in the secondary wall of tracheids, IAWA Bulletin 12(4), 431–438 (1991).

[27] G.T. Tsoumis: Science and technology of wood: structure, properties, utilization, Van Nostrand, Reinhold (1991).

[28] A. Bergander, L. Salmen: Cell wall properties and their effects on the mechanical properties of fibers. Journal of Materials Science 37, 151–156 (2002).

[29] J.A. Nairn: A numerical study of the transverse modulus of wood as a function of grain orientation and properties, Holzforschung 61(4), 406–413(2007).

CONCLUSION GÉNÉRALE

Ce travail de thèse a été réalisé au sein d'un projet beaucoup plus vaste : celui de l'ANR DEMETHER lancé en 2011. L'objectif principal du projet était d'élaborer un matériau composite d'origine bio-sourcée pouvant être utilisé à terme comme isolant thermique pour des bâtiments existants. En plus de cette exigence forte concernant les propriétés thermiques, il fallait contrôler que les propriétés mécaniques présentaient des valeurs minimales pour un usage concret de ce matériau, typiquement garantir que la manipulation de plaques ainsi réalisées serait possible sans briser les plaques en question, ou que leur fixation sur des parois puisse être envisagée sans détérioration des panneaux suite à des niveaux de contraintes locales trop élevées. C'est au sein de cette dernière problématique que ce travail de thèse a été conduit.

Un point important mérite d'être souligné : le matériau support à ce travail n'existait pas au lancement du travail mais la nature des ses constituants était connue : il s'agissait d'une part de broyats de tournesol et d'autre part d'une matrice à base de chitosane servant de liant. Un autre partenaire du projet : l'axe GEPEB de mon laboratoire, a d'abord eu pour tâche d'élaborer ce matériau composite, en regardant notamment comment la biomatrice devait être formulée pour qu'elle puisse effectivement servir de liant comme attendu. De mon côté, j'ai mis à profit cette phase très amont du projet pour étudier de près le comportement mécanique des constituants de base des tiges de tournesol que sont l'écorce et la moelle. Il faut souligner que la littérature était complètement muette sur le sujet au début de ce travail. En effet, ce matériau n'avait jamais été utilisé pour des applications structurelles ou semi-structurelles et il n'était considéré quasiment que comme un déchet. Cette première phase du travail a abouti aux résultats présentés dans les deux premiers chapitres de la thèse, à savoir une caractérisation de l'écorce et de la moelle des tiges de tournesol, avec une prise en compte des dispersions via une analyse statistique poussée. Ce travail a permis de bien mettre en évidence l'influence de la hauteur de prélèvement des échantillons dans la tige ainsi que celle de l'humidité.

Les premiers biocomposites élaborés par les partenaires de l'axe GEPEB de l'Institut Pascal ont été mis à disposition lors de la troisième année de ce travail de thèse, ce qui a alors permis de les soumettre à des essais mécaniques. Les résultats des essais conduits de façon "classique" (essais de traction/compression) seront présentés dans le mémoire de thèse d'une autre étudiante qui a travaillé sur l'élaboration du matériau, ceci afin d'analyser les liens étroits entre propriétés mécaniques et divers paramètres comme le procédé de fabrication et la formulation de la biomatrice. J'ai pour ma part concentré mes efforts sur une caractérisation

de ce matériau incluant les effets locaux avec l'étude de leur lien sur le comportement global. Une originalité a été d'adapter puis d'utiliser un système de mesure de champs cinématiques sans contact déjà existant au laboratoire : la méthode dite de la grille. Cette adaptation (donc différente et forcément plus complexe qu'une utilisation directe d'un moyen déjà éprouvé) était justifiée par la nature même du matériau qui comporte des cavités apparentes ainsi que par le fait que les copeaux de moelle sont très souples, ce qui interdit tout dépôt de grille en suivant la procédure utilisée classiquement au laboratoire. Les résultats obtenus, présentés dans le chapitre trois de ce travail, ont bien mis en évidence les mécanismes de déformation de ce matériau très fortement hétérogène. Ces mécanismes s'appuient beaucoup sur des niveaux de compression très importants (au regard des niveaux atteints au sein de broyats eux-mêmes) atteints dans les zones où les cavités sont bien visibles.

Enfin, un travail d'homogénéisation a été réalisé dans le cadre de cette thèse. Il est présenté au chapitre quatre du mémoire. L'objectif était d'examiner si la nature cellulaire des phases principales de l'écorce des tiges de tournesol, à savoir les tissus sclérenchyme, xyleme et parenchyme, et la connaissance des propriétés des matériaux constitutifs, trouvés dans la littérature vu les échelles concernées et la difficulté à mesurer en interne ces grandeurs, pouvaient conduire à une estimation réaliste des propriétés élastiques globales. Il s'est avéré que c'était bien le cas même si des hypothèses parfois fortes ont dû être formulées, notamment concernant la forme des phases ou des vides.

Au bilan, il faut considérer ce travail comme une première contribution à la connaissance du comportement mécanique des tiges de tournesol et des biocomposites réalisés avec du broyat issu de ces tiges. Vu l'absence totale de connaissance *a priori* sur le sujet et vu le phasage du projet lui-même qui a conduit à disposer des premiers biocomposites en dernière année de thèse, il est clair que des études complémentaires devront être conduites pour mieux caractériser le comportement mécanique des biocomposites et pour mieux comprendre les mécanismes de déformation et de rupture en leur sein. Ceci pourrait d'ailleurs s'avérer indispensable si l'emploi de ce matériau devait dépasser celui d'un isolant thermique pour le bâtiment, par exemple pour passer à des applications semi-structurelles. L'influence de la formulation de la matrice et de sa fraction volumique au sein du composite devra notamment être étudiée en détail. Les travaux présentés dans ce mémoire constituent cependant une première étude exploratoire qui a déjà permis de caractériser minitieusement les propriétés mécaniques des broyats de tournesol de type écorce et moelle, et de comprendre les grandes lignes des mécanismes de déformation de ce nouveau matériau composite fortement hétérogène.

ANNEXE A

Résultats supplémentaires pour le chapitre 1

Ecorce de tige de tournesol :

- La figure 1-a représente une éprouvette d'écorce montée dans la micro-machine de traction décrit dans la section 2.4 du chapitre 1.
- La figure 1-b représente des courbes de traction typique de trois éprouvettes d'écorce prélevées à trois différentes hauteurs le long d'une tige. A partir de cette figure, on peut observer que le module de Young de l'écorce augmente avec la hauteur de prélèvement de l'éprouvette, cette tendance a été discutée dans la section 3.2.1 du chapitre 1.

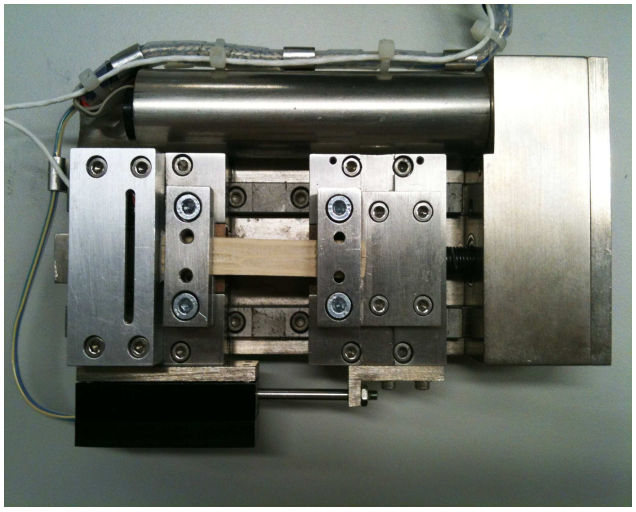

a- Specimen of bark in
Deben MICROTEST testing machine

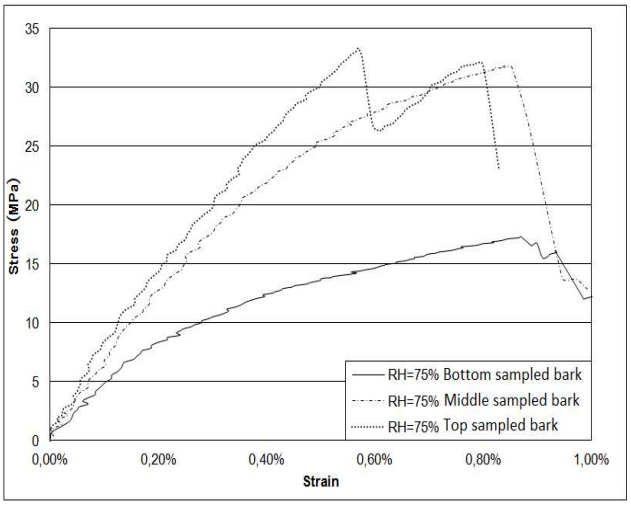

b- Typical testing curves

Figure 1 Experimental tensile test of sunflower bark specimen

Ecorce de tige de tournesol :

La figure 2 représente la déformation maximale de l'éprouvette d'écorce pour différentes conditions d'humidité relative et hauteurs de prélèvement le long des tiges. La discussion sur ces résultats se trouve dans la section 3.2.1 du chapitre 1.

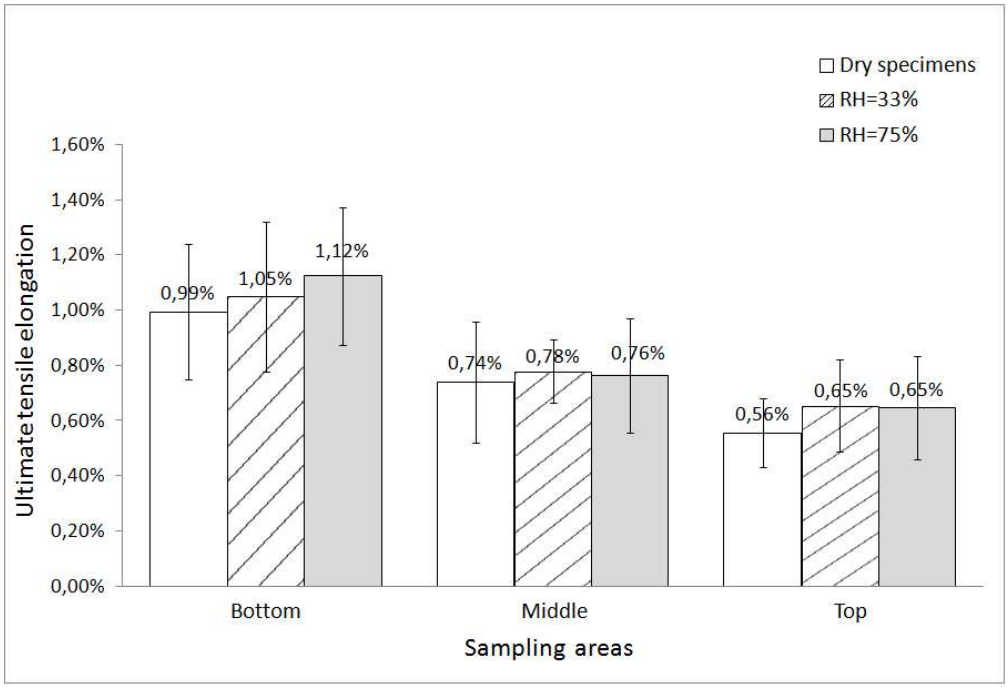

Figure 2 Ultimate elongation of bark of sunflower stem

Moelle de tige de tournesol :

- La figure 3-a représente une éprouvette de moelle montée dans la machine de compression décrit dans la section 2.4 du chapitre 1.
- La figure 3-b représente des courbes de compression typique de trois éprouvettes de moelle prélevées à trois différentes hauteurs le long d'une tige. A partir de cette figure, on peut observer que le module de Young de la moelle augmente avec la hauteur de prélèvement le long de la tige, cette tendance a été discutée dans la section 3.2.2 du chapitre 1.

a- Specimen of pith in INSTRON testing machine

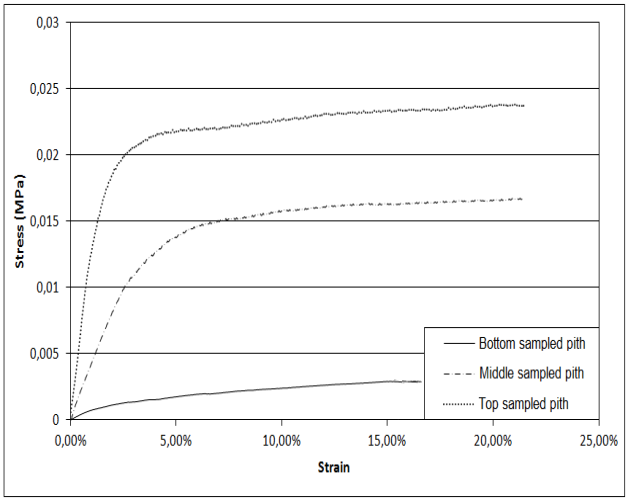

b- Typical testing curves

Figure 3 Experimental tensile test of sunflower bark specimen

Moelle de tige de tournesol :

La figure 4 représente la limite de déformation élastique de l'éprouvette de moelle pour différentes conditions d'humidité relative et hauteurs de prélèvement d'éprouvette. La discussion de ce résultat se trouve dans la section 3.2.2 du chapitre 1.

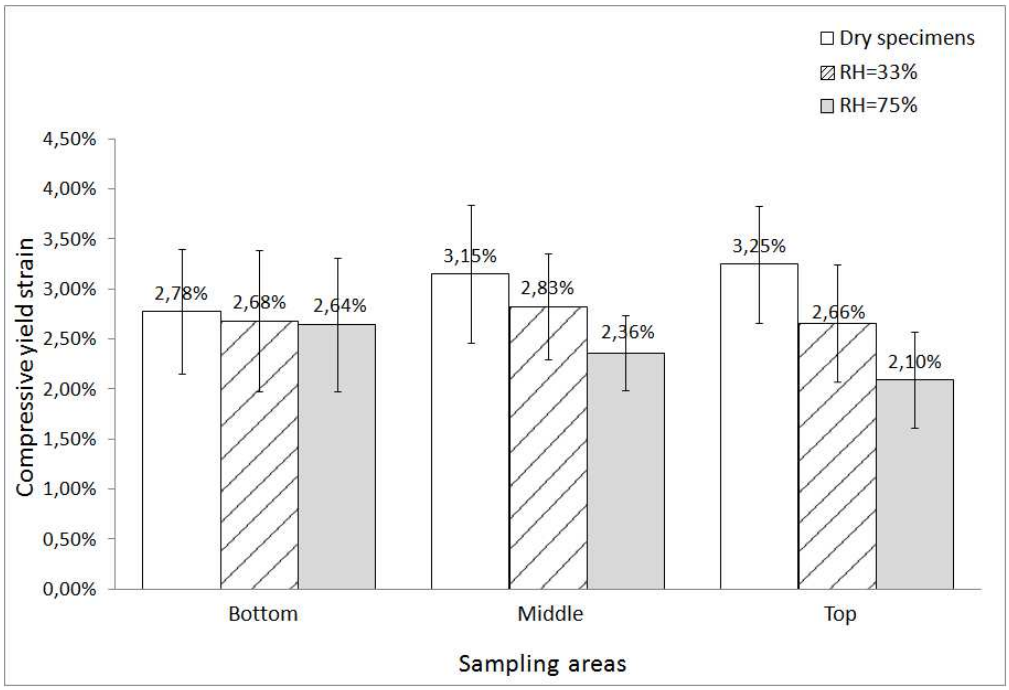

Figure 4 Compressive yield strain of pith of sunflower stem

ANNEXE B

Résultats supplémentaires pour le chapitre 2

Les figures 1 à 8 représentent les histogrammes et probabilités de distribution du module de Young d'écorce pour chaque condition de test (humidité relative et position de prélèvement le long de la tige). En fait, une figure typique a été présentée et discutée dans la section 3.2 du chapitre 2. L'ensemble de toutes ces figures montrent les trois lois de distribution possibles suivies par le module de Young de l'écorce : la loi normale, la loi log-normale et la loi de Weibull.

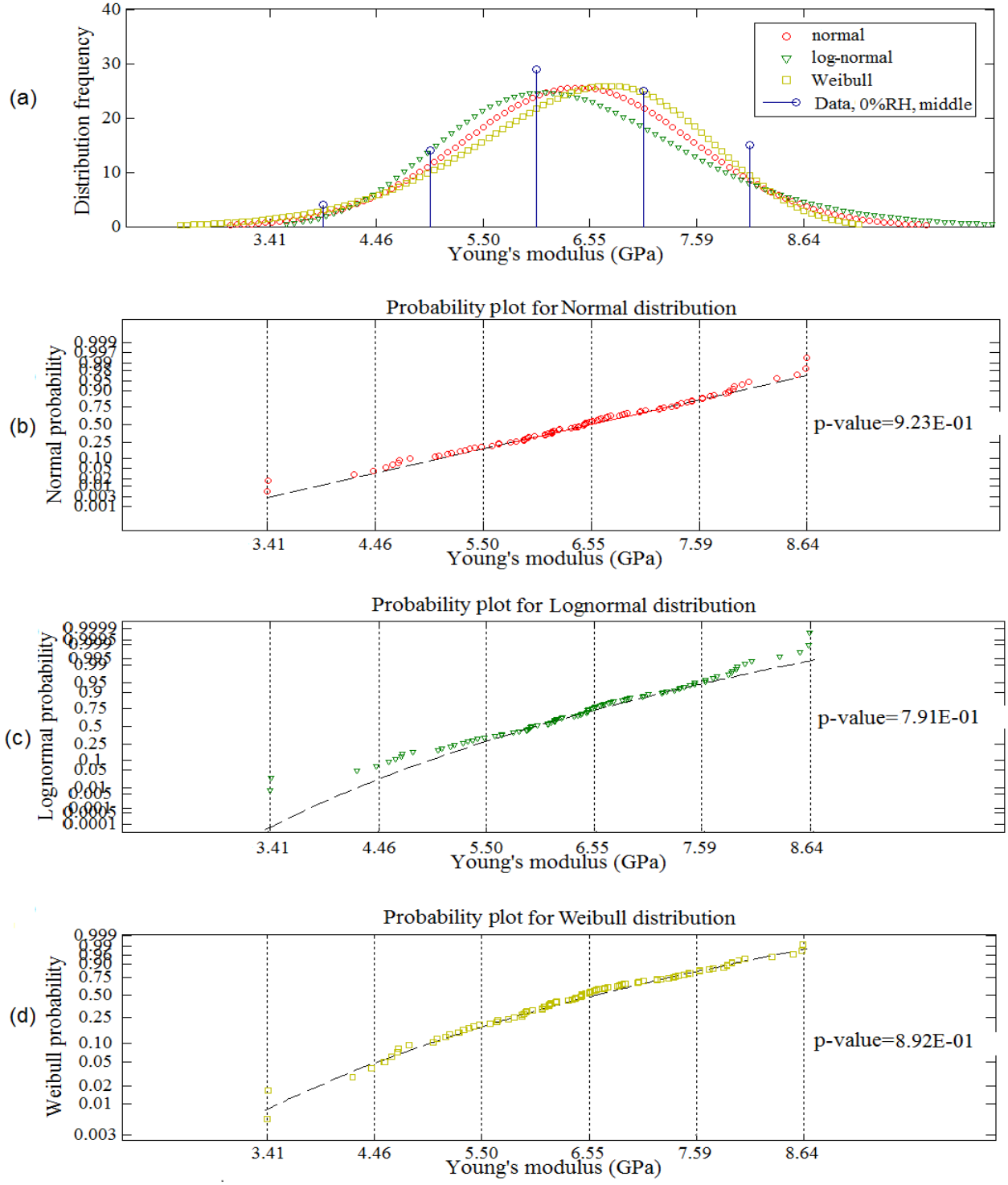

Figure 1 Histogram and probability plot at 0% RH and middle location : (a) Histogram ; (b) normal probability plot ; (c) log-normal probability plot ; and (d) Weibull probability plot

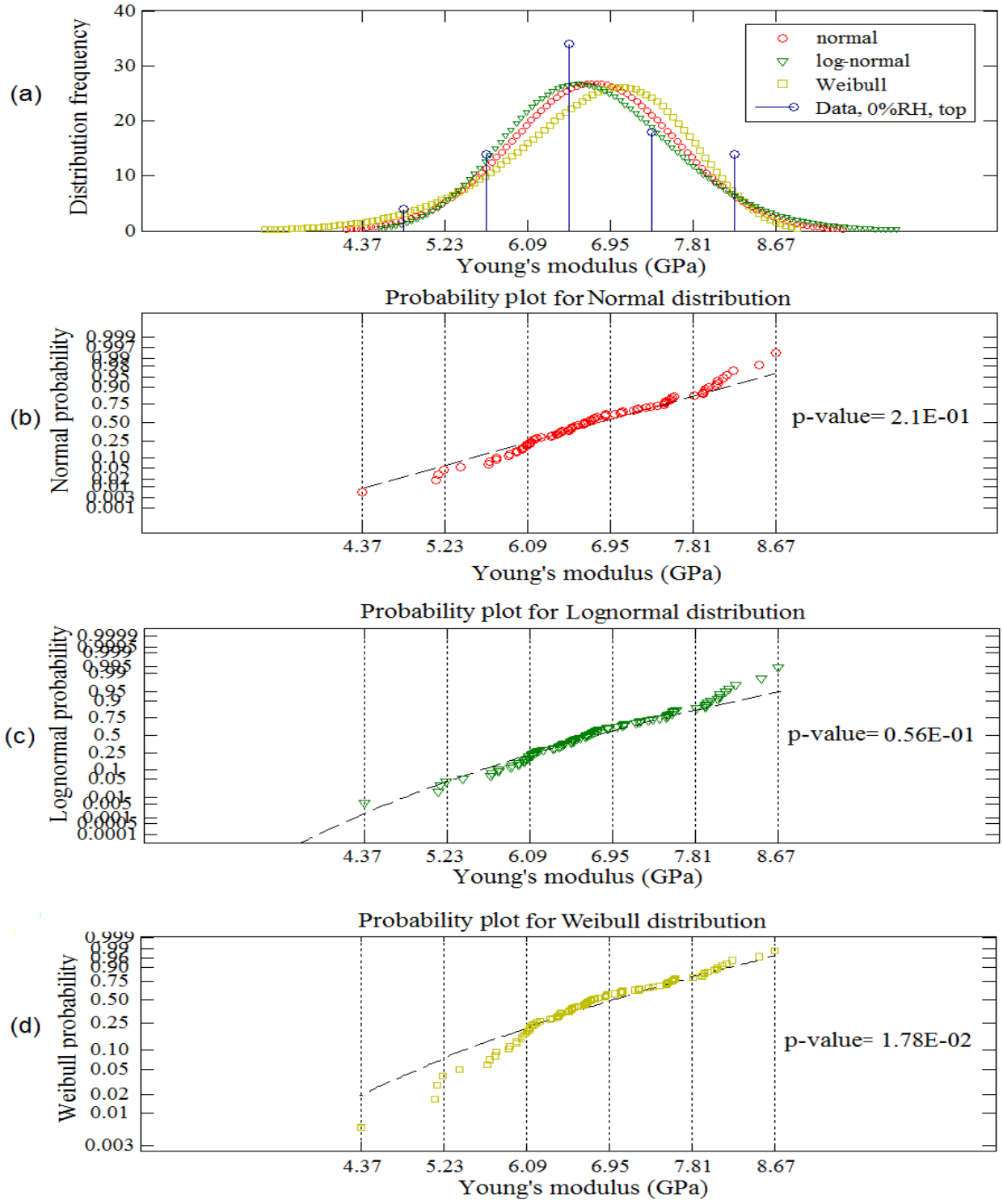

Figure 2 Histogram and probability plot at 0% RH and top location : (a) Histogram ; (b) normal probability plot ; (c) log-normal probability plot ; and (d) Weibull probability plot

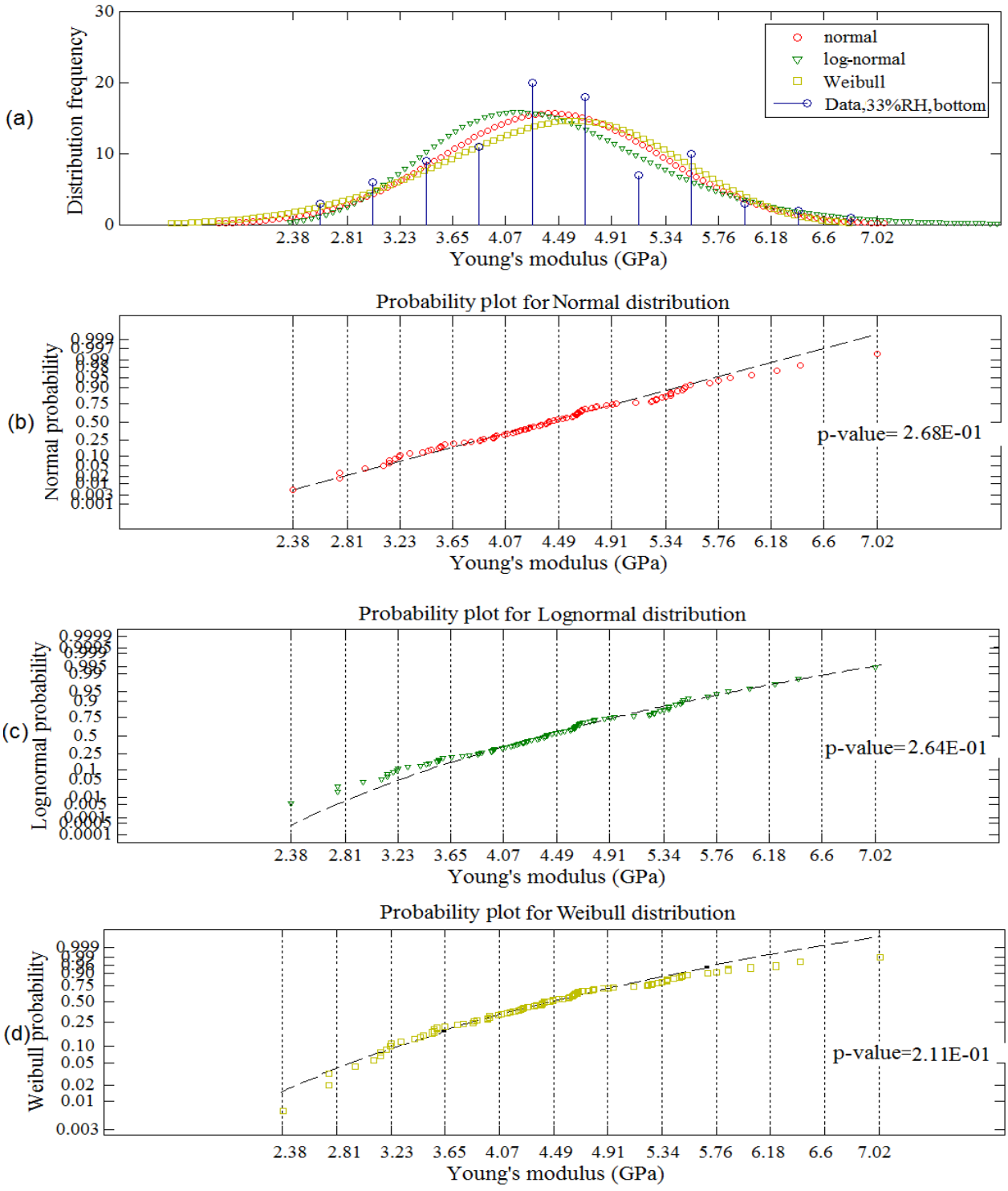

Figure 3 Histogram and probability plot at 33% RH and bottom location : (a) Histogram ; (b) normal probability plot ; (c) log-normal probability plot ; and (d) Weibull probability plot

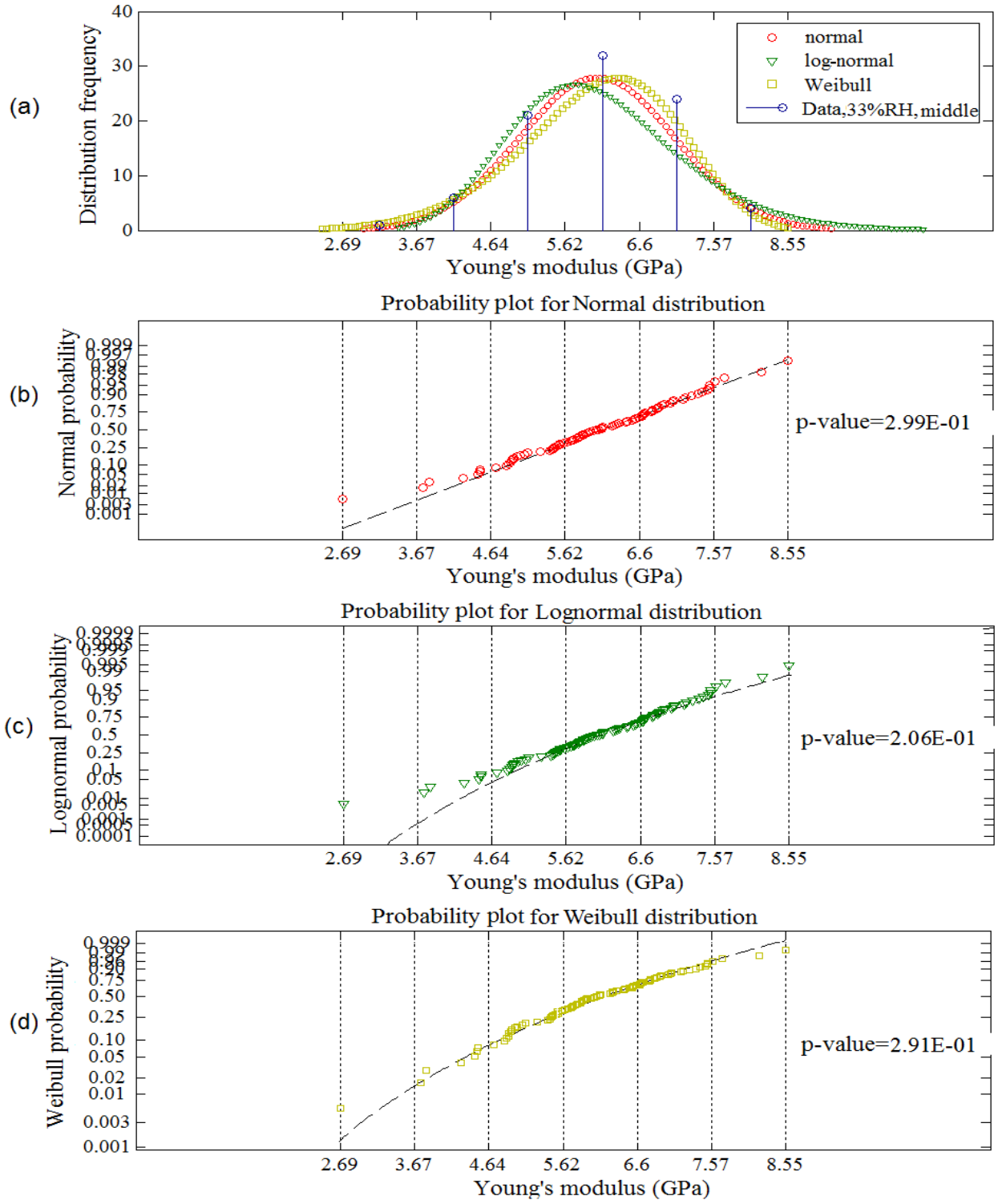

Figure 4 Histogram and probability plot at 33% RH and middle location : (a) Histogram ; (b) normal probability plot ; (c) log-normal probability plot ; and (d) Weibull probability plot

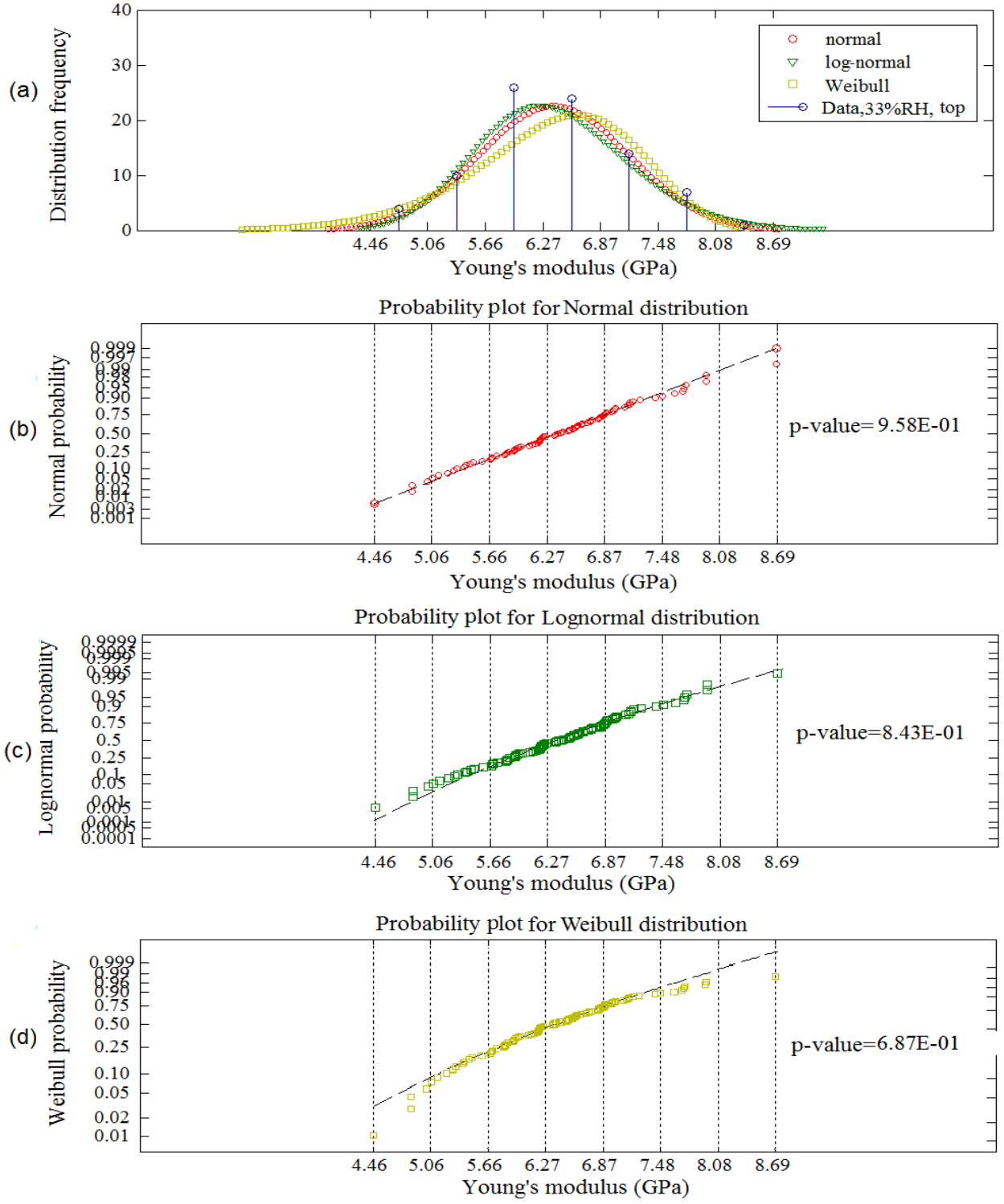

Figure 5 Histogram and probability plot at 33% RH and top location : (a) Histogram ; (b) normal probability plot ; (c) log-normal probability plot ; and (d) Weibull probability plot

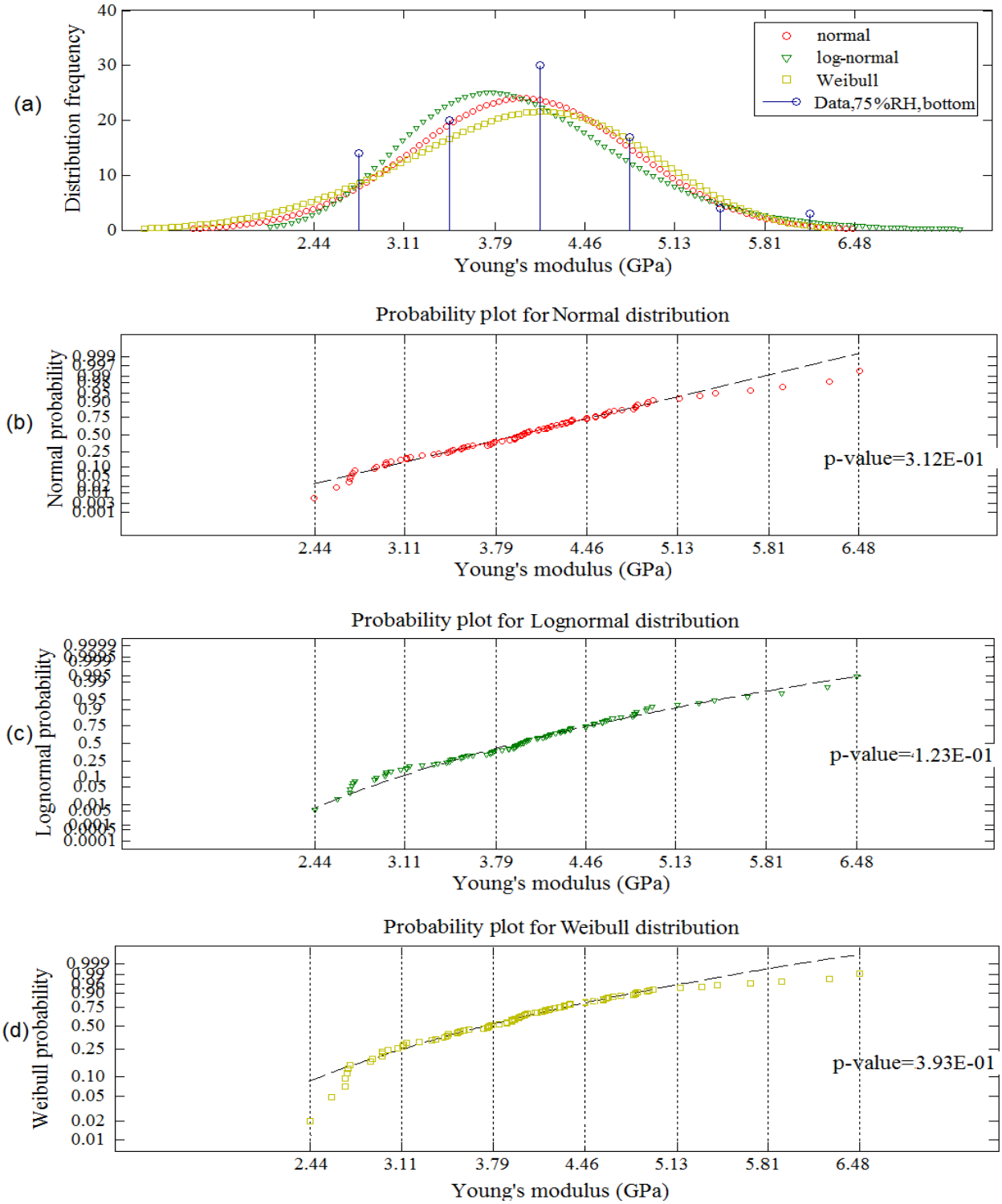

Figure 6 Histogram and probability plot at 75% RH and bottom location : (a) Histogram ; (b) normal probability plot ; (c) log-normal probability plot ; and (d) Weibull probability plot

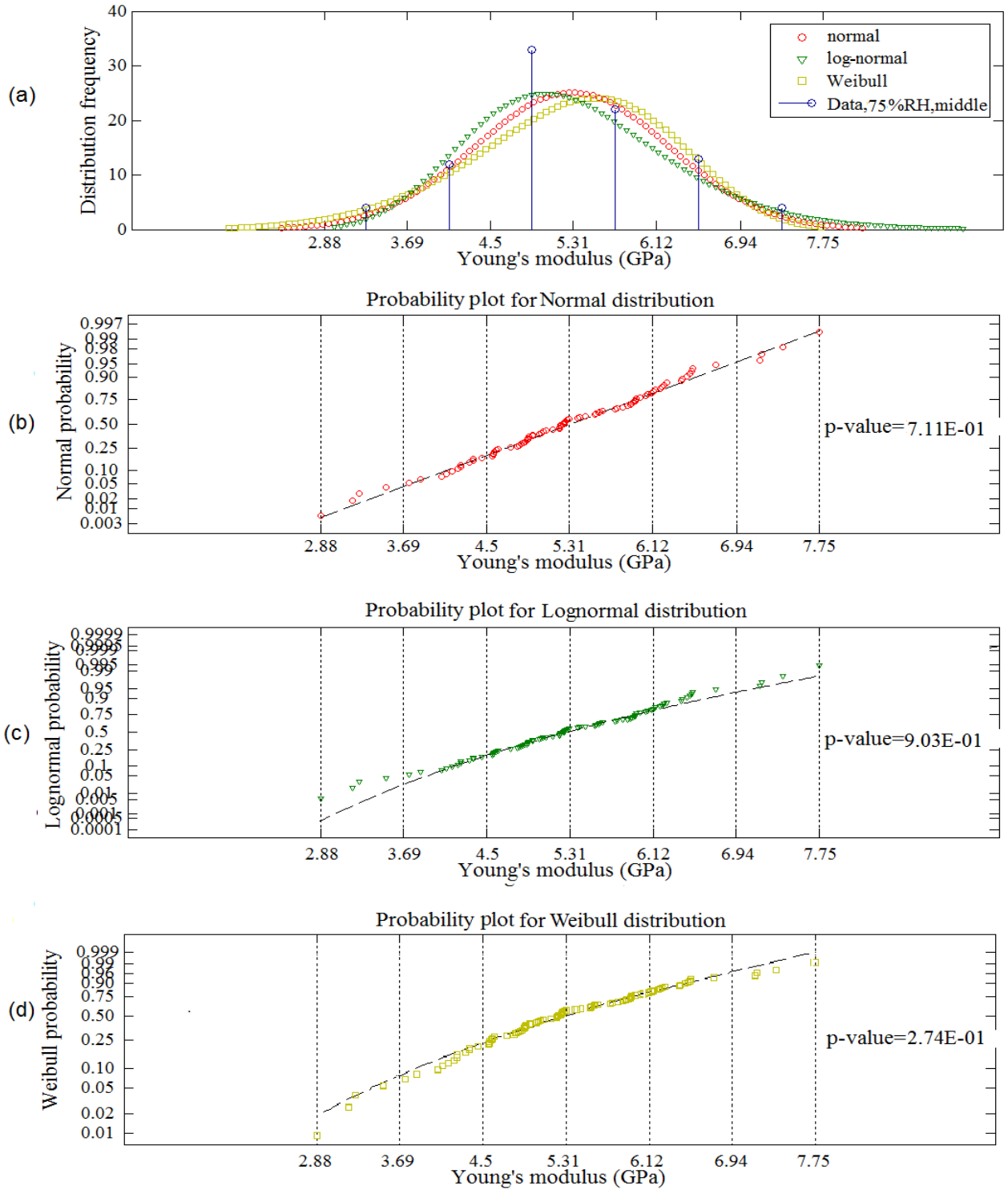

Figure 7 Histogram and probability plot at 75% RH and middle location : (a) Histogram ; (b) normal probability plot ; (c) log-normal probability plot ; and (d) Weibull probability plot

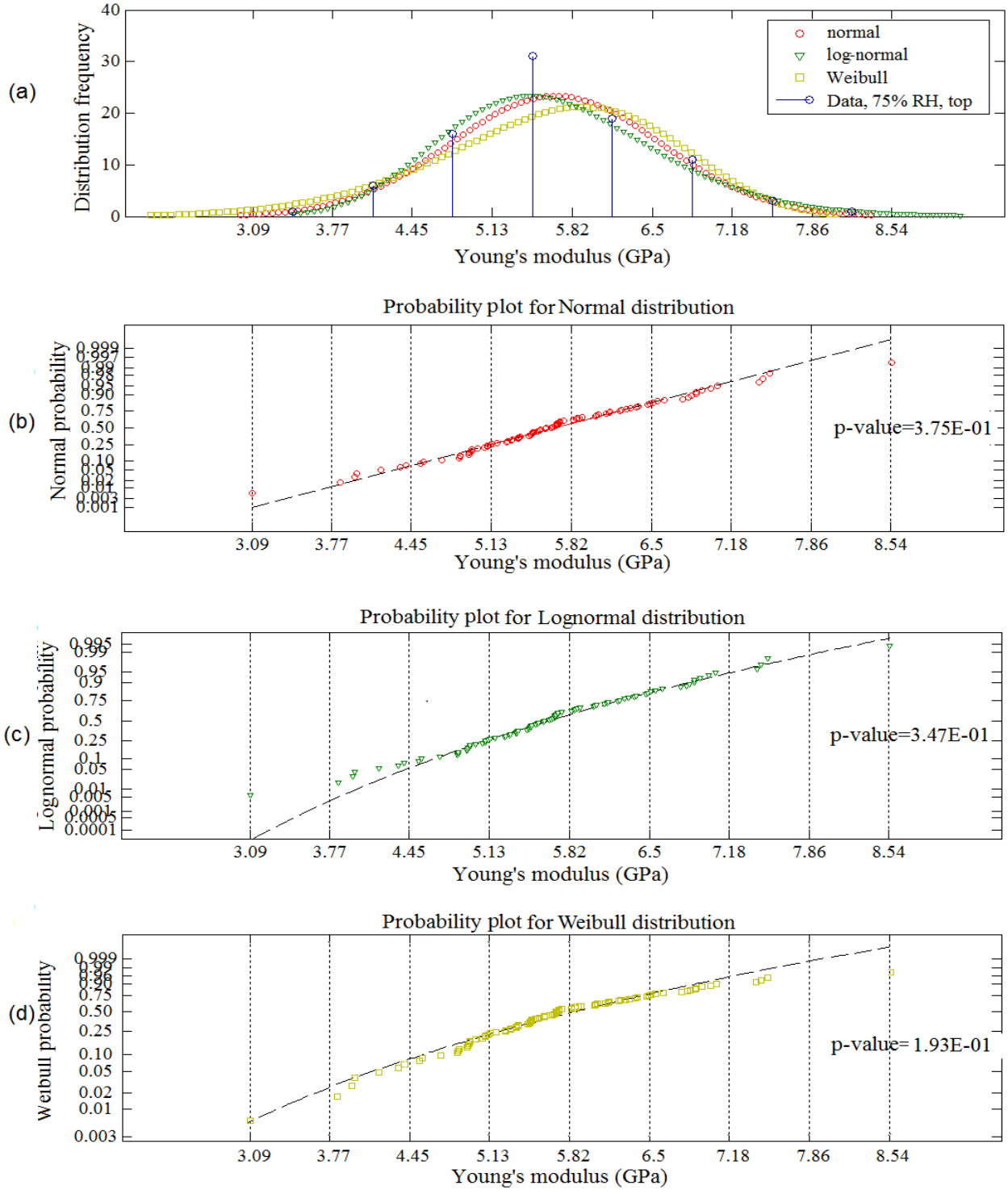

Figure 8 Histogram and probability plot at 75% RH and top location : (a) Histogram ; (b) normal probability plot ; (c) log-normal probability plot ; and (d) Weibull probability plot

Le tableau 1 représente les valeurs de p du test de distribution de la loi normale, de la loi log-normale et de la loi de Weibull. En fait, ces résultats ont été montrés et discutés avec la figure 4 de la section 3.2 du chapitre 2. Ce tableau consiste à présenter les résultats sous forme numérique. En plus, le nombre de classe de chaque groupe de donnée déterminé par le test de $chi2gof$ de Matlab (voir la fin de la section du chapitre 2) est reporté.
english

normal distribution			
	Bottom	Middle	Top
0%	4.09E-01 (7 bins)	9.23E-01 (7 bins)	2.1E-01 (6 bins)
33%	2.68E-01 (7 bins)	2.99E-01 (6 bins)	9.58E-01 (7 bins)
75%	3.12E-01 (7 bins)	7.11E-01 (7 bins)	3.75E-01 (7 bins)

log-normal distribution			
	Bottom	Middle	Top
0%	4.07E-01 (7 bins)	7.91E-01 (7 bins)	3.56E-01 (6 bins)
33%	2.64E-01 (7 bins)	2.68E-01 (6 bins)	8.43E-01 (7 bins)
75%	1.23E-01 (7 bins)	9.03E-01 (7 bins)	3.47E-01 (7 bins)

Weibull distribution			
	Bottom	Middle	Top
0%	3.08E-01 (7 bins)	8.92E-01 (7 bins)	1.78E-02 (6 bins)
33%	2.11E-01 (7 bins)	2.91E-01 (6 bins)	6.87E-01 (7 bins)
75%	3.93E-01 (7 bins)	2.74E-01 (7 bins)	1.93E-01 (7 bins)

Table 1 p-value of the Normal Lognormal and Weibull distribution tests

Le tableau 2 représente les valeurs de p du test de significativité sur l'influence de l'humidité relative et la position de prélèvement de l'éprouvette le long de la tige. En fait, ces résultats ont été montrés et discutés avec la figure 5 dans la section 3.2 du chapitre 2. Ce tableau consiste à présenter les résultats sous forme numérique.

significance test between dataset A/dataset B	**p-value**
0%/33%, Bottom	3.5E-03
0%/33%, Middle	6.8E-03
0%/33%, Top	5.27E-04
33%/75%, Bottom	8.6E-05
33%/75%, Middle	2.5E-07
33%/75%, Top	6.19E-08
Bottom/Middle, 0%	<1.00E-16
Middle/Top, 0%	2,71E-02
Bottom/Middle, 33%	<1.00E-16
Middle/Top, 33%	3.44E-02
Bottom/Middle, 75%	<1.00E-16
Middle/Top, 75%	6.9E-03

Table 2 p-value of two-sample t-test

Le tableau 3 est le matrice de résultat en appliquant la fonction $corrcoef(DATA)$ de Matlab (voir section 2.2.3 du chapitre 2). Cette fonction a été utilisée pour calculer les corrélation de module de Young d'écorce entre différentes humidités relatives et la position de l'éprouvette le long de la tige. Le matrice $DATA$ est composé de module de Young de l'écorce dont les linges sont les numéros de éprouvette et les colonnes sont les différentes conditions du test. En fait, les résultats utiles pour notre cas d'étude sont soulignées dans cette matrice (voir également les tableaux 1 et 2 dans la section 3.4 du chapitre 2).

$$R(i,j) = \left|\begin{array}{c|ccccccccc} i\backslash j & 0B & 33B & 75B & 0M & 33M & 75M & 0T & 33T & 75T \\ \hline 0B & 1.00 & 0.81 & 0.71 & 0.24 & 0.41 & 0.18 & 0.24 & 0.21 & 0.06 \\ 33B & \underline{0.81} & 1.00 & 0.64 & 0.32 & 0.41 & 0.10 & 0.06 & 0.10 & -0.01 \\ 75B & \underline{0.71} & \underline{0.64} & 1.00 & 0.20 & 0.35 & 0.42 & 0.08 & 0.23 & 0.13 \\ 0M & \underline{0.24} & 0.32 & 0.20 & 1.00 & 0.76 & 0.60 & 0.01 & 0.12 & 0.11 \\ 33M & 0.41 & \underline{0.41} & 0.35 & \underline{0.76} & 1.00 & 0.57 & 0.05 & 0.26 & 0.06 \\ 75M & 0.18 & 0.10 & \underline{0.42} & \underline{0.60} & \underline{0.57} & 1.00 & 0.10 & 0.23 & 0.22 \\ 0T & \underline{0.24} & 0.06 & 0.08 & \underline{0.01} & 0.05 & 0.10 & 1.00 & 0.56 & 0.46 \\ 33T & 0.21 & \underline{0.10} & 0.23 & 0.12 & \underline{0.26} & 0.23 & \underline{0.56} & 1.00 & 0.56 \\ 75T & 0.03 & -0.01 & \underline{0.13} & 0.11 & 0.06 & \underline{0.22} & \underline{0.46} & \underline{0.56} & 1.00 \end{array}\right| .$$

Table 3 Correlation coefficient matrix (0, 33, 75 = 0%, 33%, 75%; B, M, T=Bottom, Middle, Top)

ANNEXE C

Résultats supplémentaires pour le chapitre 3

La figure 1 représente les valeurs moyennes de déformation de l'écorce et de la moelle dans chacun des quatre composites. En fait, les résultats des éprouvettes 1-1 et 2-1 on été déjà présentés et discutés dans la section 4.4 du chapitre 3. Cette figure montre que, pour les quatre éprouvettes, la déformation de la moelle est toujours supérieur que celle de l'écorce.

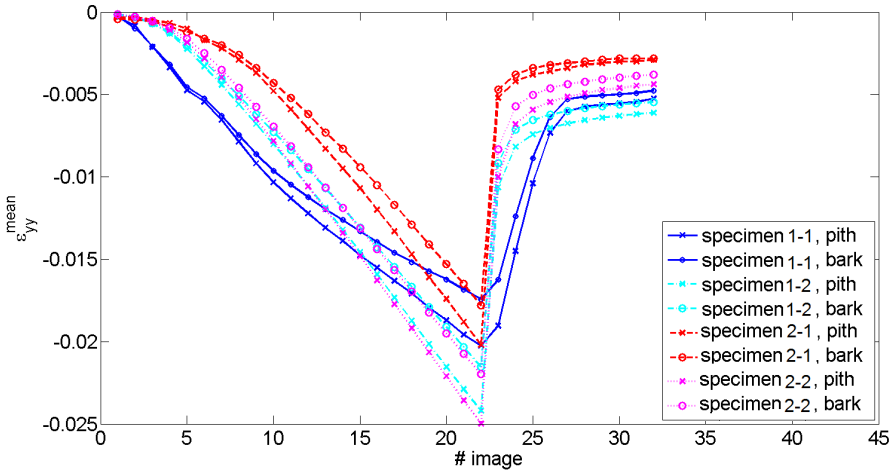

Figure 1 Mean strain in bark and pith vs. # image. All specimens

La figure 2 représente les courbes de fréquence cumulée pour la distribution de la déformation dans l'écorce et dans la moelle des quatre éprouvettes pour la charge maximale. En fait, les résultats des éprouvettes 1-1 et 2-1 on été déjà présentés et discutés dans la section 4.4 du chapitre 3. Pour les quatre composite testés, la courbe de l'écorce est toujours décalée vers la droite par rapport à la courbe de la moelle.

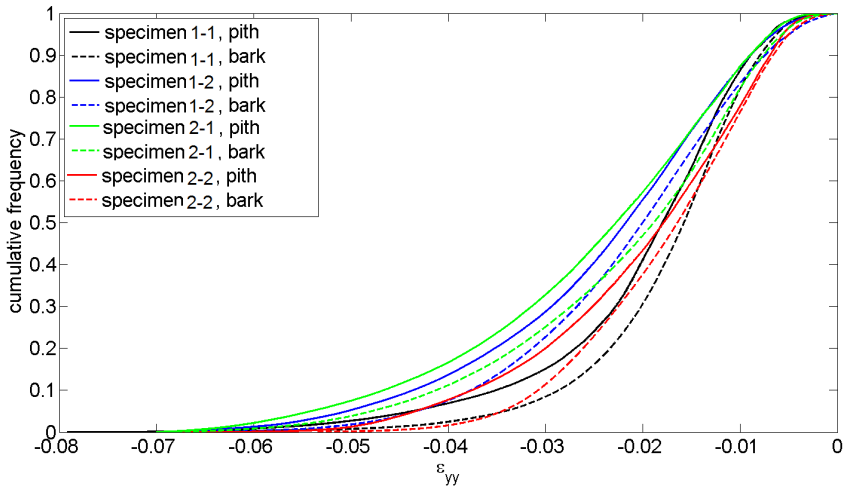

Figure 2 Cumulative frequency for the distribution of the strain in bark and pith at the maximum load. All specimens

ANNEXE D

Procédure de marquage des grilles sur la surface du biocomposite

La méthode de grille est basée sur le codage de grille périodique solitaire de la surface à étudier. Les grilles sont souvent transférées ou collées à la surface à étudier par une couche de colle. Cependant ces techniques ne sont pas toutefois applicables à certain cas, par exemple pour le biocomposite réalisé dans le cadre du projet DEMETHER, où l'éprouvette et ces phases constructives soient moins rigides que la colle. La technique de marquage de la surface décrit ici est développée pour l'application au matériau peu rigide, soit disposé ou pas une porosité à la surface à étudier. Ici on présente les diverses étapes pour marquer la surface de la biocomposite à base de tige de tournesol du type moelle et écorce réalisé dans le cadre de ce projet DEMETHER.

1. Tous d'abord il faut remplir ces porosités qui se présentent sur la surface à marquer. Le remplisseur utilisé est un mastic colle élastique (Sikaex-11FC+, Le Bourget, France) qui possède une rigidité est très faible d'ordre de 0.6 MPa. Sa souplesse permet de réduire au maximum l'impact sur comportement mécanique globale de biocomposite. On utilise un couteau à mastic de peintre en acier pour appliquer le mastic à la biocomposite. Une fois que les trous sont remplis, voire Figure 1, laissé sécher pendant 24 h.

Figure 1 Remplissage des trous dans le biocomposite

2. Une fois le mastic est séché, on ponce la surface en utilisant la polisseuse pour éliminer le mastic collé sur les broyats et rendre la surface plane, voire l'état finale dans Figure 2.. La surface de l'échantillon doit être bien examinée, au cas où il y a des défauts de

planéité, il faut rappliquer des étapes 1 et 2.

Figure 2 Polissage du biocomposite

3. Une peinture blanche (Peintures Techniques Julien, Montataire, France) est ensuite pulvérisée sur la surface de l'éprouvette. Il faut appliquer plusieurs couches de peinture pour cacher le motif de la surface l'échantillon et rendre une couleur blanche uniforme (une couche tous les 30 min), voire l'état finale dans Figure 3. Dès que la peinture est totalement séchée (24 h), on examine la planéité de la surface. Au cas où la surface n'est pas plane, il faut rappliquer des étapes 2 et 3.

Figure 3 Peinture du biocomposite

4. Une couche de colle très fine (Bâton de colle, UHU blanc) est posée sur la surface de l'échantillon et le masque est doucement appliqué sur la colle. Ceci est pour éviter le masque se gonfler au cours de la peinture de grille due à la mouillabilité. Les bords de masque devraient être bien fixés par des plaques métalliques planes, voire Figure 4.

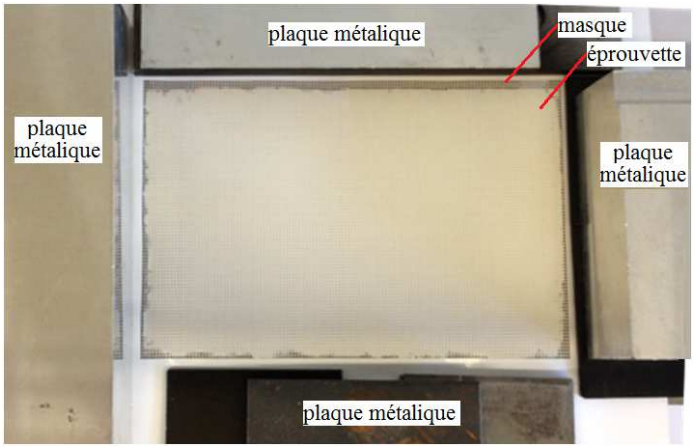

Figure 4 Fixation du masque de grille

5. L'encre acrylique noir (Réf. 28702, Schmincke, Erkrath, Allemagne) dilué à 40% (m/m) dans l'eau déminéralisé, a ensuite pulvérisée à travers du masque avec l'aérographe (Paasche Airbrush Company, Chicago, IL, USA). La distance entre l'aérographe et la surface de l'échantillon est environ 20 cm. Plusieurs couche fine (5 couche en totale avec une couche tous les 2 min) devrais être appliquée jusqu'à la surface atteindre à la couleur noire et uniforme.
6. Le masque est enlevé dès le séchage de peinture (2 min) avant la colle appliqué dans l'étape 4 soit complètement séché.
7. Examiner l'état de marquage, au cas où du défaut due au gonflement du masque, on élimine les grilles avec l'eau déminéralisé et rapplique les étapes 4-7. L'état final de la marquage est présenté dans Figure 5

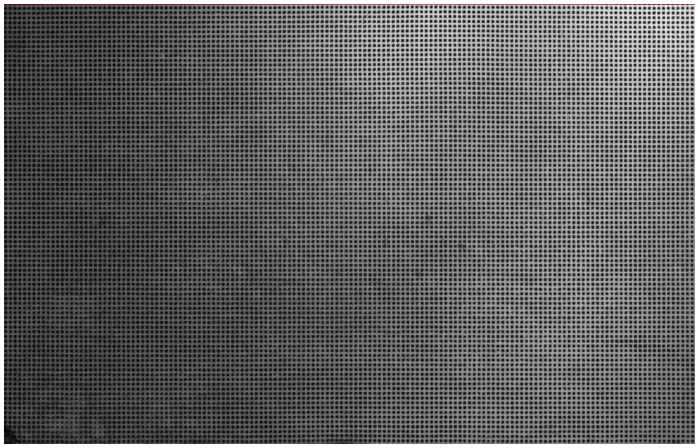

Figure 5 Biocomposite marqué de la grille

ANNEXE E

Méthode d'extraire de l'écorce et moelle

Pour retirer le masque de l'écorce et la moelle de la surface étudiée, il faut d'abord supprimer la zone où il y a du mastic et obtenir le masque *M_sans_mastic*. Ceci peut être facilement effectué en utilisant les commandes de Matlab décrit ci-dessous (voire la procédure dans Figure 1) :

Conversion d'images en niveaux de gris.

```
M = imread('E:\surface eprouvette.png');
if ndims(M) == 3
M = rgb2gray(M);
end
figure,imagesc(J,[0 265]),colormap(jet),axis equal;colorbar;
```

Le réglage des seuils en niveaux de gris pour supprimer la zone de mastique.

```
[Mt,Nt]=size(M);
for it=1:Mt
for jt=1:Nt
if M(it,jt)<88
M_sans_mastic(it,jt)=0;
elseif M(it,jt)>=88
M_sans_mastic(it,jt)=1;
end
end
end
M_sans_mastic=double(M_sans_mastic);
M_sans_mastic(M_sans_mastic==0) = nan;
figure,f=imagesc(M_sans_mastic);set(f,'alphadata',~isnan(M_sans_mastic))
```

Le masque *M_sans_mastic* obtenu est une matrice composée de 1 et *nan*, le masque de mastic est l'inverse du masque *M_sans_mastic*, ce qui égale à ones(Mt, Nt) - M_sans_mastic. Ainsi que pour obtenir le masque de l'écorce *M_ecorce* et la moelle *M_ecorce*, il faut effectuer les étapes suivantes :

1. D'abord il faut obtenir le masque de moelle *M_moelle brut* en utilisant les commende Matlab décrit dessous. Le masque obtenu est *brut* car il contient des morceaux d'écorce dont la niveaux de grise est dans la même fourchette de ceci de la moelle. La seuil de niveau de grise est choisie avec une procédure de tâtonnement, dont le but est de grader le plus possible les zones occupées par la moelle et en même temps, enlever le plus possible des morceaux d'écorce. Les résultat en appliquant cette procédure sont présentés dans Figure 2)

Conversion d'image de la masque sans mastic en niveaux de gris.

```
M_sans_mastic_b=M_sans_mastic.*M;
figure,f=imagesc(M_sans_mastic_b);
set(f,'alphadata',~isnan(M_sans_mastic_b));colormap(jet);colorbar
```

Le réglage des seuils en niveaux de gris pour supprimer la zone de l'écorce.

```
[Mt,Nt]=size(M);
for it=1:Mt
for jt=1:Nt
if M_sans_mastic_b(it,jt)<185
M_moelle(it,jt)=0;
elseif M_sans_mastic_b (it,jt)>=185
M_moelle(it,jt)=1;
end
end
end
M_moell=double(M_moell);
M_moell(M_moell==0) = nan;
figure,f=imagesc(M_moell);set(f,'alphadata',~isnan(M_moell))
```

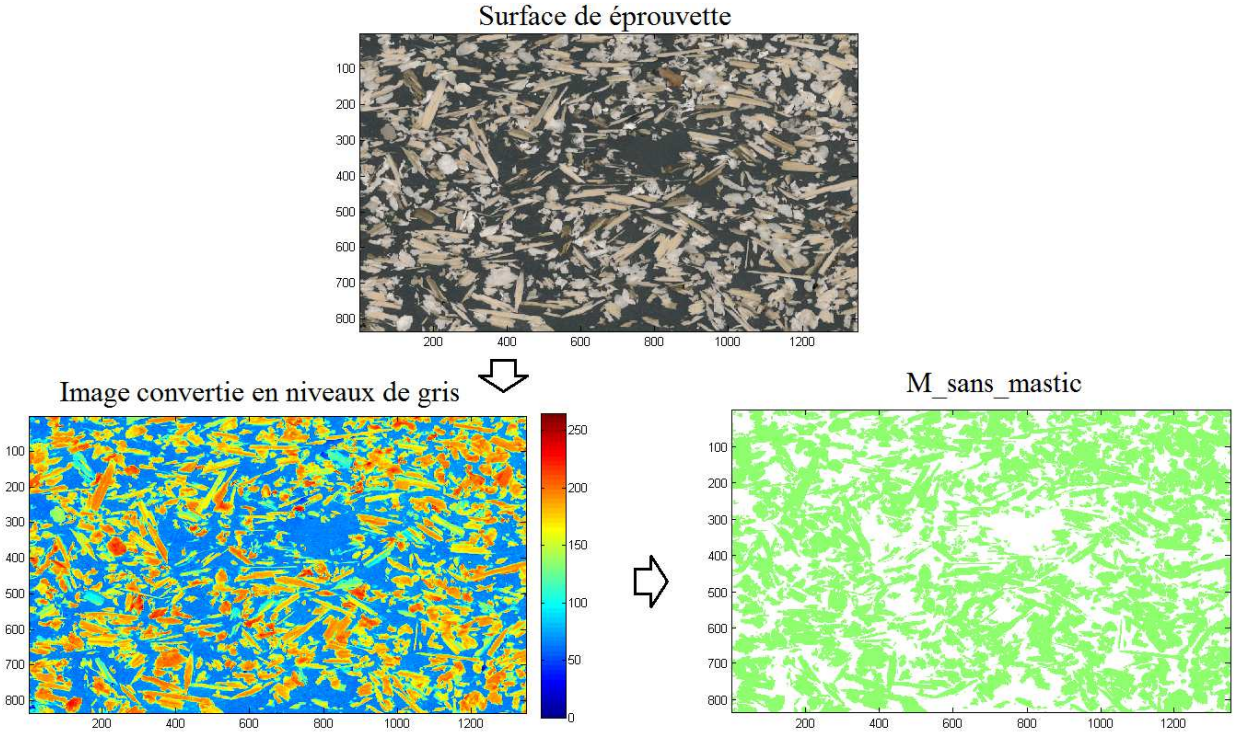

Figure 1 Procédures pour l'obtention du masque sans mastic

2. Le masque de moelle *M_moelle brut* obtenue est ainsi superposé à l'image de surface étudiée en utilisant la logicielle GIMP 2. Les outilles de peinture de cette logicielle sont utilisés pour remplir des zone manquant et supprimer des morceaux d'écorce, voire Figure 3)

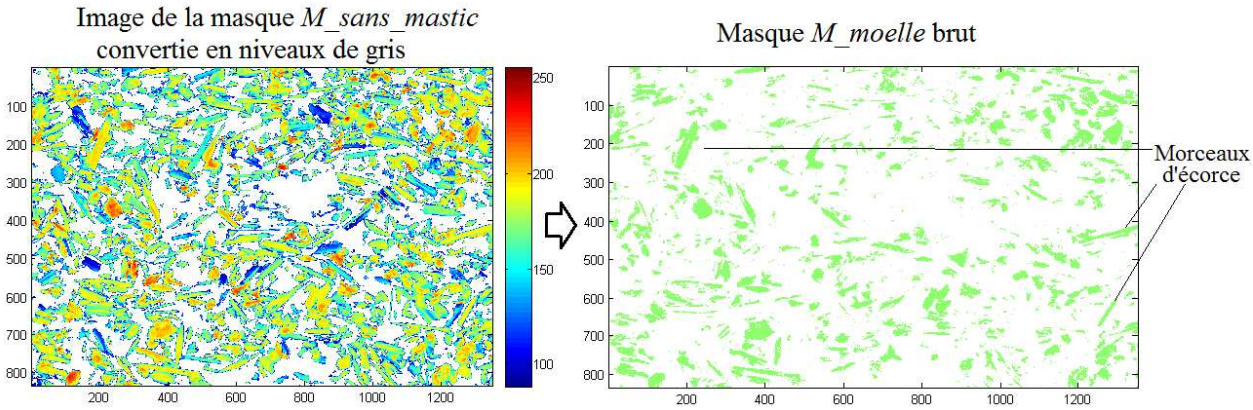

Figure 2 Procédures pour l'obtention du masque de moelle brut

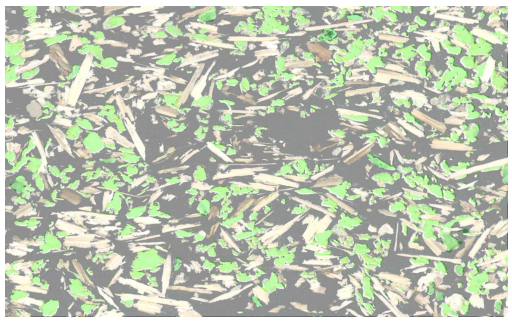

Figure 3 Masque de moelle traité et superposé sur l'image de surface étudiée

3. Une fois le masque de moelle est traité, le masque d'écorce *M_ecorce* peut être ainsi obtenu en utilisant Matlab avec la command : *M_ecorce=M_sans_mastic-M_moelle*. Ce masque obtenu devrais ensuite superposé sur l'image de surface étudiée pour être vérifié et amélioré en utilisant la logicielle GIMP 2 décrit précédemment. Les masques d'écorce et moelle sont présentés dans Figure 4)

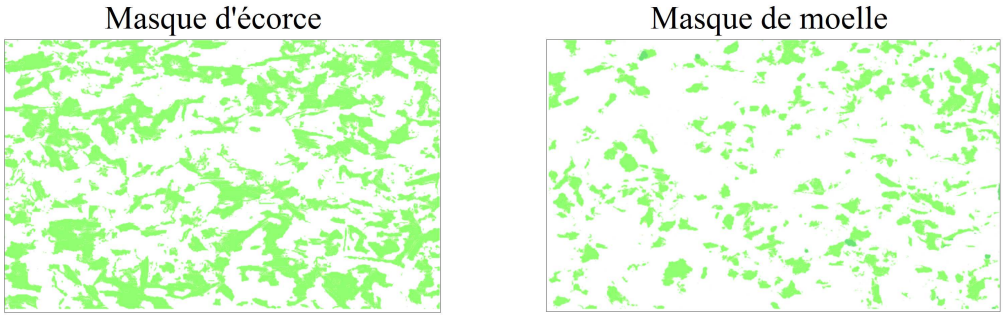

Figure 4 Masque d'écorce et moelle